UNIVERSITY OF CRETE

DEPARTMENT OF PHYSICS

PhD THESIS

Studies of 1fs scale dynamics in atoms and molecules

Paolo A. Carpeggiani

Supervisors: Prof. D. Charalambidis
Dr. P. Tzallas

UNIVERSITY OF CRETE
DEPARTMENT OF PHYSICS

PHD THESIS

DOCTOR OF PHILOSOPHY
OF
- PHYSICS -

Defended by
Carpeggiani Paolo Antonio

Studies of 1fs scale dynamics in atoms and molecules

Committee

Prof.	D. Charalambidis	-	University of Crete
Dr.	P. Tzallas	-	FORTH-IESL
Prof.	I. Kominis	-	University of Crete
Prof.	P. Rakitzis	-	University of Crete
Prof.	D. Anglos	-	University of Crete
Prof.	T. Zouros	-	University of Crete
Dr.	A. Lappas	-	FORTH-IESL

Date of the defense:
18/12/2013

"Considerate la vostra semenza:
fatti non foste a viver come bruti,
ma per seguir virtute e canoscenza"
Dante, *Inferno, XXVI* 118-120

"scire licet nobis nihil esse in morte timendum
nec miserum fieri qui non est posse, neque hilum
differre an nullo fuerit iam tempore natus,
mortalem vitam mors cum inmortalis ademit."
Lucrezio, *De rerum natura, III* 866-869

Acknowledgements

I here wish to thank all those people who helped or supported me during my hard work in FORTH and during my almost four years in Crete. A special thanks also to those who are actually reading my thesis, including these acknowledgements.

First of all, the members of my group: my supervisors, *Dr. P. Tzallas* and *Prof. D. Charalambidis*, for trusting me and for all they taught me in work and in life as well; my colleagues, *Kiki, George, Balazs, Tassos* and *Dimitris*, for helping with the boring stuff and for tolerating me in the hard times and especially in the good ones.

The technical support, in particular the guys in the machine shop and in the electronics, whom I bothered every other day with my requests for all the exotic devices or components I needed for my prototypes.

The group of *Politecnico di Milano*, that kindly hosted me for two months in 2012 and with whom I will work again from 2014.

The organizers of the *Attofel* network, for all the events, and also for the scientific part.

All my friends, for all the time and the energies we consumed together in the darkness of the heart of Crete.

Finally, my president *Silvio B.* for all the past elegant dinners and the good times to come, upon our return to the most beloved homeland.

List of publications

A compact collinear polarization gating scheme for many cycle laser pulses
G. Kolliopoulos, P. A. Carpeggiani, D. Rompotis, D. Charalambidis, and P. Tzallas
Rev. Sci. Instrum. *83*, 063102 (2012)

Disclosing one-femtosecond scale intrinsic molecular dynamics through extreme-ultraviolet pump-probe measurements
P. A. Carpeggiani, P. Tzallas, A. Palacios, D. Gray, F. Martín and D. Charalambidis
Phys. Rev. A. Accepted on Jan 23rd, 2014.

Revealing quantum path details in high-field physics
G. Kolliopoulos, B. Bergues, H. Schröder, P. A. Carpeggiani, L. Veisz, G. D. Tsakiris, D. Charalambidis and P. Tzallas
Submitted for publication.

A single-shot XUV autocorrelator
G. Kolliopoulos, P. Tzallas, B. Bergues, P. A. Carpeggiani, P. Heissler, H. Schröder, L. Veisz, D. Charalambidis, and G. D. Tsakiris
Submitted for publication.

2^{nd} order AC of an attosecond pulse train formed by long trajectory harmonics generated in gas media by a 2-color-field
P.A. Carpeggiani et al.
Article in preparation.

Contents

List of Figures

Abstract

Coherent light pulses of few to hundreds of femtoseconds (fs) duration have prolifically served the field of ultrafast phenomena. While fs pulses address mainly dynamics of nuclear motion in molecules or lattice in the gas, liquid or condensed matter phase, the advent of attosecond (asec) pulses has in recent years provided direct experimental access to ultrafast electron dynamics. However, there are processes involving nuclear motion in molecules and in particular coupled electronic and nuclear motion that occur in the few fs or even sub-fs time scale. Electronic excitations in molecules are commonly in the VUV/XUV spectral region. Until recently most of the XUV sources were lacking either sufficient pulse energy (High Order Harmonic Generation (HOHG) sources) or ultrashort pulse duration (free electron lasers (FEL) [1]), thus preventing access to XUV-pump-XUV-probe measurements in the $1fs$ or asec temporal scale. In this work, by loose focusing a multi-cycle, high power, fs Infra-Red (IR) laser ($35fs$, $\leq 160mJ/pulse$, $805nm$) into a Xenon gas jet, the non-linear interaction results in frequency up-conversion and, under proper experimental conditions for Phase Matching (PM), in the formation of Attosecond Pulse Trains (APT). The application of Interferometric Polarization Gating (IPG) [88, 89] to this scheme allows the generation of energetic, broadband, coherent extreme-ultraviolet (XUV) continuum radiation. Although the temporal properties of the XUV pulse are affected by the lack of Carrier-Envelope Phase (CEP) stabilization [86], the XUV intensity is high enough to induce XUV multi-photon absorption in atomic [75] or molecular system.
So far, experimental efforts on this time scale have been restricted to XUV-IR pump-probe schemes [34, 37, 41, 44, 73, 94], or in-situ electron-ion collision methods [59]. As the IR field induced potential may distort the molecular potential [33], the use of IR-free technique to investigate the intrinsic molecular dynamics is of central importance.The present work focuses on the development of techniques for the investigation of such dynamics utilizing solely XUV radiation and demonstrates proof of principle time resolved and XUV pump - XUV probe experiments, tracking ultrafast molecular dynamics.

In order to induce the aforementioned XUV multi-photon processes, high XUV photon flux is required. In order to increase the XUV intensity, the setup was upgraded to allow the use of 3m or 6m lenses for loose focus configuration [36], and of a Barium Borate (BBO) crystal, for 2-color driven HOHG [9, 14, 19, 25, 40, 95]. Although in our case the XUV intensity does not benefit from the 2-color generation scheme, there is the possibility in the HOHG process to control the electron re-collision trajectories by acting on the parameters of the two laser fields [10]. With this option, the use of long trajectories is convenient due to their higher energy content. The temporal characterization of the HOH obtained by the long trajectories in a 2-color driving field is an unexplored field of investigation. We succeeded in this task, recording 2^{nd} order Interferometric Volume Auto Correlation [84, 85] traces by using, for the first time, a multiply ionized atom [8, 87] as a nonlinear detector. The results show clearly the existence of a structure on the 1fs scale.

Exploiting the short duration of the above mentioned high energy pulses, all the optically allowed excited states of H_2 are coherently populated. Monitoring the pump-probe delay dependent yield of protons, nuclear and electronic $1fs$ scale dynamics are subsequently investigated and compared to the results of ab initio calculations. The revealed dynamics reflects the intrinsic molecular behavior as the XUV probe pulse, despite its still high intensity, hardly distorts the molecular potential. It was further feasible to follow the opening of the dissociative ionization channel through the $2\Sigma_g^+(2p\sigma_u)$ state, due to the stretching of the molecule. This is visible as a build-up of non-zero kinetic energies proton signal during the first fs of the delay time.

Utilizing individual harmonics, single ($5^{th} + 5^{th}, 7^{th} + 7^{th}$ harmonic) and two-color ($5^{th} + 9^{th}$ harmonic) time resolved spectroscopy has been performed in molecular Oxygen, aiming at settling existing discrepancies of previous experiments [23, 64]. Finally an attempt in observing energy resolved direct two photon atomic double ionization [43, 48] through energy resolved electron spectroscopy has identified necessary actions and improvements for a successful implementation of such an experiment.

1 Theory

1.1 High Order Harmonic Generation - HOHG

The achievement of shorter laser pulse duration is inherently limited not only by the carrier frequency of the pulse, but also by its spectral bandwidth. Indeed in wave mechanics, the uncertainty principle states that $\Delta E \Delta t \geq h/4\pi$, or, equivalent, $\Delta\omega\Delta t \geq 1/2$. Thus, shorter laser pulses require shorter carrier frequencies and larger spectral bandwidth, and both can be obtained through the frequency up-conversion of a conventional IR, fs laser pulse.

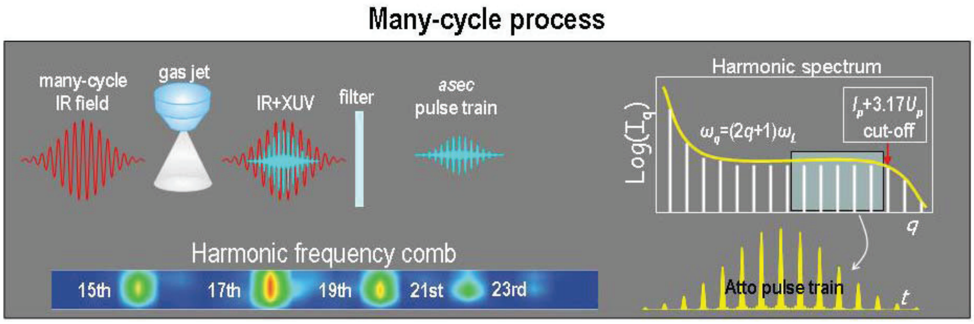

Figure 1: Schematic of APT generation by a many cycle laser process. By focusing a many-cycle linearly polarized driving laser field in a gas phase medium, XUV radiation is emitted in the direction of propagation of the driving laser field. The spectrum of the XUV radiation contains well confined odd harmonic frequencies. By using the proper metal filter a part of the spectrum can be selected. The temporal profile of the selected spectrum may then have the shape of APT. The contour iso-intensity colour plot shows a typical harmonic spectrum which has been recorded by using a 50 fs long driving pulse. In the harmonic spectrum are visible the main features of the process: the amplitude throughout the first harmonic orders rapid decreases; when $q\hbar\omega \geq I_p$, the conversion efficiency becomes constant, forming the plateau region of the spectrum; the harmonic amplitude drops fast in the cut-off region. [89] *[P. Tzallas et al. Progress in Ultrafast Intense Laser Science (Springer Series in chemical physics) vol. VII, p. 163 (2011)]*

A reliable way to obtain pulses with XUV spectrum and sub-fs duration is the HOHG from gases. In fig. 1 the principle of attosecond pulse generation in gases is shown schematically. Briefly, by focusing an intense, linearly polarized, many-cycle, fs, IR laser beam into a gas phase medium, the medium is non-linearly driven to emit short-wavelength radiation in the direction of propagation of the laser field. The emitted spectrum consists of odd harmonics of the driving frequency and presents a characteristic behavior:

1. the amplitude throughout the first harmonic orders rapid decreases

2. when the harmonic photon energy becomes equal or larger than the ionization energy of the medium, its conversion efficiency becomes and remains constant up to the highest-order harmonics, forming the *plateau* region of the spectrum.

3. the harmonic amplitude drops fast in the *cutoff* region.

This phenomenon was first observed in 1988, by *Ferray et al.* [28]. Since then, it has been extensively studied both theoretically and experimentally. In gases, the physics of the single-atom response has been explained with "the three step model" [18, 47] in a semi-classical picture, as represented in fig. 2: in a strong-field low-frequency regime, the electron can tunnel out from the core through the Coulomb barrier lowered by the electric field of the laser. The electron is considered to have zero kinetic energy at the moment of its release into the continuum, then it undergoes oscillations in the field, during which the influence of the Coulomb force from the nucleus is negligible. Some of the trajectories come back to the vicinity of the nucleus and may lead to a radiative recombination back to the ground state, thus producing a photon of energy I_p plus the kinetic energy E_C acquired during the motion [70]. The motion of the electron in the continuum can be treated classically, considering $x(t_i) = 0$ and $v(t_i) = 0$, with driving field $E_0 \cos(\omega t)$:

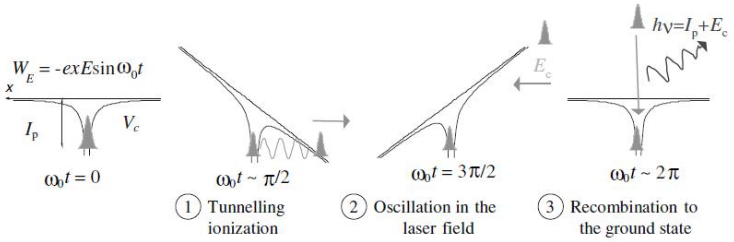

Figure 2: Semi-classical model for harmonic generation: the electron is subjected to the Coulomb potential V_c and to the interaction W_E with the strong laser field *P. Saliéres, M. Lewenstein* [70].

$$x(t) = \frac{-eE_0}{m\omega^2}\left[\cos(\omega t) - (\omega t_i) + (\omega t - \omega t_i)\sin(\omega t_i)\right] \tag{1}$$

the recombination takes place when:

$$x(t_r) = x(t_i) = 0 \Rightarrow \cos[\omega(t_i + \tau)] - \cos(\omega t_i) - \omega t_i = 0 \tag{2}$$

being τ the traveling time, t_i the ionization time and t_r the recombination time. From this condition the relation between t_i and τ reads:

$$t_i = \frac{1}{\omega} \arctan \frac{\cos(\omega\tau) - 1}{\sin(\omega\tau) - \omega\tau} \tag{3}$$

Considering the initial condition $v(t_i) = 0$, $v(t)$ reads:

$$v(t) = \frac{eE_0}{m\omega} \left[\sin(\omega t) - \sin(\omega t_i)\right] \tag{4}$$

and thus the kinetic energy at the recombination time reads:

$$E_k(t_r) = \frac{e^2 E_0^2}{2m\omega^2} \left[\sin(\omega t_r) - \sin(\omega t_i)\right]^2 \tag{5}$$

where $e^2 E_0^2 / 4m\omega^2 = U_p$ is the ponderomotive energy. By searching the stationary points in eq. 5, we find that the maximum kinetic energy that the electron can gain is $E_C^{max} = 3.17 U_p$.
This model has the advantage of simplicity and allows us to understand some of the main features of the process:

- the sudden loss of efficiency of conversion for the HOH in the cutoff is explained in terms of the mean kinetic energy gained by the electron due to the ponderomotive potential, plus the ionization potential of the parent atom; the cutoff value is determined as $E_{cutoff} = I_p + 3.17 U_p$.
- by solving eq. 3, it is found that the main contributions to the HOHG are due to trajectories with traveling times τ_S and τ_L, called respectively short and long trajectories.
- only odd high harmonics $(2n + 1)\omega = q\omega$ are produced.

Considering that the system is spherically symmetric, there are several ways to explain the last point. From a quantum mechanical point of view, the conservation of the angular momentum requires that the total number of photons involved in the process should be even. This is explained by the fact that the atom, after the multi-photon absorption and the emission of a single photon, returns to its initial, ground state and, in the whole process, each photon contributes only by ±1 to the angular momentum. Thus, one photon emission at high frequencies requires the absorption of an odd number of photons at the fundamental frequency. Alternatively, in the classical picture, since the XUV emission takes place every $T/2$ of the driving field, this leads to a spacing of 2ω in the frequency domain. Also, it can be explained by considering the electric fields of the driving laser and of the generated harmonics. In the driving field $\vec{E} = E_0 \cos(\omega t)$, neglecting the variation of E_0 over an optical cycle, as a multi-cycle laser is considered:

$$E_0 \cos(\omega t) = -E_0 \cos(\omega t + \pi) \tag{6}$$

As the system is isotropic, this is also required for the field of the harmonics:

$$E_0^q \cos(q\omega t) = -E_0^q \cos(q\omega t + \pi) \tag{7}$$

but this condition is satisfied only for odd $q = 2n + 1$. Even harmonics can appear only in non-symmetric systems, like anisotropic crystals or surfaces, but not in gases interacting with one color radiation.
The successive quantum mechanical model by Lewenstein [49], which is valid for the Single Active Electron (SAE), when a single atom interacts with a high intensity laser field (high compared to the electric field of the atomic potential) of low frequency (low compared to the time that an electron needs to tunnel out from an atomic potential distorted by the driving field), is based upon the quantum path analysis and it is capable to provide more accurate solutions about the electron quantum paths, spectral phase and amplitude of the harmonics. Starting from the expression for the single-atom dipole moment:

$$\begin{aligned} x(t_r) = i \int_0^{t_r} \mathrm{d}t_i \int \mathrm{d}^3p \times \left[\mathrm{d}^* \left(\vec{p} - \vec{A}(t_r)\right)\right] \times \\ \times \left[\vec{E}(t_i) \cdot \mathrm{d}\left(\vec{p} - \vec{A}(t_i)\right)\right] \times \mathrm{e}^{-iS(p,t_r,t_i)} + c.c \end{aligned} \tag{8}$$

where the quantity S denotes the quasi-classical action that the electron experiences during its excursion in the continuum and reads as:

$$S(\vec{p}, t_r, t_i) = \int_{t_i}^{t_r} \mathrm{d}t \left(\left([\vec{p} - \vec{A}(t)]^2/2\right) + I_p\right) \tag{9}$$

In Feynman's spirit, this is an integral over all possible electron trajectories that are characterized by t_i, t_r and $\vec{p}$. $\vec{p} = \vec{u} + \vec{A}(t)$ is the canonical momentum, $\vec{A}(t)$ the vector potential of the driving electric field, $\vec{u}$ the electron velocity in the continuum and d the dipole matrix element for bound-free transitions. As shown in [49, 71], eq. 8 can be solved using the Saddle-Point Approximation (SPA). In this approximation, the integral over all the possible electron trajectories becomes a sum over the most significant one, with values of t_i, t_r and $\vec{p_s}$ which are determined by the principle of stationary action. This results in a single atome dipole moment which reads as:

$$\begin{aligned} x(t_r) = i \int_{-\infty}^{t_r} \mathrm{d}t_i \left(\frac{\pi}{\mu - i(t_r - t_i)/2} \right)^{3/2} \left[\mathrm{d}^* \left(\vec{p_s} - \vec{A}(t_r) \right) \right] \times \\ \times \left[\vec{E}(t_i) \cdot \mathrm{d} \left(\vec{p_s} - \vec{A}(t_i) \right) \right] \times \mathrm{e}^{-iS(\vec{p_s}, t_r, t_i)} + c.c \end{aligned} \tag{10}$$

where μ is a positive regularization constant (associated with the effect of quantum diffusion [3]) and

$$\vec{p_s} = \frac{1}{t_r - t_i} \int_{t_i}^{t_r} \vec{A}(t) \mathrm{d}t \tag{11}$$

is the stationary value of the momentum, which is obtained by setting $\nabla_p S(\vec{p}, t_r, t_i)|_{p_s} = 0$.
The Fourier transform of the single-atom dipole moment can be calculated as:

$$x(\omega) = \int_{-\infty}^{+\infty} x(t_r) \mathrm{e}^{i\omega t_r} \mathrm{d}t_r \tag{12}$$

The harmonic emission rate is given by [56]:

$$W(\omega) = \omega^3 |x(\omega)|^2 \tag{13}$$

The generalized phase term of a specific frequency ω is:

$$\Theta(\vec{p_s}, t_r, t_i) = \omega t_r - S(\vec{p_s}, t_r, t_i) \tag{14}$$

To solve eq. 13, and to obtain the most significant values of t_i and t_r contributing to the spectrum, the stationary phase approximation $\partial\Theta/\partial t_r|_{t_{rs}} = \partial\Theta/\partial t|_{t_{is}} = 0$ has to be applied. For a given value of the photon energy $\hbar\omega$, a series of saddle point solutions $S(\vec{p_s}, t_r, t_i)$ is obtained. By using this approximation to the generalized phase term of eq. 14, the Fourier transform of the dipole moment, $x(\omega)$, can be transformed to [50]

$$\begin{aligned} x(\omega) &= \sum_S |x_S|(\omega)| \mathrm{e}^{I\Phi_S(\omega)} = \\ &= \sum_S \frac{i2\pi}{\sqrt{\det(\ddot{S})}} \left[\frac{\pi}{\epsilon - i(t_{rs} - t_{is})/2} \right]^{3/2} \times \left[\mathrm{d}^* \left(\vec{p_s} - \vec{A}(t_i) \right) \right] \times \\ &\times \left[\vec{E}(t_{rs}) \cdot \mathrm{d} \left(\vec{p_s} - \vec{A}(t_i) \right) \right] \times \exp\left[-iS(\vec{p_s}, t_{rs}, t_{is}) + i\omega t_{rs} \right] \end{aligned} \tag{15}$$

Eq. 15 is a coherent superposition of the contributions from the complex saddle-point solutions of $(\vec{p_s}, t_{rs}, t_{is})$. In eq. 15, $\Phi_S(\omega)$ is the phase of the complex function of the dipole moment $x_S(\omega)$, and $\det(\ddot{S}) = \det(\ddot{\Theta})$ is the determinant of the 2×2 matrix of the second derivative of $\Theta(\vec{p_s}, t_{rs}, t_{is})$ with respect to t_r and t_i, evaluated in correspondence with the saddle point solutions $(\vec{p_s}, t_{rs}, t_{is})$. The physical interpretation of the saddle-point solutions is that photon of energy $\hbar\omega$ are emitted mostly by electrons that are set free at time t_{is}, have acquired momentum $\vec{p_s}$ in the electric field, and recombine with the nucleus at a time t_{rs}. It is thus found that two interfering electron trajectories, with different flight times $\tau_q^L(I_L)$ and $\tau_q^S(I_L)$ contribute to the emission of each harmonic q, at a given driving laser intensity I_L. The phase of each frequency component ω is obtained from $\mathrm{Re}\left[\Theta(\vec{p_s}, t_{rs}, t_{is})\right]$.

So far, the two models reported above, explain the microscopic harmonic emission caused by the non-linear response of the atom subjected to the intense laser field. The macroscopic harmonic field measured in the experiment is the coherent superposition of the fields emitted by all the atoms of the generating medium. For a given harmonic order q, constructive addition occurs along the propagation direction over the so called coherence length $L_{COH} = \pi/\Delta k$. Here $\Delta k = qk_1 - k_q$ is the wave-vector mismatch along the propagation direction between the generated field and the laser-induced polarization at frequency $q\omega$. In order to maximize the coherence length, the wave-vector mismatch must be minimized. In a non-guiding focus geometry, this can be done through the interplay between the four sources of wave vector mismatch [6, 16, 68, 69]:

$$\Delta k = \Delta k_g + \Delta k_n + \Delta k_p + \Delta k_d \tag{16}$$

The contribution $\Delta k_g < 0$ originates from the Gaussian beam phase gradient along the propagation direction (z). $\Delta k_n > 0$ and $\Delta k_p < 0$ describe the neutral and free-electron dispersion, which have opposite sign and are proportional to the gas pressure. Δk_d, which is negative if the laser focus is before the jet and *vice versa*, is the gradient of the so called dipole phase, which is proportional to the intensity gradient and is small for the short trajectories and large for the long ones [69]. If only short trajectories are considered (or, experimentally, selected by focusing the laser before the medium), the Δk_d contribution can be neglected. For a given medium, harmonic order and focal length, the only variable parameter is the free-electron contribution, which can be adjusted by changing the laser intensity. Eq. 16 requires the intensity to be low enough so that the contribution due to the neutral dispersion dominates over the free-electron dispersion. This defines a maximum ionization degree above which phase-matched generation is not possible (saturation of the medium). When the coherence length is maximized, the harmonic emission is limited by re-absorption in the generation gas. An absorption length is defined so that:

$$pL_{ABS} = \frac{kT}{\sigma_{ion}} \tag{17}$$

where p is the gas pressure, k is the Boltzmann constant, T the temperature and σ_{ion} the ionization cross section. According to [17], the harmonic yield is then maximized for $L_{med}^{opt} \geq L_{ABS}$. For high-energy laser systems, an increase in the absorption limited HOH intensity can be achieved by increasing the focal length for a certain initial beam diameter [36]. L_{med}^{opt} thus depends upon the density of the medium, so that by raising the pressure p it becomes shorter. In fact, this sets an upper limit to the number of atoms which interact with the fundamental frequency, so that typical conversion efficiency factors in HOHG from gases do not exceed $10^{-5} - 10^{-4}$. Even though this value may look very small, with the use of the loose focus configuration, combined with experimentally improved phase matching conditions and the availability of IR lasers with higher and higher energy content per pulse, allowed the generation of APT and Isolated Attosecond Pulse (IAP) with intensity up to $10^{14} W/cm^2$ [58, 74, 79, 83, 91].

1.2 High order harmonic generation by $\omega - 2\omega$ field

Although the maximization of the conversion efficiency can be achieved by optimizing the phase matching conditions in the harmonic generation medium, an alternative approach, based on the harmonic generation by a 2-color field, can be used for the enchantment of the harmonic energy. By controlling the relative phase between the two colors in a 2-color driving field we are able to control the electron quantum paths in the continuum and thus to control the re-collision cross section.

Several theoretical and experimental works have demonstrated the possibility to enhance the HOHG in gases by the interaction of a two color field both with parallel [14] and perpendicular linear polarizations [40]. Such an enhancement may concern the improvement of the efficiency of conversion for the harmonics in the plateau, the extension of the cut-off or the shortening of the XUV pulse [9, 95]. Usually the two colors are provided through parametric amplification or, more often, by doubling the laser frequency through Second Harmonic Generation (SHG) [19].From now on we refer to the case where the laser fields are carried by $\omega - 2\omega$ frequencies, as in fig. 3. The explanation for the improved efficiency in the $\omega - 2\omega$ case is straightforward. With the second harmonic, it takes half the number of photons $(q/2)$ to ionize

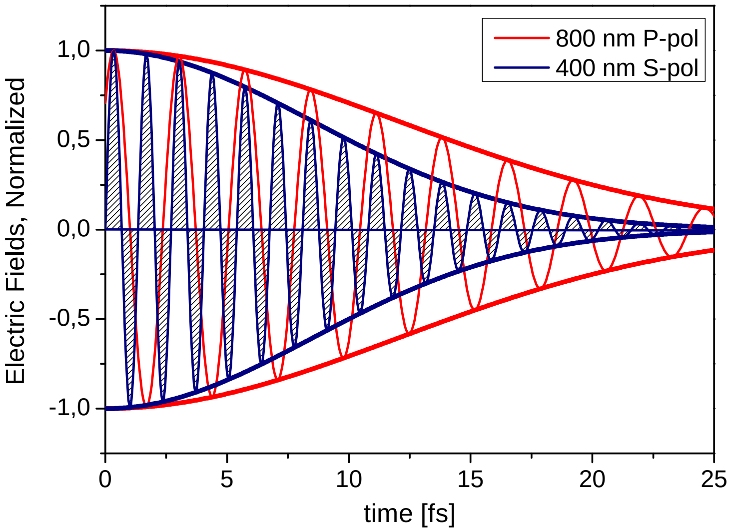

Figure 3: $\omega - 2\omega$ field for an IR pulse with duration $\tau_L = 20fs$ FWHM and its second harmonic. The fields are represented with equal amplitude in the center of the pulse to show better the different shape of the two fields.

an atom as compared to the case where only the fundamental is used. Therefore, within the lowest order perturbation theory, the probability varies like $I_0^{q/2}$ instead of I_0^q, I_0 being the intensity of the driving field and q the number of photons, at the fundamental frequency, required to ionize the atom. The order of the process is thus almost twice as small, and therefore more efficient at comparable intensity [19]. In this case another interesting feature is the appearance of the even harmonics and the possibility to adjust the relative intensities of all the harmonics by tuning the relative delay between the ω and 2ω fields. The appearance of even harmonics can be explained in terms of the selection rules for photon absorption and emission by a spherically symmetric atom. For instance, in the case of high harmonic emission, for the conservation of angular momentum it is required that an odd number of photons from the driving field be absorbed for one photon at higher frequency to be emitted. Clearly, in the one-color field case, this implies that only odd harmonics can be emitted. In the 2-color field case both odd and even harmonics are possible. As the obtained harmonic spacing is ω instead of 2ω, under the condition of phase locking between the harmonics, we can expect the temporal spacing from the asec pulses to be $\Delta t = 2\pi/\omega = T_{IR}$, twice as large as that of the one-color generation, where the temporal spacing is $\Delta t = 2\pi/2\omega = T_{IR}/2$.

Note that it has not been necessary to develop a dedicated theoretical model

in order to predict the properties of High Order Harmonics (HOH) generated through this different approach. The Lewenstein model does not have particular restrictive assumptions, neither on the field polarization nor in the use of different frequencies. It can be, and has been, used to perform numerical integration.
We can highlight the differences between the HOHG in the one-color case as compared with the 2-color case by integrating the equation of motion for the ejected electron, $F = m\ddot{x} = eE$, in the 2-color case. In the case of 2-color perpendicular field generation, the total driving field reads:

$$\vec{E} = E_{0x}\cos(\omega t)\vec{e_x} + E_{0y}\cos(2\omega t + \phi)\vec{e_y} \tag{18}$$

Integrating the differential equation for the x and y:

$$\ddot{x} = \frac{eE_{0x}}{m}\cos(\omega t) \tag{19}$$

$$\ddot{y} = \frac{eE_{0y}}{m}\cos(2\omega t + \phi) \tag{20}$$

we obtain:

$$x(t) = \frac{eE_{0x}}{m\omega^2}\left[\cos(\omega t_i) - \cos(\omega t) + (\omega t_i - \omega t)\sin(\omega t_i)\right] \tag{21}$$

$$\begin{aligned} y(t) = {} & \frac{eE_{0y}}{4m\omega^2}\left[\cos(2\omega t_i + \phi) - \cos(2\omega t + \phi)\right] + \\ & + \frac{eE_{0y}}{2m\omega^2}\left[(\omega t_i - \omega t)\sin(\omega t_i + \phi)\right] \end{aligned} \tag{22}$$

In this case the trajectory of the ejected electron is in a bi-dimensional space, and the recombination with the parent ion ($R < R_a$) can take place only if there is a time t_r for which the distance $R = \sqrt{x^2 + y^2}$ is smaller than the atomic radius R_a. This distance, which is associated with the re-collision cross-section, defines the spectral phase distribution of the emitted XUV radiation and stongly depends on the relative phases (see fig. 4) and amplitudes of the two fields.

Concerning the experimental conditions, it must also be noted that in all the cited work the laser systems in use provide high repetition rate and low laser energy, usually in the $100\mu J$ [14] or $1mJ$ [25, 40] range. Our experimental setup is optimized to operate in loose focusing configuration, at $10Hz$ repetition rate and a laser energy on the gas jet around $30mJ$. Due to the different experimental conditions (loose focusing configuration and the phase matching conditions), the enchantment of the harmonic yield is a

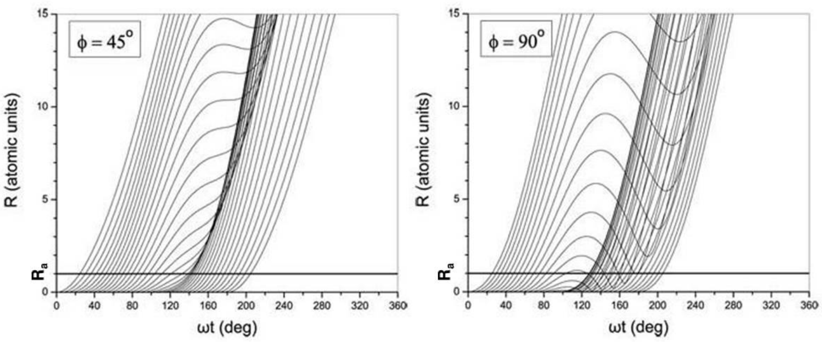

Figure 4: Electron trajectories in 2-color field. The recombination of the electron with its parent ion ($R < R_a$) takes place only for specific conditions on the relative phase and amplitude of the two fields. Here is compared the effect of the phase: for $\phi = \pi/4$ (left) there is no recombination; for $\phi = \pi/2$ it can take place for some trajectories.

subject of investigation. Additionally, the temporal characterization of the EUV radiation generated by a 2-color field has never been done before and is also subject of investigation. Also, the recently published work [10], which concerns the control of the short and long trajectory harmonics generated by a 2-color field, constitutes the the starting point for the experiment we present in sec.3.2 and 3.4.

1.3 Isolated attosecond pulse supported by an XUV coherent continuum

HOH generated by multi-cycle IR driving field lead to APT. Although these pulses have many applications on the dynamic in the asec time scale, the use of intense IAPs [15, 26, 35, 52, 72, 74, 77] is much more beneficial for ultrafast dynamic studies in all states of matter.

The above described technique allows the production of APT, having each of them considerably short durations. However, it is highly desirable for pump-probe experiments to use single IAP. For the emission of isolated asec pulses, we need to generate a temporal gate, with a width τ_g close to half the driving laser period, near the peak of the envelope of the laser pulse, within which the XUV emission will take place. By controlling the width τ_g of the gate with asec precision, we can manipulate the dynamics of the quasi-free electron wave packets is such a way, that it revisits and recombines with the atomic core only once. In this case, the XUV emission is confined to a single attosecond burst as shown schematically in fig. 5. The idea of the gate formation is based on the dependence of the harmonic generation on the ellipticity of the driving laser field [76]. The harmonic intensity I_q

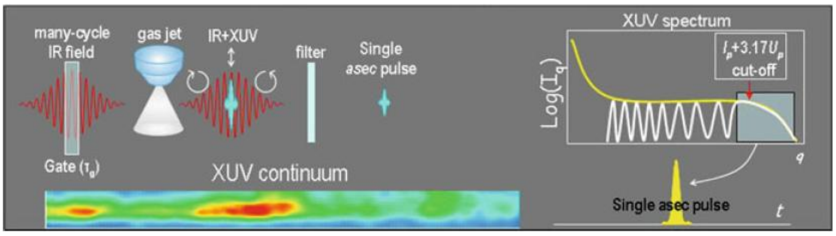

Figure 5: Schematic representation of the generation of an isolated asec pulse applying the Polarization Gating (PG) concept using a many-cycle ElMo driving field. By placing a few cycles wide gate at the peak of the many-cycle driving field envelope, the XUV emission is confined to few XUV bursts. The spectrum of the XUV radiation is quasicontinuous with a continuum part in the cutoff region. By using the proper filter the continuum part of the spectrum can be selected. The temporal shape of the selected spectrum can be that of an isolated asec pulse. The contour isointensity color plot shows a typical quasicontinuum spectrum, which has been recorded by using an Interferometric Polarization Gating (IPG) device. [89] *[P. Tzallas et al. Progress in Ultrafast Intense Laser Science (Springer Series in chemical physics) vol. VII, p. 163 (2011)]*

rapidly drops with the ellipticity of the driving laser field [2]. According to the lowest order perturbation theory [11], the dependence of the harmonic intensity on the harmonic order q and ellipticity ϵ is given by:

$$I_q = \left(\frac{1-\epsilon^2}{1+\epsilon^2}\right)^{q-1} \tag{23}$$

For linear polarization, where $\epsilon = 0$, I_q is maximum (I_q^{max}), while for circular polarization $I_q(\epsilon = 1) \approx 0$. There is a value of ellipticity, known as the ellipticity threshold ϵ_{th}, above which $I_q < I_q^{max}/2$. This threshold can be used to define the beginning and the end of the gate, thus creating an XUV emission switch. Within the interval during which the gate is open (τ_g) the XUV emission can take place. During this time interval, the ellipticity ϵ varies in the interval $0 \leq \epsilon \leq \epsilon_{th}$. When, in the time domain, XUV emission is restricted to occur within a narrow temporal gate τ_g (that is, from half a cycle T_L of the driving laser field up to few cycles), in the frequency domain a XUV coherent continuum (when $\tau_g \leq T_L/2$) or quasi continuum (when $\tau_g \approx T_L$) spectrum is obtained. One solution to the problem of achieving a narrow gate τ_g starting from a many-cycle pulse with duration τ_L has been proposed in [88] with the IPG approach. The operating scheme is reported in fig. 6. The parameters which determine the width of the gate are the delay between the pulse pairs and the intensity ratio of the perpendicular components E_1 and E_2 of the electric field. The analytical calculations are

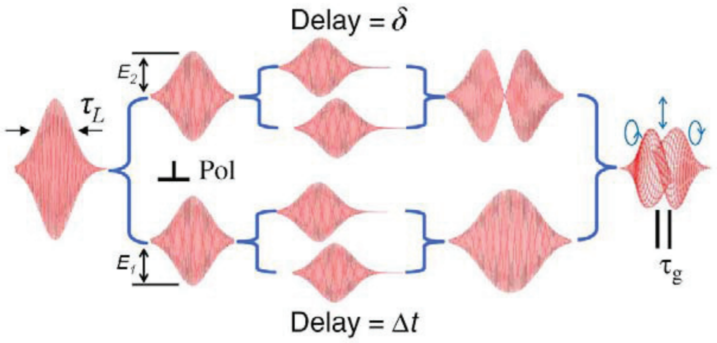

Figure 6: Schematic representation of the IPG approach. The incoming pulse, with duration τ_L, is split in two with perpendicular polarizations and different amplitudes E_d and E_c. Then, each of these pulses is split again into two. Two of the appropriately delayed (δt) pulses interfere constructively, while the other two with delay δ form a destructive interference minimum. The polarization planes of the superposition are mutually perpendicular. The two waveforms are superimposed forming an ElMo pulse with linear polarization in its central part. τ_g is called gate width and corresponds to the temporal window where the polarization is almost linear. *[P. Tzallas et al. Progress in Ultrafast Intense Laser Science (Springer Series in chemical physics) vol. VII, p. 163 (2011).]*

also reported in the cited work to obtain the expression for the gate time as:

$$\tau_g = \frac{\tau_L^2 \log_2(A)}{2\delta} \tag{24}$$

where A, and its parameters B and λ,are defined as:

$$A = \frac{-2\lambda\sqrt{1-B^2} + B\left(\lambda^2-1\right)}{B-2\lambda+B\lambda^2} \tag{25}$$

$$B = \sin\left(2\tan^{-1}\left(\epsilon_{th}\right)\right) \tag{26}$$

$$\lambda = \frac{E_2}{E_1} \tag{27}$$

The emitted XUV spectrum has also been calculated by solving the three step model using the saddle point method. The scheme shown in fig. 6 has been achieved first with a Double Michelson Interferometer (DMI) arrangement, then with the Double Mach-Zehnder Interferometer (DMZ) which, at the cost of reducing the degrees of freedom in the choice of the amplitude of the electric fields (each constructive and destructive pulse is the product of the recombination of a pair of pulses: DMI allows to choose the amplitude for the four of them, the DMZ to choose the ratio between pairs) has a transmission efficiency in energy of 50% instead of 25%, as well as the intensity content in the gating interval is twice as for the DMI. The DMZ setup has been used in

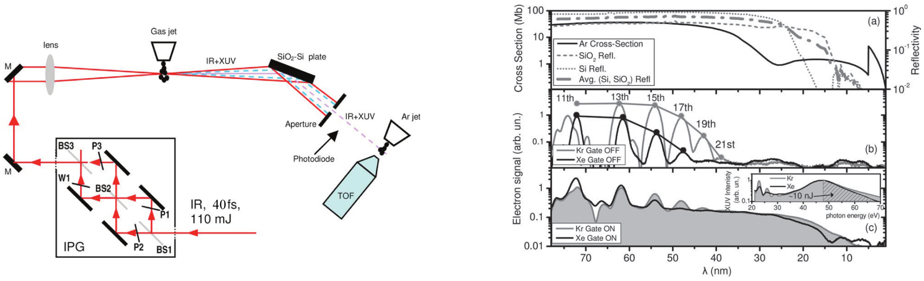

(a) (b)

Figure 7: IPG setup and obtained spectra.*[E. Skantzakis et al. Opt. Lett. 2009].* (a): Experimental setup. P1, P2, W, and BS1, BS2, BS3 represent the delay plates, $\lambda/2$ wave plates, and beam splitters, respectively. B1, B2 are 50/50 beam splitters, while B3 has 20% reflectivity and 80% transmission.(b): (Top) Black solid curve, single-photon ionization cross section of Ar. Gray dotteddashed, gray dotted, and gray dashed curves, reflectivity of the oxidized Si, Si, and SiO_2 plate, respectively. (Middle) Black and gray solid curves, harmonic spectrum generated in Xe and Kr, respectively, by a $115fs$ IR pulse. (Bottom) Black solid curve and gray filled area, quasi-continuum spectrum generated in Xe and Kr gases when a temporal gate of $\tau_g \approx 4.5fs$ duration is on.

the past in our laboratory to produce IAPs supported by a XUV continuum spectrum [74]; these pulses have been characterized by Auto Correlation (AC) and used for pump-probe experiments for the study of Auto Ionizing States (AIS) in Xenon [75]. The experimental setup is shown in fig. 7(a), while a typical continuum spectrum is shown in fig. 7(b).

1.4 2^{nd} order Intensity or Interferometric Volume AC

Once APT or IAP are generated, a full characterization is necessary. The temporal characterization is the most challenging.

In order to characterize the temporal properties of APT or IAP, we use the 2^{nd} order Intensity (or Interferometric) Volume Auto Correlation (2-IVAC) technique, which is accurately described in [24, 38, 54, 83, 84]. A dispersionless XUV autocorrelator is required: a spherical, golden coated, split mirror mounted on a piezoelectric delay stage works both as wavefront divider and delay selector. Like in the usual 2^{nd} order AC used in IR pulse duration metrology,the presence of a non-linear medium is required. In the case of XUV, the single or multiple ionizations of some noble gases can be used. There are two points that distinguish this technique from the conventional Michelson interferometer based on a nonlinear crystal or a nonlinear photodiode:

- the signal produced emanates from the interaction of the XUV pulse with the non-linear medium (He atoms) within a volume defined by the focusing properties of the spherical mirror and not from a plane as in the case of a nonlinear crystal.
- unlike the amplitude splitting arrangements, the split mirror technique is a wavefront splitting device and as such, a delay variation results not in a change of the energy reaching the detector, but simply in a spatial redistribution of the energy in the focal volume according to the diffraction principle

Because of these differences, the signal to background ratio is lower than in the conventional methods. It has been shown that the theoretical S/B ratio for 2-IVAC (interferometric AC) is in the range $2.8 \leq S/B \leq 3.4$, (for conventional AC methods $S/B = 8$) depending upon the considered volume of interaction (infinite or small volume). In the corresponding Intensity 2-IVAC, which is obtained from the interferometric by cycle-averaging the fast oscillations, the values are $2.1 \leq S/B \leq 2.4$, to be compared with $S/B = 3$ in the conventional cases. In experimental traces S/B values are usually lower, mainly because of the difficulty in overlapping perfectly the two replicas of the pulse.
The relation which connects the duration of the Intensity 2-IVAC trace to the duration of the pulse is $\tau_{AC} = 1.41\tau_{pulse}$, like in conventional AC traces.

In order for the detector to be non-linear, it is important to avoid any contributions from single photon ionization. Also, since the bandwidth of the asec pulses is much broader (several eV) compared to that of any of the IR pulses, its is not straightforward that the conditions of flatness and instantaneous response can be fulfilled over the whole bandwidth. Finally, only direct processes are suitable for the temporal characterization of the XUV pulse. If also a sequential process is involved, the measured AC trace will be a convolution of a squared 1^{st} order AC trace (resulting from the photons involved in the sequential process) and a 2^{nd} order AC trace resulting from the photons involved in the direct 2^{nd} order process).

1.5 Effects of Carrier Envelope Phase - CEP

The CEP - oscillations are a limiting factor in the achievement of a single IAP.

The CEP is the relative phase between the envelope of the laser pulse and

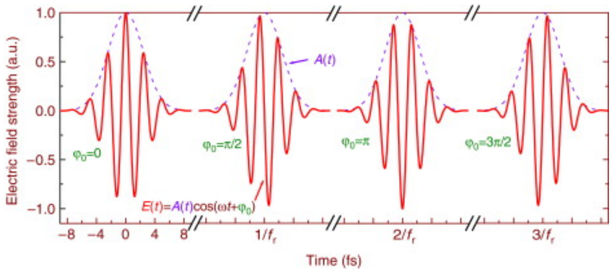

Figure 8: Laser pulses with different CEP values.

the carrier frequency. Fig. 8 shows few cycle laser pulses with different CEP values. In general it fluctuates between consecutive laser shots, but for many-cycle lasers this does not play an important role, as the envelope can be considered to be varying slowly as compared to the period of the laser wavelength. Also when such lasers are used for HOHG, CEP does not produce sensible variations in the XUV pulse. The situation changes for few-cycle IR lasers and polarization gating approaches. Many studies [7,77,88] proved that the CEP variation in few-cycle laser pulses affects the generation of XUV pulses, switching from a pure continuum spectrum to a quasi-continuum with very broadened harmonics.This problem forced the researchers to develop

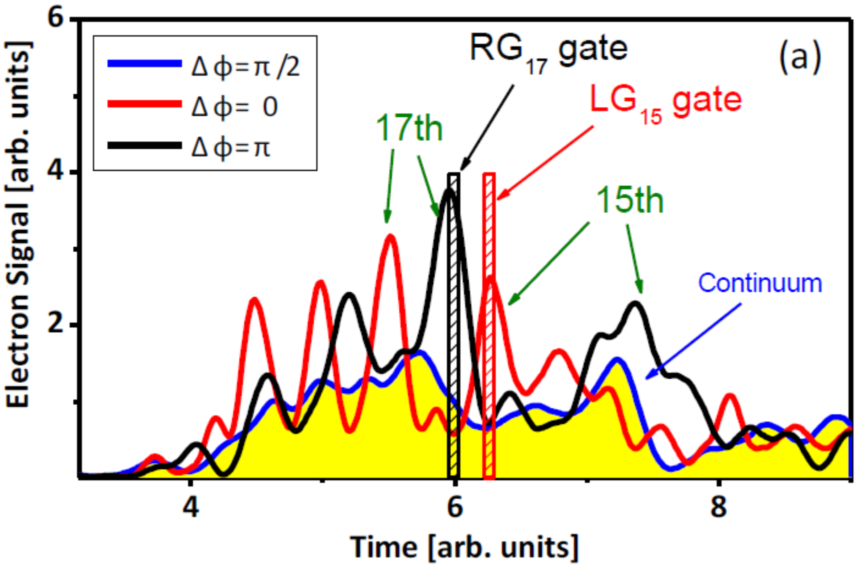

Figure 9: Single shot photoelectron spectra equivalent to the generated XUV spectra, which are obtained for different CEP value. Note that pure continuum is achieved around $\Delta\phi = \pi/2$, like the second pulse in figure 8. *[P. Tzallas et al. PRA 2010.]*

few-cycle IR laser system with CEP stabilization [7, 81].
In fact, all the approaches leading to isolated asec pulses supported by XUV continuum radiation are affected by CEP variations, and this includes also many-cycle laser systems when used in combination with an IPG device [88].
In previous studies from our group it has been demonstrated how the use of the IPG device makes the polarization gated part of a laser pulse from a many-cycle pulse equivalent to a few-cycle one [86]. Also, when using the IPG technique, the shot to shot variations in the XUV spectra allow the shot to shot measurement of the CEP value for a multi-cycle laser.
In the frequency domain, displacements $\Delta\phi = \pi/2$ in the CEP value change the structure of the spectrum from continuum to quasi-continuum with broadened and shifted harmonics, as shown in fig. 9. In the time domain, a single IAP turns into a double peak, with $1.3fs = 0.5T(\lambda = 800nm)$ separation. This aspect has to be considered when performing experiments with the IPG and when comparing the obtained data trace with the theoretical calculations.

1.6 Molecular dynamics

Since a large part of the present work concerns studies of ultrafast molecular processes, it is considered essential to provide the fundamentals of molecular physics and of the pump-probe approach (sec. 1.7).

The knowledge of molecular energy levels can be obtained from the Schrödinger equation:

$$H\Psi(\vec{x},\vec{R}) = E\Psi(\vec{x},\vec{R}) \tag{28}$$

$$H = K_N + K_e + V_{eN} + V_{NN} + V_{ee} = K_N + H_e \tag{29}$$

where K_N denotes the kinetic energy of the nuclei, K_e the kinetic energy of the electrons, V_{eN} the Coulomb interaction between electrons and nuclei, V_{NN} among nuclei, V_{ee} among electrons. If we compare the Hamiltonian in eq. 29 for molecules with the one in eq. 31 for atoms:

$$H\Psi(\vec{x},\vec{R}) = E\Psi(\vec{x},\vec{R}) \tag{30}$$

$$H = K_e + V_{eN} + V_{ee} \tag{31}$$

we notice that in molecules the additional terms K_N and V_{NN} appear. This could complicate much the solution of the Scrödinger equation in eq. 28; fortunately, the well known Born-Oppenheimer approximation states that, as nuclei are much heavier and slower than electrons, they can be considered to be almost stationary with respect to the electron motion, while the average electronic distribution (rather than the instant one) can be considered when solving the motion of the nuclei. For this reason the wavefunction can be split into independent parts of nuclei and the electrons:

$$\Psi(\vec{x},\vec{R}) = \Psi_e(\vec{x},\vec{R}')\Psi_N(\vec{R}) \tag{32}$$

$$H_e\Psi_e(\vec{x},\vec{R}') = E_e(\vec{R}')\Psi_e(\vec{x},\vec{R}') \tag{33}$$

where the function Ψ_e has to be evaluated at fixed positions for the nuclei ($\vec{R}'$). In order to evaluate the energy levels, the motions of electrons and nuclei can be considered separately. For nuclei we obtain

$$K_N = \frac{-1}{2\mu R^2}\frac{\partial}{\partial R}\left(R^2\frac{\partial}{\partial R}\right) + \frac{J^2}{2\mu R^2} \tag{34}$$

The first term on the right-hand side describes radial motions of the nuclei with respect to their center of mass, that is the nuclear vibrations, and the second term describes angular motion, that is molecular rotation, of the nuclei. J is the angular momentum operator and μ is the reduced mass of the system. To find the solution with K_N of this form, we split the wavefunction in a radial and an angular part, as we split the total wavefunction into electronic and nuclear in eq. 32:

$$\Psi_N(\vec{R}) = Y(\Theta,\phi)\frac{1}{R}X(R) \tag{35}$$

An illustration of molecular energy levels is shown in fig. 10

Rotational levels: to find the rotational energy levels, we need to solve

$$\left(\frac{J^2}{2\mu R^2} - E_{rot}\right)Y_{JM}(\Theta,\phi) = 0 \tag{36}$$

that, for a simple linear molecule, yields

$$E_{rot} = \frac{\hbar}{2\mu R_e}J(J+1) \equiv B_eJ(J+1) \tag{37}$$

where the nuclei are at a fixed separation R_e, B_e is the rotational constant at the equilibrium position and the rotational quantum number J can take the values $J = 0, 1, 2, \ldots$ For rotational radiative transitions, which require the molecule to possess an electric dipole moment, the selection rules allow $\Delta J = \pm1$. For homonuclear molecules (like H_2 and O_2), which have no electric dipole, no electric-dipole transitions exist: with lower transition probability

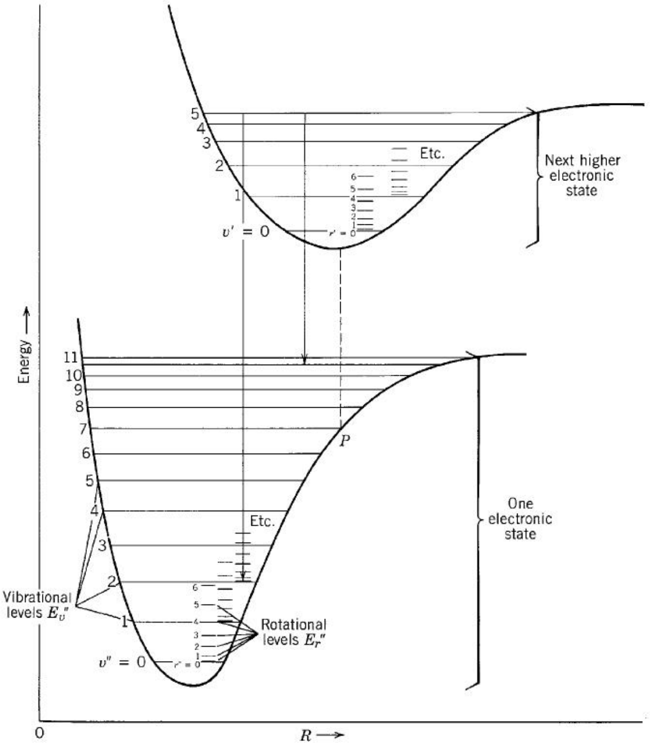

Figure 10: Illustrating the molecular energy versus internuclear separation curves for two electronic states. Each electronic state has its own set of vibrational levels, and each vibrational level has its own set of rotational levels.
[R. Eisberg and R. Resnik. Quantum physics 2^{nd} *ed. Wiley, 1985.]*

electric quadrupole transitions are allowed with $\Delta J = \pm 2$.

Vibrational levels: in this case we need to solve

$$\left(\frac{-1}{2\mu R^2} \frac{\partial}{\partial R} + E_e(R) + \frac{J(J+1)}{2\mu R^2} - E_{vib} \right) X(R) = 0 \qquad (38)$$

taking $J = 0$ and expanding E_e around the minimum, keeping that the molecule remains bound, we obtain:

$$E_e = E_e^{min}(R_e) + \frac{1}{2} \left(\frac{d^2}{dR^2} E_e \right) (R - R_e)^2 + \dots \qquad (39)$$

$$= -D_e + \frac{1}{2} k (R - R_e)^2 \qquad (40)$$

being D_e the dissociation energy. This equation, valid around the minimum of electronic bound states, describes a harmonic oscillator, with solutions $E = -D_e + E_{vib}$ and $E_{vib} = \hbar\omega_e\left(v + \frac{1}{2}\right)$, $v = 0, 1, 2, \ldots$ and $\omega_e = \sqrt{k/\mu}$. Unlike in the case of rotational energy, the $v = 0$ level has $E_{vib} = \hbar\omega_e/2 \neq 0$. Also, in the approximation of harmonic oscillator, the energy levels have equal spacing: but, as the real potential is anharmonic, as v rises the energy spacing decrease, while the period of oscillation increase.

Electronic levels: to calculate the energy levels of the electrons, the nuclei can be considered fixed in space. Nevertheless, the electronic energy level structure of molecules is fairly complex, and the details about how to calculate them from spectroscopic data and with numerical calculations will be described in the next section.

Approximation for real potential curves and higher vibrational states. In the previous paragraph, the vibrational levels have been calculated by approximating the electronic potential to a harmonic oscillator through the Taylor polynomial expansion in terms of $(R - R_e)$, truncated at the second order. Such approximation can be valid at the bottom of the potential, but for higher vibrational levels, to whom we are interested in the work here presented, the real anharmonic potential has to be considered.
A moderately good approximation to the true potential is given by the widely used *Morse Potential*:

$$U_M(R - R_e) = D_e\{1 - \exp[-\beta(R - R_e)]\}^2 \tag{41}$$

where D_e is the dissociation potential, and

$$\beta = \omega_e/[2R_e(B_eD_e)^{1/2}] = \omega_e(2\pi^2 c\mu/D_eh)^{1/2} \tag{42}$$

which, in the case of H_2 becomes $\beta = 0.12226\omega_e/D_e^{1/2}$ (ω_e and D_e in cm^{-1} and β in $\mathring{A}^{-1}$). Only three molecular parameters R_e, ω_e and D_e are required. Other methods can provide an improvement to this potential. *Hulburt and Hirschfelder* have given the following equation, which makes use of two additional molecular constants, $\omega_e\chi_e$ and α_e:

$$\begin{aligned} U_{HH}(R - R_e) = {} & U_M(R - R_e) + \\ & + CD_e\beta^3(R - R_e)^3[1 + b\beta(R - R_e)]\exp[-2\beta(R - R_e)] \end{aligned} \tag{43}$$

where

$$C = 1 - \frac{1 + \alpha_e W_e / 6B_e^2}{\beta R_e} \tag{44}$$

$$b = 2 - \frac{1}{C}\left[\frac{7}{12} - \frac{1}{\beta^2 R_e^2}\left(\frac{5}{4} + \frac{5\alpha_e^2 \omega_e}{144 B_e^4} - \frac{2\omega_e \chi_e}{3B_e}\right)\right] \tag{45}$$

Those five constants are available in the Atomic Data for most excited states of H_2 since the '70s. Those potential-energy curves are generated from spectroscopic data; the most general method to obtain them is the semi-classical *Rydberg-Klein-Rees method* (RKR). *Gilmore* [32] provides a thorough discussion on this method and developed a numerical method and a computer program to obtain the potential curves.

The *Morse Potential* can be solved analytically and allows already to obtain eigenstates and eigenvalues for the vibrational levels which are more realistic than the ones obtained with the harmonic oscillator approximation. The spacing between vibrational states is not anymore constant, as the eigenvalues of the energy are expressed as:

$$E_{vib} = \hbar\omega_e \left(v + \frac{1}{2}\right) - \frac{\left[\hbar\omega_e \left(v + \frac{1}{2}\right)\right]^2}{4D_e} \tag{46}$$

Eq. 46 is often found in the spectroscopic notation:

$$\frac{E_{vib}}{\hbar c} = \omega_e \left(v + \frac{1}{2}\right) - \omega_e \chi_e \left(v + \frac{1}{2}\right)^2 \tag{47}$$

where ω_e is a wavenumber in cm^{-1} and χ_e is the anharmonicity parameter. It is clear that in both equations 46 and 47 that they can be valid only as long as

$$\omega_e \chi_e \left(v + \frac{1}{2}\right) \leq \omega_e \tag{48}$$

that is, the anharmonicity correction can not be larger than the spacing between the vibrational levels in the harmonic oscillator. This means that there exists a v_{max} so that the equations 46 and 47 are valid only for $v \leq v_{max}$. This is in agreement with the fact that the Morse potential has only a limited number of bound vibrational states: as long as $E_{vib} \geq D_e$, the energy spectrum becomes continuous and the vibrational oscillations degenerate into the dissociation of the molecule.

The effects of the anharmonic potential on the vibrational periods can be seen in fig. 40 from sec. 4.6, where the calculated vibrational periods, for the vibrational levels from different electronic configurations, are shown.

So far, thanks to the Born-Oppenheimer approximation, we have divided the total wavefunction Ψ into three independent ones, the electronic $\Psi_e(\vec{x}, \vec{R}')$, the vibrational $X(R)$ and the rotational $Y(\Theta, \phi)$, with related energies E_e, E_{vib} and E_{rot}. This approximation has been motivated *a priori* considering that the difference between the mass of the nuclei and the mass of the electron is of 3 or 5 orders of magnitude. *A posteriori*, it is confirmed by the actual energy difference found between electronic, vibrational and rotational transitions. In H_2, which is the lightest molecule, consecutive electronic levels have energy differences between $\approx 10eV$ and less than $1eV$ for the ones which are very close; the separation between the first vibrational levels in the electronic ground state is $\backsimeq 0.5eV$; the minimum separation between rotational levels is $\backsimeq 7meV$, while the minimum energy gap in an allowed transition is $44meV$.

Dissociative ionization: role of bonding and anti-bonding states As anticipated above, when a molecule is excited so that $E_{vib} \approx D_e$, it will dissociate into its components. This is not the only channel to achieve dissociation: it can be produced also through the excitation of an anti-bonding state. We restrict now the discussion to the homo-nuclear diatomic molecules considered in the rest of this thesis: O_2 and H_2.

Neutral dissociation and dissociative ionization: considering a molecule initially in the ground state, then excited in laser interaction by one or more photon absorption, it can dissociate in the following ways:

$$H_2 + h\nu \to H + H \qquad O_2 + h\nu \to O + O \tag{49}$$

$$H_2 + h\nu \to H + H^+ + e^- \qquad O_2 + h\nu \to O + O^+ + e^- \tag{50}$$

From now on we will only consider the dissociative ionization by the process described in the reaction 50. We will not consider the neutral dissociation, described by the reaction 49, for the following reasons:

- experimentally, it is much easier to detect ions rather than neutral species;
- our experimental set-up is optimized to provide photons whose energy can typically excite the ionized rather than the neutral dissociation;
- neutral dissociative states differ from neutral bonding states by the electron spin configuration, which can not be changed by the interaction with photons, making such states unaccessible

The last point has key importance in the future discussions: it means that, while neutral dissociation can take place only through the neutral bond states, two channels can lead to dissociative ionization. It can take place either through the excitation of an ionized dissociative state, either through the excitation of high vibrational levels in ionized bound states.

The role of bonding and anti-bonding states: two possible channels can lead the molecule to its dissociative ionization. Experimentally it is possible to distinguish their contributions by measuring the kinetic energy of the fragments.
Let us consider a molecule (H_2, for instance, as in fig. 11) that is excited, by one or more photon absorption, to gain, within the Franck-Condon region, a certain energy E_T, and that this energy is large enough to be above a dissociative (*anti-bonding*) state of the ion (could be the $2p\sigma_u$ for H_2: see also fig. 33 in sec. 4.2). Classically, the Franck-Condon principle is the approximation that an electronic transition is most likely to occur without changes in the positions of the nuclei in the molecule. The resulting transition is vertical and occurs within the region of the internuclear distances allowed in the initial state. This energy E_T would be also larger than the dissociation energy D_e^+ of the parent ion (H_2^+) and also of some of its bound states (in the case of H_2, of all the bound states, but this may not be the case in other molecules: see, for instance, the energy levels of O_2, fig. 41 sec. 5.1). The way the energy E_T is shared between the ionized molecule and the ejected electron depends on which level is involved: specifically, if it is a dissociative level or a bound state, and, in this case, on which vibrational levels. The problem of calculating the probabilities for each of the two processes will be considered in sec. 4.2. In case the anti-bonding level is involved, the electron is ejected with energy $K_e = E_T - E_D$, and the molecular ion remains with an energy $E_D > D_e^+$; then the nuclei are accelerated apart by the repulsive potential, and the molecular (H_2^+) ion is dissociated into a neutral (H) and an ionized (H^+) atom. The energy $\Delta E = E_D - D_e^+$ is converted into kinetic or, eventually, internal energy of the fragments. If the internal energy is zero, then all the ΔE is converted into kinetic energy of the fragments.
In case the bound levels are involved, a larger amount of energy is converted into the kinetic energy of the ejected electron, but the molecular ion may still have enough energy to dissociate. It is very important to notice that in this case its fragments may still have some internal energy, but their kinetic energy is zero: the dissociation takes place through the higher vibrational states of a bound state, whose energy can be at most equal to D_e^+. If in an

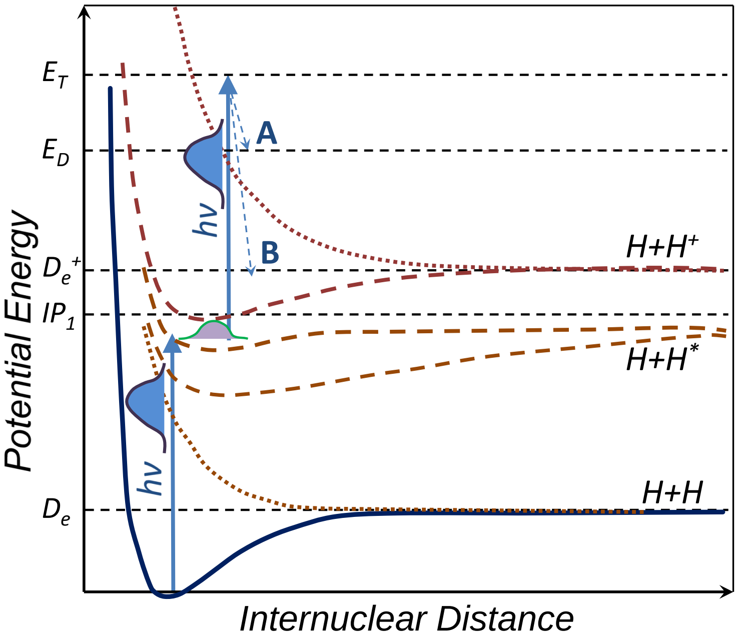

Figure 11: Possible scenarios for dissociation and ionization in H_2.
Blue solid line, ground level. Zero energy is set to its first vibrational level. Orange lines, neutral excited levels. Red lines, ionized levels. Dashed lines, bound states. Dotted lines, dissociative states.
D_e: dissociation energy of the neutral molecule. Two neutral H are released.
IP_1: first ionization potential.
D_e^+: dissociation energy of the ionized molecule. H and H^+ are released.
E_T: total energy acquired by the molecule by one or more photon absorption.
E_D: energy of the molecular ion in a dissociative state, after the ejection of the electron.
With the absorption of one or more photons until $E_T > D_e^+$, dissociative (case A) or bound states (case B) can be excited. The dashed arrows represent the energy lost by the molecule in the form of kinetic energy of the ejected electron (EKE). Note that such transition is vertical: arrows are slightly tilted just for graphical reasons.

experiment it is possible, among the charged fragments (H^+), to distinguish the ones with zero kinetic energy from the ones with non-zero kinetic energy, then information about the levels involved can be retrieved.

1.7 The pump-probe studies in molecular wavepacket dynamics

Pump-probe is a simple and widely used experimental technique for the time-resolved investigation of ultra-fast dynamics.
In the experiments with H_2 and O_2, which will be exhaustively presented in sec. 4 and 5.1, respectively, the molecular wavepacket dynamics are investigated through XUV pump - XUV probe technique. The first XUV pulse, the pump, coherently excites some of the neutral electronic and all their vibrational (vibronic is the term used for vibrational and electronic) wave packets; a second XUV pulse probes the wave packet evolution through ionization and dissociation. The vibrational wave packet in the excitation of a single electronic bound state can be written as:

$$|\psi_n(x,t)\rangle = \sum_m a_m \exp\left[-iE_m t/\hbar\right]|m\rangle \tag{51}$$

where $|m\rangle$ is the set of vibrational eigenstates, E_m their eigenvalues and a_m the constant coefficients. For short laser pulses, the energy bandwidth (see, for instance, fig. 35 in sec. 4.6) is large enough that the excitation of multiple electronic states has to be considered:

$$|\psi_{tot}(x,t)\rangle = \sum_{n=1}^{N}|\psi_n(x,t)\rangle = \sum_{n=1}^{N}\sum_{m_n=0}^{M_n} a_{m_n}\exp\left[-iE_{m_n}t/\hbar\right]|m_n\rangle \tag{52}$$

where now $|m_n\rangle$ is the set of vibrational eigenstates for each of the N electronic states considered, same for E_{m_n} and a_{m_n}. The interaction of the probe pulse with the excited molecule produces:

$$\langle f|\vec{\mu}\cdot\vec{E}|\psi_{tot}(x,t)\rangle = \sum_{n=1}^{N}\sum_{m_n=0}^{M_n} c_{m_n}\exp\left[-iE_{m_n}t/\hbar\right]|m_n\rangle \tag{53}$$

$$c_{m_n} = a_{m_n}\langle f|\vec{\mu}\cdot\vec{E}|m_n\rangle = a_{m_n}\mu_{m_n} \tag{54}$$

where $\langle f|$ is the final ionic state, $\vec{\mu}$ the transition dipole, $\vec{E}$ the electric field vector of the probe laser.

The signal, or the ion yield, is:

$$\begin{aligned} Y(t) = |\langle f|\vec{\mu}\cdot\vec{E}|\psi_{tot}(x,t)\rangle|^2 = \sum_{n,n'}\sum_{m,m'} c_{m_n} c^*_{m'_n} \cdot c_{m_n} c^*_{m_{n'}} \cdot \\ \cdot \exp\left[-i\left(E_{m_n} - E_{m'_n}\right) t/\hbar\right] \cdot \exp\left[-i\left(E_{m_n} - E_{m_{n'}}\right) t/\hbar\right] \end{aligned} \quad (55)$$

The ion yield is monitored as a function of the time delay between the pump and the probe pulse. Within the Frank-Condon picture, the ionization process is favored for certain particular internuclear separation R (named the Condon point), so a modulation is expected as the wave packets evolves through such detection windows. The evolution of the vibrational wave packet is related to the classical frequency of molecular vibration ω_e (and to the lower frequencies obtained for higher levels considering the anharmonic Morse potential). For example, in the simple case of the Condon point to be at a turning point, the ion yield would be expected to show a modulation with frequency ω_e. Considering that more than one electronic-vibrational state are involved, eq. 55 shows that the signal is composed of the beat frequencies between all pairs of energy levels that make up the wave packet.

2 The experimental setup

In the present work a CEP not stabilized, CPA, Ti:Sa laser system, with two separate beam lines, is used. One beam line has $1kHz$ repetition rate, $2mJ/pulse$, pulse duration $\tau_L = 35fs$, beam $\varnothing \approx 1cm$. The other line operates at $10Hz$, up to $160mJ/pulse$, pulse duration $\tau_L = 38fs$, with beam $\varnothing = 5cm$.

2.1 High-intensity XUV line

The main purpose of our laboratory is to generate, characterize and use coherent XUV radiation for investigating non-linear phenomena. This kind of experiments are performed in the "main set-up".
Fig. 12 shows a picture of the XUV line used in the present thesis. A schematic of the same line is shown in fig. 13. The IR beam, which exits the compressor, enters in the EUV vacuum line ($\approx 5 \cdot 10^{-6}mbar$ in the production area and at $\approx 4{\cdot}10^{-7}mbar$ in the detection area) through a selectable path, so that each diagnostic, optic or optical device can be selected or bypassed.

After the exit of the IR beam from the compressor, a feedback system (which is described in details in sec. 6.6) is used in order to improve the long term pointing stability of the laser beam. Pointing stability (which partially comes from thermal instabilities in the laser chain) is also an important issue which has to be considered for the improvement of the long term stability of the whole XUV line. A small amount of laser light passing through the first mirror is used to monitor the pointing stability. The detector consists of a mask with four holes along a circle in the peripheral part of the laser beam profile (which is about 5 cm diameter), a converging lens with focal length of about 30 cm and a 4-radiants photodiode ($1cm\varnothing$) with an integrated circuit for amplification and summation of the signal from the different channels. In this way, the photodiode measures the amount of light from 4 points in the peripheral part of the beam, which is obviously more sensitive to variations rather than the central part.A basic model oscilloscope is used as a digitizer, connected to a computer with USB interface. A Labview program reads the signal of the photodiode on the oscilloscope, takes a proper amount of averages, and compares the current values with the references taken in the beginning. When a drift is measured the programs adjusts, through the motion of picomotors, the orientation of the mirror which defines the laser pointing.
Before the vacuum line, the IR pulse duration can be measured with a SPIDER or a 3^{rd} order single-shot auto-correlator. The laser beam can pass

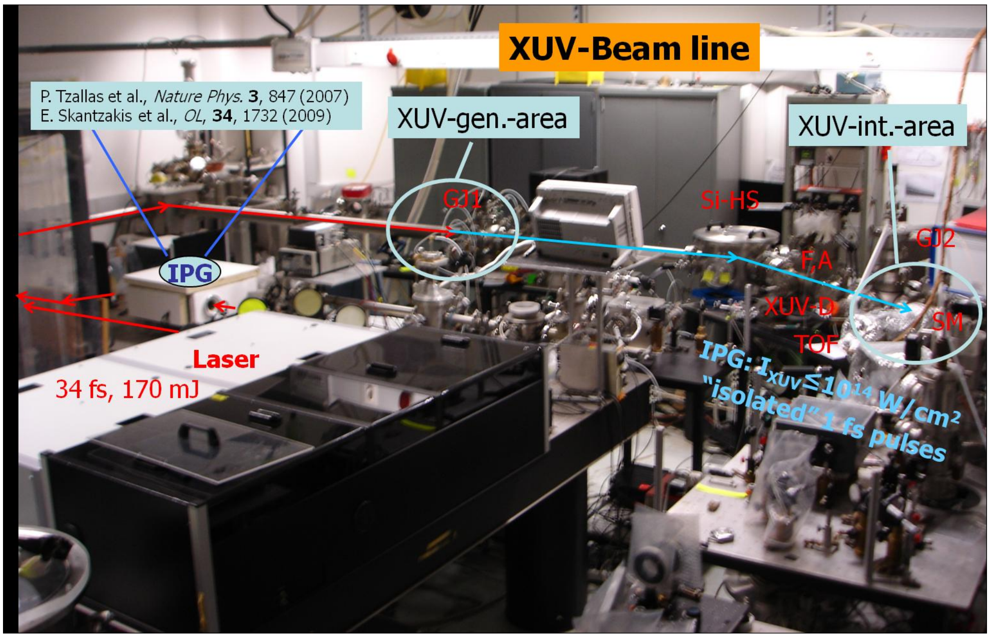

Figure 12: Main set-up and XUV line. *IPG:* Interferometric Polarization Gating. *GJ1:* gas jet 1, for HOHG. *Si-HS:* silicon plate, harmonic separation from IR. *F,A:* thin metal filters and apertures. *XUV-D:* XUV detection with calibrated photodiode or with MCP coupled to a phosphor screen. *GJ2:* gas jet 2, for the HOH interaction with the medium under investigation. *SM:* spherical, golden coated split mirror. *TOF:* time of flight spectrometer, for photoelectron energy spectra or ion mass spectra. *XUV-int area:* XUV interaction area, or detection area 1.

through the IPG-DMZ (see fig. 7(a) of sec. 1.3), which allows to achieve XUV continuum spectrum with focused intensities $I_{XUV} \approx 10^{13} W/cm^2$, which are enough to induce non-linear effects. The achievement of single-isolated attosecond pulses is limited by the lack of CEP stabilization in the laser system rather than by the technique itself. As a drawback, the alignment and the long term stability makes highly desirable the development of a more simple, compact and stable device, like the Collinear Polarization Gating (sec. 2.2).

The laser can be focused by a $6m$ lens (placed just before the entrance of the IR beam in the EUV vacuum line), or by a $3m$ lens (which has been placed in the EUV vacuum line). Here, the alignment and the insertion of the lens in the laser line can be adjusted with a mechanical mount, controlled through the vacuum by vacuum feedthroughs. Also, at a distance of $\approx 1.5m$ before the first gas jet, a similar support has been set to insert and align all the optics (that is, a BBO second harmonic crystal and a CaF_2 delay plate) needed for 2-color harmonic generation. Thus, the laser is focused in front of a piezoelectric controlled gas jet, either with the $6m$ (placed just before

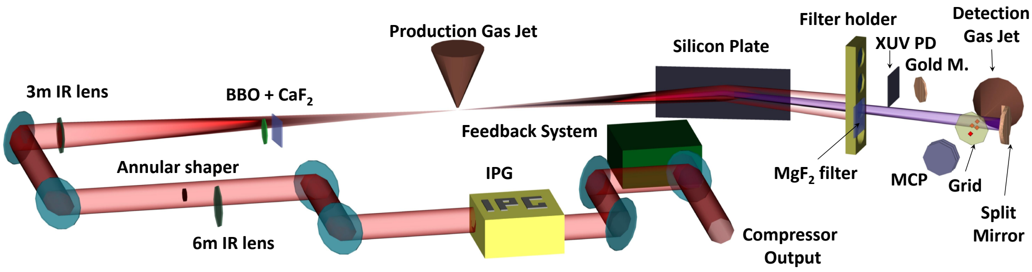

Figure 13: Schematic for main set-up, XUV line and detection area 1. In this representation, the annular shaped IR beam is focused by a $3m$ lens. The $6m$ lens, the BBO crystal and the CaF_2 plate are shown out of the IR beam. The XUV beam passes through one of the three thin ($150nm$) metal (Al, In, Sn) filters held in the filter holder (one slot is empty). A MgF_2 glass filter, the XUV photodiode *(XUV PD)*, a flat gold mirror *(Gold M.)* can be inserted in the XUV beam. The detection gas jet and the grid provide the electric field to accelerate the ions (represented here as red dots) to the MCP of the TOF.

the entrance of the IR beam in the EUV vacuum line) either with the $3m$ lens (which has been placed in a in the EUV vacuum line). The jet provides a laser-syncronized, $10Hz$ pulsed flow of gas (usually Xe as it provides the optimal efficiency of conversion for the harmonics in the plateau, but in general selectable between other noble gases) at high pressure (delivered pressure is adjustable in the $mbar$ range; backing pressure is $2.5bar$) for the XUV generation.

Also a magnetic valve pulsed jet has been installed. The reason for this redundancy is the study of quasi phase-matching through the use of multiple gas jet. This study has not been performed, but the magnetic jet can be useful in case of problems: despite the lower performances in terms of minimum opening time ($300\mu s$ compared to the $150\mu s$ of the piezoelectric one) and precision, this magnetic jet is more robust, and its driving electronic is more reliable, simpler, cheaper and requires at most $100V$ instead of $200V$ - $500V$.

The delicate requirements for the background pressure ($P_{back} \approx 4 \cdot 10^{-7} mbar$) in the detection area are fulfilled by differential pumping.

After the interaction of the IR beam with Xenon in the production gas jet, XUV and IR pulses co-propagate towards the detection chamber: a silicon plate at Brewster angle (75°) reflects the XUV and absorbs most of the IR. A mechanic stage, movable under vacuum, allows to choose between two silicon plates with opposite orientation, so that the XUV radiation can be selectively directed to one of the two available detection areas. The two detection areas are structured the same way, so that they both have selectable combinations of pin-holes, masks and thin metal filters to adjust the profile and to modulate the spectrum of the XUV beam, shutters to separate them from the rest of the set-up, independent high vacuum system and indicators, high-voltage floated pulsed gas jet, a spherical golden mirror with $f = 5cm$ to focus the XUV radiation in front of this jet, but are equipped with different diagnostic. The detection area 1 is mainly for pump-probe experiments. It is equipped with a golden coated spherical split mirror, mounted on piezo-controlled close-loop stage, so that it acts both as wavefront divider and as delay line. A Time of Flight (TOF) spectrometer, which can be set to work either as an ion mass spectrometer or as an electron energy spectrometer, measures the product of the interaction.

The detection area 2 is equipped with an ion microscope, a detecting device composed of a system of high voltage electrostatic lenses and a gated Multi Channel Plate (MCP) detector coupled with a phosphor screen. Its purpose, like an optical microscope, is to produce on a detector the magnified image of an object. In this case, the object is the spatial distribution of the atoms ionized in the focus of the XUV beam. The electrostatic lenses, obtained by a proper configuration of ring-shaped anode and cathode, guide the ions from the XUV-gas interaction area to the detector, analogous to the way an optical system assists in the transport of light in an optical instrument. The detector can be set to operate continuously or in gated mode. In the first case, it collects all the ionized species; in the second case, it is possible to discriminate particles with different charge to mass ratio, thanks to their different time of arrival on the MCP plates. For instance, if Ar is being used, and both Ar^+ and Ar^{2+} are produced, the user can choose whether to detect Ar^+, Ar^{2+} or both together. From the phosphor screen coupled to the MCP, a camera collects the spatially resolved, time integrated image of the spatial distribution of the selected ionized species. If no saturation occurs in any of the stages, the intensity of the image is related to the time-integrated concentration of ions. The ion microscope has been used for the measurement of the XUV focal spot size in the interaction region and for *Revealing the quantum path details in high-field physics* (submitted).

Additionally, in order to improve the collection efficiency and the PES resolution, a magnetic bottle has been constructed and used in the present XUV line. This device has been mainly used for the detection of the Two Photon Double Direct Ionization (TPDDI) Photoelectron Energy Spectrum (PES) signal, which is described in sec. 3.3. A detailed description of the device is provided in sec. 6.4

2.2 Collinear Polarization Gating

The Collinear Polarization Gating (CPG) device is based on the same principle as the IPG device and on eqs. 24- 27, but it is user friendly and it provides

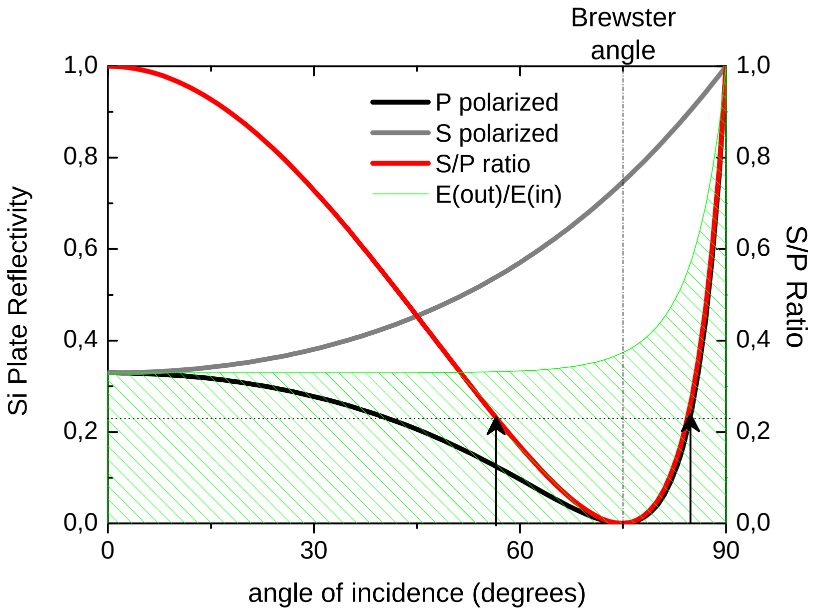

Figure 14: Reflectivity for S and P polarized light at 800nm on the silicon plate. The ratio between the total reflected energy and the total incoming one is shown as a shaded area on the graph. We see that, by adjusting the angle of incidence it is possible to select the desired intensity ratio between the two polarizations. For each value of the ratio there are two angles which determine it, one smaller and one larger than the Brewster angle.

long term stability. The device consists of the following four elements:

- a $\lambda/2$ plate is used just to rotate the polarization of the laser, which usually enters as horizontal and is rotated to 45°
- a multi order (MO) $\lambda/4$ plate, which splits the pulse into two with perpendicular polarization and phase shift of $(n+1/4)\lambda$, corresponding to a delay of about $38fs$ and phase difference of $\lambda/4$
- a zero order (ZO) $\lambda/4$ phase, whose purpose is as explained above
- a silicon plate, mounted on a rotating stage with an angle of incidence $\approx 60°$ which can be finely tuned to adjust the ratio between the electric fields.

The MO $\lambda/4$ and ZO $\lambda/4$ plates play the role of the beam splitter and re-combiner in the IPG, while the Si plate has been introduced in order to control the relative amplitudes between the perpendicularly polarized pulses. The amplitude ratio of the two perpendicularly polarized fields can be controlled by changing the angle of incidence Θ on the silicon (Si) plate as shown

in fig. 14. Silicon plates are commonly used in the attosecond community for the separation of the IR beam from the XUV radiation. In their present mission to control the amplitude ratio of the two fields, the width τ_g of the formed gate is given by the relation of eq.24 in sec.1.3. With this modification we managed to apply the gating technique with the wave-plate scheme, originally efficient only for few-cycle laser systems, to our multi-cycle laser. The CPG totally relies on collinear geometry, but we manage to reproduce the same conditions as in the IPG-DMZ for the elliptical modulation of the pulse, thus using the same model and achieving almost the same results.
The details of the experiment and the results can be found in the related article [42]. Despite the positive results obtained, the CPG could not be used for XUV-pump XUV probe experiments. This is because the energy output is slightly lower than that of IPG (as can be seen in fig. 14: 32%, while for the IPG in DMZ arrangement it is 50%). From this figure we can also see that we may obtain the same results but with an higher output ($\geq$ 50%) energy by switching to almost grazing incidence: the problem in this case would be just that a much longer silicon plate would be required. Another solution is the use of a dedicated dielectric optical element.

3 Characterization of the XUV beam

3.1 High photon flux XUV source

In order to induce non-linear phenomena with XUV light, it is necessary first to produce high-intensity XUV radiation.
As explained in [2, 31], the relative position of the laser focus and the production gas jet plays a key role in the total efficiency of conversion from IR to XUV, due to the phase matching conditions given in eq. 16 of sec. 1.1. From previous studies [46] the general behavior is known:

- By focusing the laser at $z = +b/2$ (being b the confocal parameter) after the production gas jet the conversion efficiency is maximized, the harmonics are mainly generated by the recombination of long electron trajectories and the spectral phase distribution of the XUV radiation is not the optimum for the formation of the asec pulses

- By focusing the laser on the production gas jet ($z = 0$), the conversion efficiency is reduced approximately by a factor of 3 compared to the case where the focus is placed after the gas jet, the harmonics are generated by the recombination of short and long electron trajectories and the spectral phase distribution of the XUV radiation is not the optimum for the formation of the asec pulses

- By focusing the laser at $z = -b/2$ before the production gas jet, the conversion efficiency is approximately the same compared to the case where the focus is placed on the gas jet, the harmonics are mainly generated by the recombination of short electron trajectories and the spectral phase distribution of the XUV radiation is the optimum for the formation of the asec pulses. In this case the divergence of the XUV beam is expected to be smaller compared to the the divergence of the XUV which is generated by the long electron trajectories. The different divergence between the harmonics generated by the short and long electron trajectories is associated to the gradient forces applied on the electron trajectories by the intensity variation of IR beam along the beam cross section.

The above mentioned features are shown in fig. 15 (red and black lines) and fig. 16. Using the knife edge technique, a MgF_2 plate can be inserted in the harmonic beam by a mechanic feedthrough with 1/100 of inch precision ($0.025mm$). Fig. 16(a) shows a knife edge measurement: the signal represents the integral of the 2D XUV beam over the one dimension of the plate

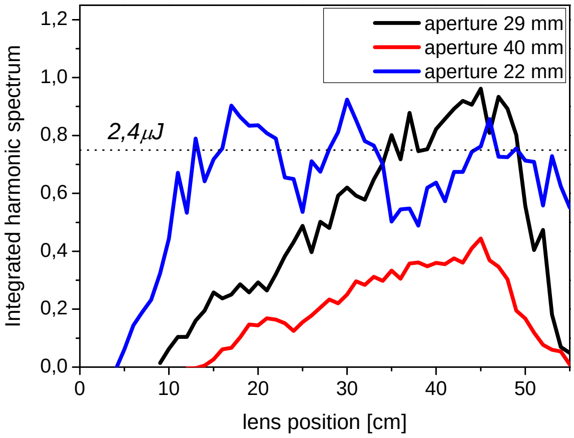

Figure 15: Integrated photoelectron signal as a function of the $6m$ lens position and different beam diameters. Relative intensity of the traces is adapted according to successive measurements. The energy has been measured by using an XUV calibrated photodiode and found to be approximately $2.4\mu J$ just after the generation gas. This value is found to be approximately the same for $3m$ and $6m$ lens, although further studies are required in this direction by using the $6m$ lens.

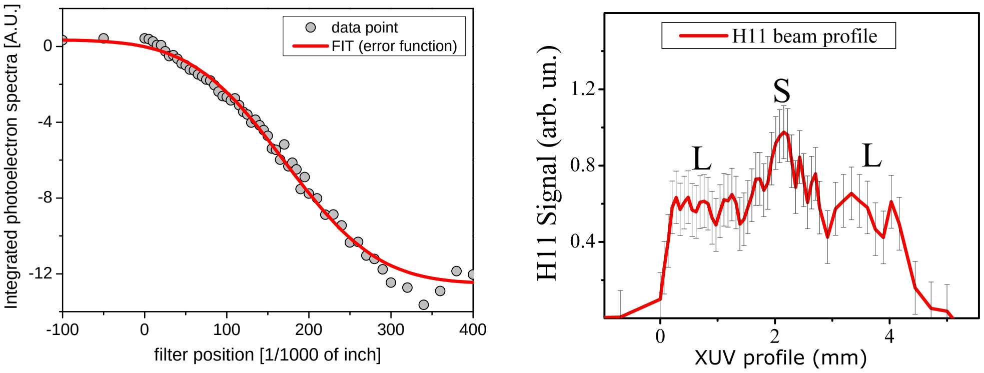

(a) (b)

Figure 16: Knife edge characterization of the XUV beam profile. On the left, data points are fit with error function, in order to determine the XUV beam diameter. On the right, their derivative shows the structure of the XUV beam profile. Short trajectories contribute mainly to the central part, long trajectories to the outer one. (a): Black dots are integrated photoelectron signal as a function of filter insertion. Red curve is the fit with error function. Note that higher signals have negative values: random fluctuations are stronger for high signal, bottom right of the plot. (b): Beam profile of the 11^{th} harmonic on the surface of the gold spherical mirror determined by means of knife-edge technique. The beam profile and the diameter of the 13^{th} and 15^{th} harmonics (for simplicity are not shown here) are approximately the same with the 11^{th}.

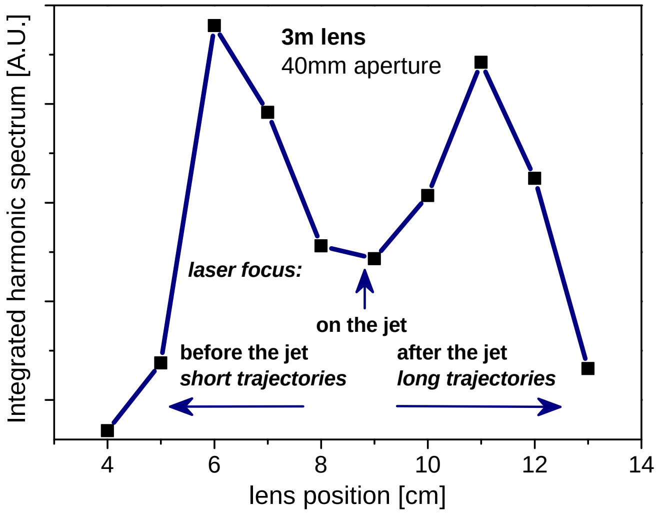

Figure 17: Integrated photoelectron signal as a function of the $3m$ lens position with $40mm\varnothing$ aperture.

movement:

$$S(\bar{x}) = \int_{0}^{\bar{x}} dx \int_{-\infty}^{+\infty} dy I(x,y) \tag{56}$$

The data points are fitted with an error function, which is defined as the integral function of the Gaussian. XUV beam diameters, obtained with the $6m$ lens for different focal position and different IR beam diameters, are shown in tab. 1. Since we measure the PES, spectrally resolved profile measurement are available. For instance, in fig. 16(b), obtained as the first derivative of a knife edge measurement, the profile of only the 11^{th} harmonic is shown. The contribution from short trajectories appears as a peak on the pedestal of the contribution from long trajectories.

In case where the laser intensity exceeds the ionization saturation intensity of the medium, the phase matching conditions are not valid any more and the macroscopic emission drops while temporal localization of the attosecond pulse is expected to be worse due to large plasma formation. This is clearly shown in fig. 15 (blue line) and in fig. 17, where the intensity of the IR field is larger due to tighter focusing. While PES show the spectral characteristics of the XUV beam, and the ion mass spectra are convenient to identify the nonlinear processes, since the amount of the signal is larger compared to the PE signal, the energy content has to be measured with a calibrated photodiode.

XUV beam diameter [mm]			
lens position [cm]	IR [mm]		
	22	29	40
25	1.3 ± 0.1	1.45 ± 0.08	1.9 ± 0.25
35	1.6 ± 0.1	1.65 ± 0.1	2.2 ± 0.2
45	1.4 ± 0.3	2.6 ± 0.4	2.2 ± 0.2

Table 1: XUV beam diameter with $6m$ lens, for different lens positions and laser apertures.

As the photon energy for XUV is far above ($E_{h\nu} \gg 1eV$) the typical energy gap of semiconductors, the photodiode does not need any external power supply. It provides a charge $Q = k(\hbar\omega)E_{XUV}$, directly proportional to the energy of the incident radiation. This charge can be obtained by integrating the signal $V(t)$ on the oscilloscope:

$$Q = \frac{1}{R}\int dt \cdot V(t) \tag{57}$$

where $R = 50\Omega$ is the resistance applied to the coaxial cable. The proportionality factor $k = k(\hbar\omega)$ depends on the photon energy, its calibration curve is provided by the constructor. The relative contribution of different harmonics is known by PES spectra. Typical energy values are $2.4\mu J$ for HOH and $80nJ$ for the XUV coherent continuum. These values are the energy content at the generation. In order to estimate the energy of the XUV in the interaction region, the reflectivity of the silicon plate and the transmission through the thin metal filter have to be taken into account. Once the temporal duration and the energy of the XUV beam are known, by mea-

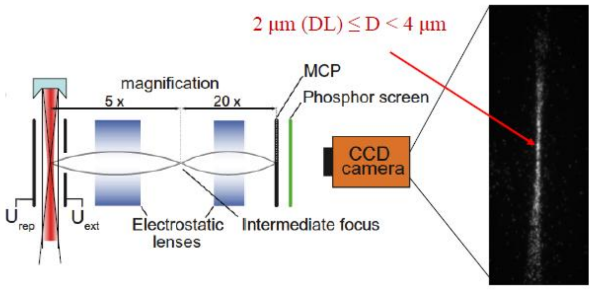

Figure 18: Imaging of the XUV focal spot by an ion microscope. The measured focal spot diameter is $2\mu m \leq D \leq 4\mu m$.

suring the XUV focal spot size it is possible to calculate also the absolute intensity value at the XUV focus.

As explained in sec 2.1, the ion microscope can be used to collect magnified images of the spatial ion distribution in the XUV focal spot, thus providing different types of information. Fig. 18 shows an image of the focal spot from the full XUV beam. The spot diameter D of the XUV beam is measured to be $2\mu m \leq D \leq 4\mu m$.

Concluding this section, by using a loose focusing configuration ($6m$, $3m$ focal length lenses) we are able to generate harmonic radiation in the $15-25eV$ spectral region, with energy in the few μJ regime and divergence $\approx 3mrad$. In the interaction region, taking into account the energy of the XUV beam ($\approx 100nJ$ for the train of attosecond pulses and $\approx 10nJ$ for isolated attosecond pulses), the focal spot diameter of the XUV radiation, and, assuming the pulse duration of the train of asec pulses is following the conventional non-linear law, i.e. $T_{XUV} = T_L/\sqrt{p}$ (being $p = 4$ the order of non-linearity of the process) and assuming for the isolated asec pulse a Fourier transform-limited duration of $0.5fs$, it is estimated that the intensity of the HOH can be as high as $I = 10^{14}W/cm^2$. This intensity value is sufficient to induce non-linear processes in matter and to perform pump-probe experiments in the XUV spectral range.

3.2 Multiple ionization of noble gases using XUV radiation.

It has been observed [8], fig. 19, that XUV radiation, spectrally modulated by a $150nm$ thick Sn filter, multiply ionizes Ar atoms. Indeed, this is strong evidence of the high intensity of the XUV source.

In a previous work [8], using one-color generated HOH spectrally modulated by $150nm$ thick Sn filter, multiple ionization of Ar and Kr atoms has been observed. In this work we made the same observation using both one-color and 2-color generated HOH. Fig. 19 shows a representative ion mass spectrum, which has been recorded using harmonics generated by a 2-color field. Similar spectra (for simplicity are not shown here) have been recorded in case a single color field was used for the harmonic generation. Since the Sn filter heavily cuts the photon energies above $25eV$ ($T(\hbar\omega = 25eV) < 10^{-2}$, see also fig. 20), and since the $IP_2(Ar) = 43.39eV$, the observed yield of Ar^{2+} is due to multiple photon absorption from the XUV pulse. Two different processes contribute to the double ionization of atoms by multiple absorption of photons.

One is Sequential Double Ionization (SDI), in which the atom first ionizes

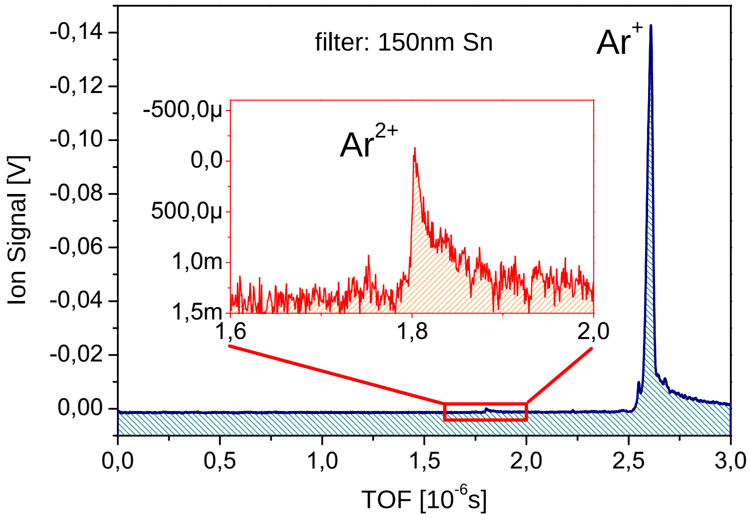

Figure 19: Ion Mass Spectrum with Ar, showing Ar^{+} and Ar^{2+} ions. This is one of the spectra collected in order to produce the plot in fig. 31. The difference in the amplitude between the peaks of the two differently ionized species is remarkable: it shows the difference in the probabilities of one-photon and two-photon process for the available XUV intensities.

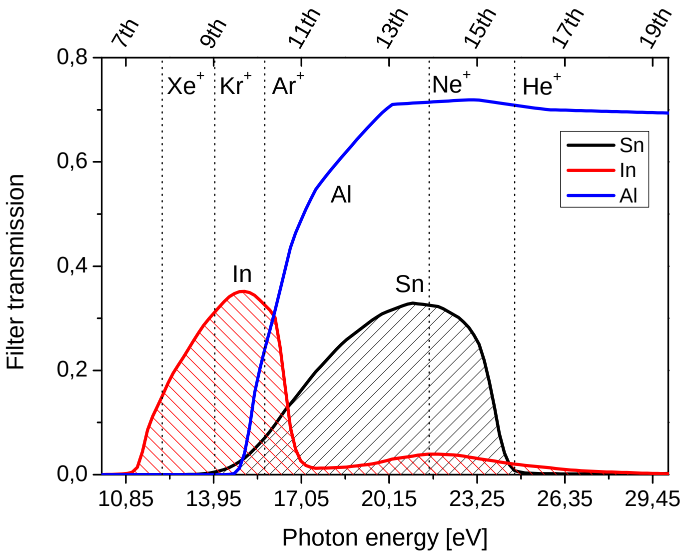

Figure 20: Filter transmission function for commonly used $150nm$ thick metal filters. Vertical dashed lines show the ionization potentials for noble gases. The energy values on X axis correspond to the energy of odd HOH, which are shown on top.

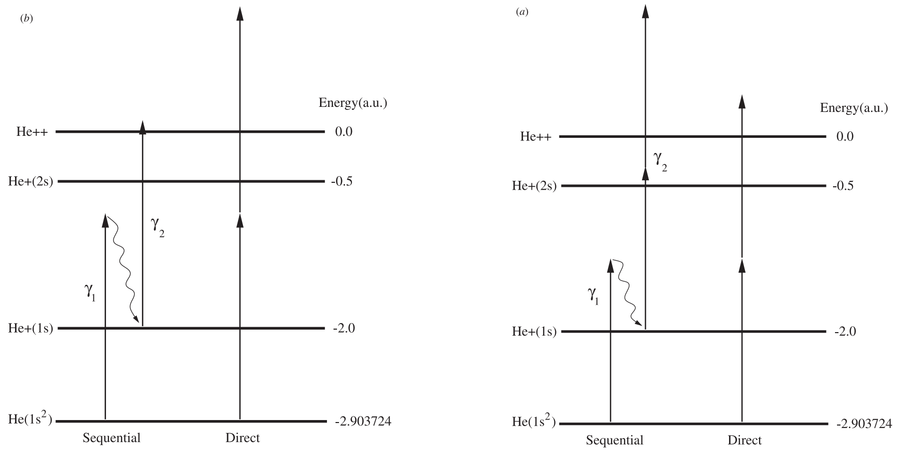

(a) (b)

Figure 21: Schematic representation of the levels of He of interest in [43]. In (a) it is shown the case where the sequential channel requires two (1 + 1) photons, and the diagram corresponds to the particular frequency $\hbar\omega = 2.05au$. In the case that $2\hbar\omega > IP_2$ and $\hbar\omega > (IP_2 - IP_1)$, both SDI and DDI are 2-photon processes. In (b) it is shown the case where the sequential channel requires three (1 + 2) photons, and this is exemplified for the photon frequency $\hbar\omega = 1.65au$. In the case that $IP_2 < 2\hbar\omega < 2(IP_2 - IP_1)$, the SDI is a 3-photon process, while DDI remains 2-photon. In both cases the direct channel requires two-photon absorption to be allowed. The quantities labeled γ_1 and γ_2 denote the ionization widths of $He(1s^2)$ and $He^+(1s)$, respectively. *[Kornberg and Lambropoulos. Journal of Physics B, 1999.]*

through single-electron ejection and, subsequently, the produced ion absorbs further photons to be doubly ionized. The other is Direct Double Ionization (DDI), in which two electrons are ejected simultaneously, sharing the excess energy once reaching the double continuum.

At high-field frequencies, i.e., in few-photon ionization, the sequential dominates the direct process if the nonlinearity order of both processes is the same. However, work by *Kornberg and Lambropoulos* [43] has pointed out that in specific schemes of high-frequency ionization the direct process might become more efficient than the sequential one. This is the case when the nonlinearity of the direct process is lower than the overall nonlinearity of the sequential one.

Briefly, in case of 2-photon, double ionization, it is required that:

$$2\hbar\omega > IP_2 \tag{58}$$

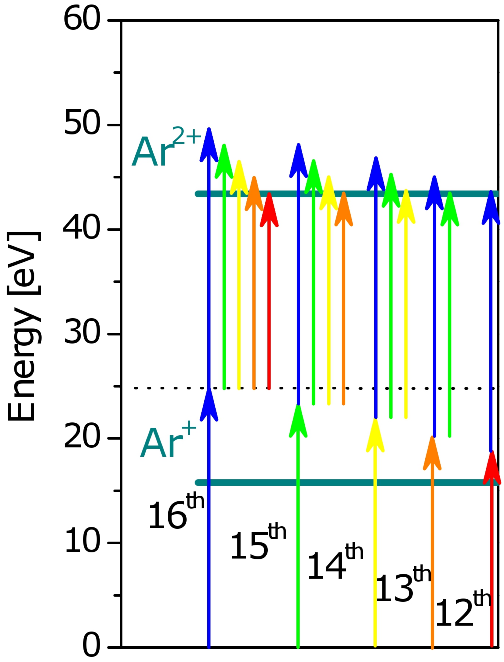

Figure 22: Excitation scheme for Ar. Ar^{2+}, in combination with Sn filter, is a suitable non-linear medium: it can be doubly ionized through 2-photon absorption by two harmonics, at the conditions that $q_{tot} \geq 28$ and each of them to be transmitted through the filter: as the 17^{th} is cut, HOH between the 12^{th} and the 16^{th} contribute to the yield of Ar^{2+}.

In the sequential process, the first photon ionizes the neutral atom, according to $X + h\nu \rightarrow X^+ + e^-$, then, with the absorption of the second photon by the ion, the second electron is ejected: $X^+ + h\nu \rightarrow X^{2+} + e^-$. This process requires, as shown also in fig. 21(a), that:

$$\hbar\omega > IP_2 - IP_1 \tag{59}$$

In the direct process two photons are absorbed by the atom and two electrons are simultaneously ejected: $X + 2h\nu \rightarrow X^{2+} + 2e^-$. If the photon energy is chosen so that:

$$IP_2 < 2\hbar\omega < 2(IP_2 - IP_1) \tag{60}$$

the DDI remains a second order process, while the SDI becomes a third order process, as shown in fig. 21(b).

In our case, where Ar has been used, DDI is expected to be the dominant process for photon energies $\hbar\omega < 2(IP_2 - IP_1) = 27.63eV = 17.82\hbar\omega_L$, where $\hbar\omega_L = 1.55eV$ is the energy of the IR driving field used for HOHG. As shown in fig. 22, in our case, where the harmonics were generated either by one-color or 2-color fields and spectrally shaped by the $150nm$ thick Sn filter, DDI in Ar occurs through the channels 12+16, 13+16, 13+15, 14+16, 14+15, 14+14, 15+16, 15+15, 16+16 in case where the harmonics were generated by 2-color field and the channels 13+15, 15+15 in case of one-color field. Since the TPDDI ion signal was relatively easy to measure with our set-up, a really demanding step towards the measurement of the PES signal resulting by this process has been attempted. The reason why this step is important but, at the same time highly demanding, is briefly expressed in [43]. *"The yield of the doubly ionized species as a function of the laser intensity may be the easiest to measure, but the photoelectron energy spectrum, or parts of it, can be a much more informative and discriminating quantity, whose detection is, however, usually much more demanding."*

In theoretical works [43, 48], large attention has been paid to the quest for the signature of the TPDDI process in the PES. The main feature of a PES obtained by the interaction with a train of HOH is the discrete peak structure. These theoretical works claim that photoelectrons from TPDDI should produce a continuum spectrum between $0eV$ and $2\hbar\omega - IP_2$,as illustrated in fig. 23, with slight peak structure at the edges and a sharp cut-off at these two values, which should represent a clear experimental signature. What

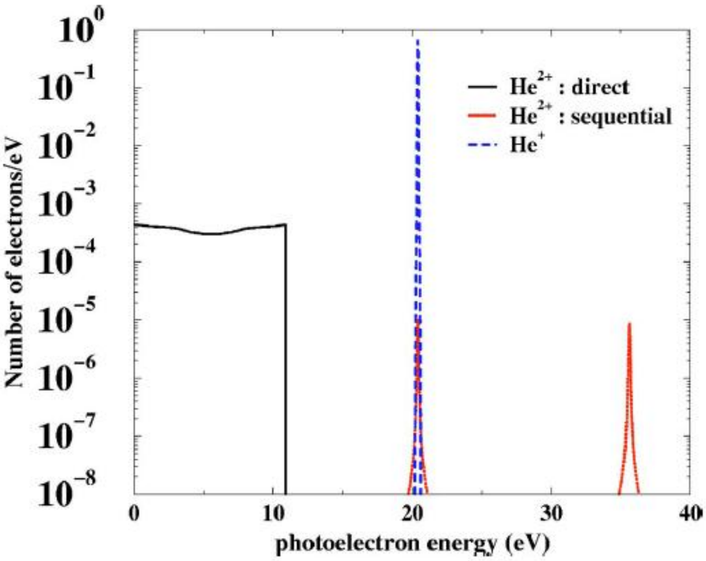

Figure 23: Two-photon PES of He under irradiation with a Gaussian pulse of photon energy $45eV$, peak intensity $10^{14} W/cm^2$, and $30fs$ duration. Only single-photon ionization to He^+ and 2-photon ionization of He^+ to He^{2+} have been considered, in addition to the direct one, with $\sigma_2 = 8.1 \cdot 10^{52} cm^4 s$. *[Lambropoulos, Nikolopoulos and Makris. PRA, 2005]*

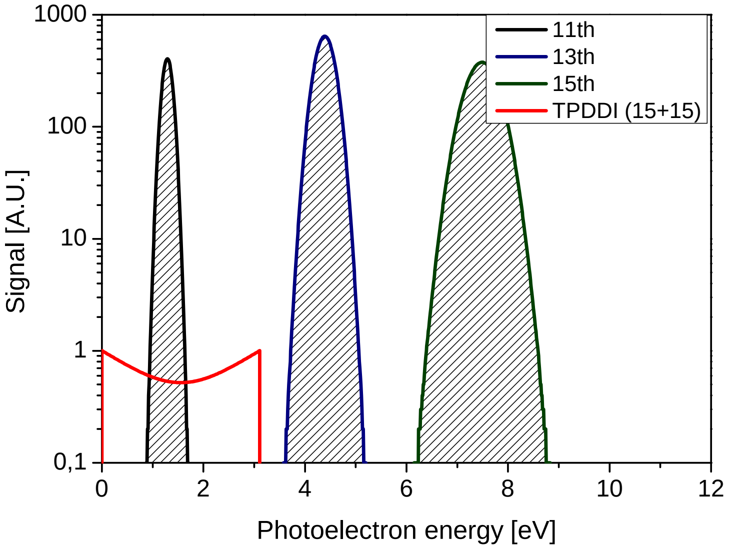

Figure 24: Estimated PES for Ar. The shaded area represents the photoelectrons from TPDDI, which are supposed to show a non-linear dependence on the HOH intensity, while the peaks from single photon absorption are linearly dependent.

is considered "an issue well beyond our expertise", is the possibility to distinguish such a signal from the noise of tails of the single-photon single-ionization peaks, which are orders of magnitude stronger. Also, while in the theoretical work the XUV radiation is assumed to be monochromatic, in experiments we shall not ignore the simultaneous presence of several HOHs. Despite being more suitable for calculations, He requires high intensities for too high photon energies to be achieved in our set-up. Ar, with its $IP_2 = 43.39eV = 28.3\hbar\omega$ and $IP_1 = 15.76eV$ is a suitable candidate: TPDDI from $15^{th} + 15^{th}$ would yield photoelectrons with a continuum energy spectrum, from 0 to $3.11eV$ (see fig. 24), which might be distinguishable from the tail of the 11^{th} harmonic (photoelectrons with $1.29eV$) and of the 13^{th} (photoelectrons with $4.39eV$).
In the most optimistic assumptions of XUV intensities ($10^{14}W/cm^2$) and of cross-section values (10^{-51}), a calculated ratio of $Y_{1ph}/Y_{2ph} < 10^3$ may allow us to expect to find an experimental proof by observing the behavior around $3.1eV$. This value is in agreement also with the yields of singly and doubly ionized species observed in ion mass spectra, as in fig. 19. In the series of data of that measurement, the integrated signals of the two species are in a ratio: $I\left(Ar^{+}\right)/I\left(Ar^{2+}\right) \leq 10^3$.

Unfortunately, it has to be considered also that:

- TPDDI electrons are not only continuously distributed in energy, so that their signal has even lower amplitude, but they may have a broader angular distribution;

- the tails of single photon, single ionization peaks are quite broad and do not go to zero;
- in PES acquired with focused XUV beam, a certain background signal is inevitable.

3.3 Experimental attempt on recording the TPDDI PE distribution in Ar and Kr

Usually PES are produced by the unfocused XUV beam interacting with the gas at the detection jet. As the beam is unfocused, only 1-photon processes can be seen. Thus PE produced by HOHs whose photon energy $\hbar\omega > IP_1$ for a given gas (see fig. 20) can be observed, and thus the spectral properties of the XUV beam can be monitored. In case our purpose is to observe a 2-photon process, which requires high intensities in order to take place, the PES must be taken with the XUV beam focused, by a part of the split mirror, in front of the detection jet. PES acquired as a function of the energy content of the XUV beam (varying the pressure in the production jet, for instance) may contain some peaks (or knees, or points) showing a non-linear behavior as compared to the others. Given that the main peaks of the spectrum come from 1-photon process, they can be taken as reference for the linear process, i.e. they represent the energy of the harmonics. All the other points of the PES can be compared with them to search for a power dependence of 2. As such non-linear points are close to zero-energy, we have to apply some negative extraction voltage (very few Volts: $2-6V$), otherwise their time of flight would tend to be infinite. Also, as the TPDDI signal is expected to be very weak (see ion mass spectra in [8], but also in fig. 19 of sec. 3.2), we increase the efficiency of collection of the photoelectrons by installing a magnetic bottle TOF (see sec.6.4 for details). In fig. 25 two PES, one for Ar with magnetic bottle, one for Kr with traditional TOF, are shown. They are both taken from one point in XUV power dependence series, which means that for each different value of XUV energy a PES is saved. Power-dependence analysis over all the collected PES series did not show any significant non-linearity. The main problems are related to the tails of the single photon peaks and with the background. Despite the fact that this experiment did not succeed, we realized which strategies and improvements need to be applied in the future:

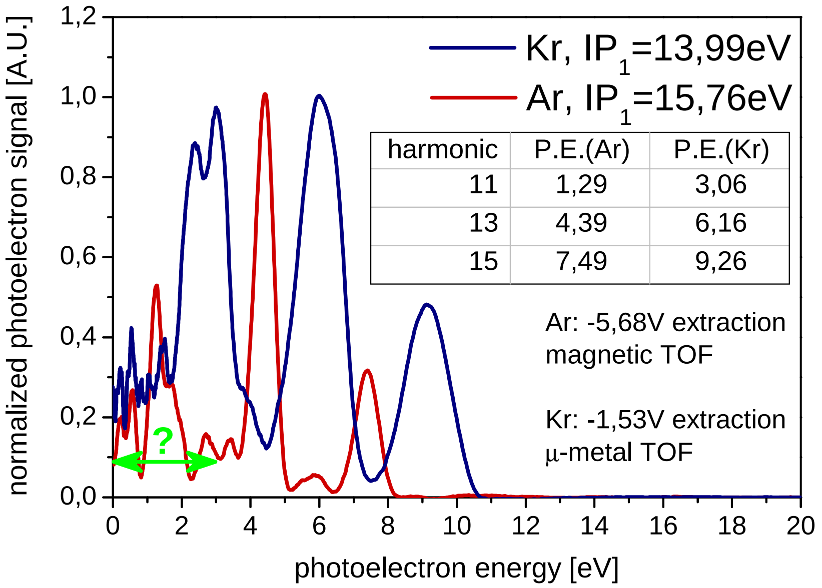

harmonic	P.E.(Ar)	P.E.(Kr)
11	1,29	3,06
13	4,39	6,16
15	7,49	9,26

Figure 25: PES for Kr (blue) and Ar (red), detected with traditional and magnetic bottle TOF, respectively. Note that also an extraction voltage is applied for a better collection of photoelectrons close to zero kinetic energy. PES are normalized in order to be comparable: in this case the larger amount of signal for the magnetic bottle TOF can not be appreciated, but its higher quality is evident.
Open question (green arrow): this PE distribution is in agreement with the expected values but additional measurements are required (like power dependence and angular distribution) in order to extract a safe conclusion. In these forthcoming measurements particular attention must be paid on the stability of the signal and the vacuum conditions.

- the single photon peaks have a narrow angular distribution: this means that the IR, and consequently, the XUV, laser polarization can be rotated to an angle for which no single photon peaks appear on the detector. In order for this technique to work, the PES must be collected in a small solid angle, i.e. without magnetic fields and, possibly, with a small acceptance aperture. TPDDI peaks instead may be expected to have a different angular distribution, so that they may appear in the detector even when the laser polarization is set to exclude the presence of single photon peaks.

- even in this case, the background signal is strong as compared to the expected TPDDI yield. This problem is due to the fact that our detection area is not optimized for this kind of operation: the XUV beam has to pass under, or over, the detection jet before being focused back in front of it by the split mirror, and this produces a large source of background. By focusing the XUV beam with a grazing toroidal mirror before the detection jet, we may expect to reduce the background to almost zero.

While it is easy to try the first point, the second requires radical changes to the currently available set-up. The new set-up, currently under development, shall be equipped with toroidal mirrors, so it will be possible to re-try this experiment with the suggested improvements.

3.4 Measurement of XUV pulse duration

The XUV pulse duration is a crucial parameter in pump-probe experiment. 2^{nd} order Intensity Volume Auto Correlation (2-IVAC) is the technique we currently use for this measurement (see sec. 1.4).
The temporal properties of the one-color generated XUV radiation has been extensively studied in the past [46, 60, 84, 85] through different techniques. During any pump-probe experiment it is obviously important to know the duration of the used pulses. This allows us to distinguish in a pump-probe trace the quantum effects related to the system under investigation from the quantum-optical effects. In this work we characterize the temporal structure of HOH generated by the long trajectories in a 2-color driving field. The temporal characterization of the XUV radiation generated by a 2-color field is motivated by the following reasons. As explained in sec.1.2, the harmonics generated by a 2-color field are expected to be more intense as compared the ones generated by a one-color field. Thus, the larger resulting signal would be much more useful for the applications in an XUV-pump-XUV-probe study. Previous works on 2-color generation mainly focus their studies on the spectral properties. In [14] the XUV pulse duration is estimated as a function of the phase difference between the fields. The experimental characterization of the temporal properties of the XUV pulse is an open field of investigation. In [10] it is reported that, by controlling the relative phase between the two fields, the two-dimensional trajectories can be steered to return, or not, to the core, thus providing a control on the relative strength of the short or long quantum trajectory contribution. In one-color generation, it is known that long trajectories can provide higher energy content to the HOH, but the resulting XUV temporal structure is worse than for the short trajectories. In 2-color generation, this control on the trajectories may provide an improvement in the temporal structure of HOH with the unique contribution by the long trajectories.Within this generation scheme, a temporal characterization of the HOH has never been provided before.

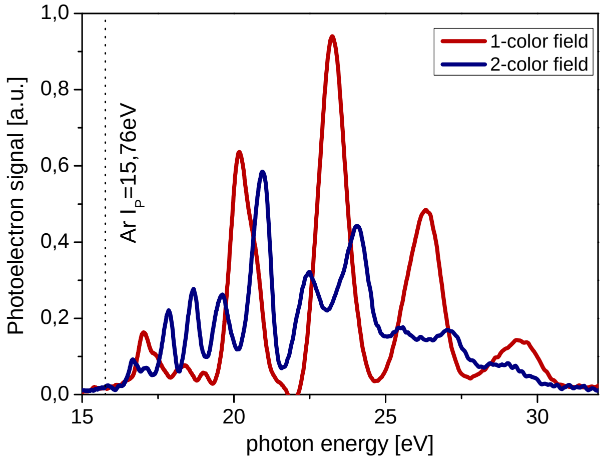

Figure 26: *Ar* photo-electron spectra, converted from electron TOF to photon energy scale. In red, the spectrum from one-color generation; in blue for two color. Only energies above $IP_1(Ar)$ are visible. Spectrum for one-color generation is shown just for the comparison.

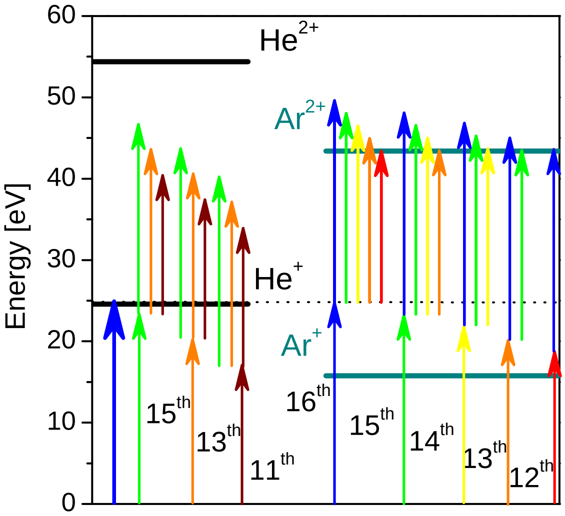

Figure 27: Compared excitation scheme for Ar and He. In case of only odd HOH and Sn filter, He^+ is a suitable non-linear medium. In case both odd and even HOH are produced, even after the Sn filter the 16^{th} harmonic alone can singly ionize He. Ar^{2+} in combination with Sn filter, is, instead, a suitable non-linear medium.

3.4.1 Methodology

The spectrum of the XUV radiation used in this experiment (which contains odd and even harmonics) is shown in fig. 26 (blue line). The red line, which refers to the harmonic spectrum (contains only odd harmonics) in case of using 1-color driving pulse, has been placed in the same figure only for reasons of comparison with the spectrum generated by a 2-color driving pulse.
Since the spectrum contains harmonics up to the 16^{th}, He can not be used as a non-linear detector, because the photon energy of the 16^{th} harmonic is slightly above its $IP_1 = 24.58eV < 16\hbar\omega_L = 24.8eV$. This is shown in the excitation scheme of fig. 27. Thus the TPDDI of Ar has been considered as the ideal excitation scheme (figs. 22, 27) for the temporal characterization of the XUV radiation. Here, is interesting to note that the presence of any 2-photon sequential ionization process which can influence the duration of the measured pulse is entirely absent.

For the generation of odd and even harmonics, the IR beam is focused by a $3m$ lens into Xe gas jet where the harmonic generation is taking place. In order to generate the 2ω field and to control the relative phase between the two colors a BBO crystal and a $400\mu m$ thick CaF_2 plate have been placed at two separate rotating stages $1.4m$ before the Xe gas jet. Taking into account the dependence of the refractive index on extra-ordinary $(n_E(400nm) = 1.56869)$

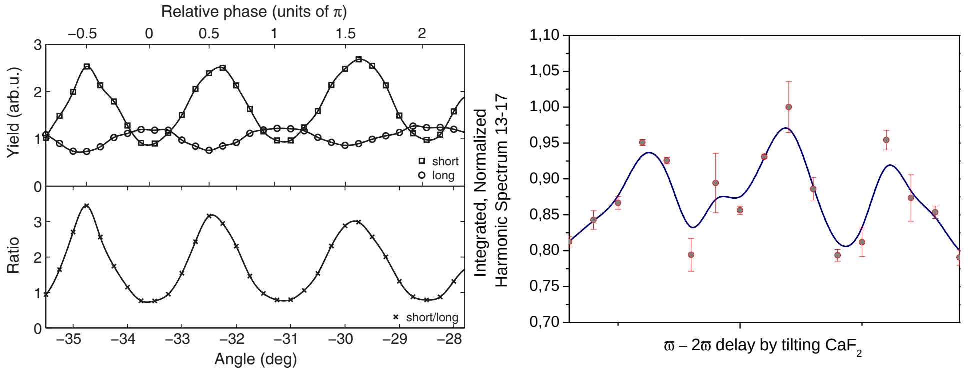

(a) (b)

Figure 28: $\omega - 2\omega$ field delay from the proposed work [10] and in our setup. The graph on the right shows the modulation mainly of the long trajectories (because of the experimental conditions, see fig. 29), so it has to be compared with the modulation for long trajectories in the graph on the left. Despite the different experimental conditions, the observed effect is consistent. (a): Modulation of long (circles) and short (squares) trajectory contribution vs $\omega - 2\omega$ field delay. *[L. Brugnera et al. PRL 2011.]* (b): Equivalent measurement performed in our set-up with the conditions illustrated in fig. 29.

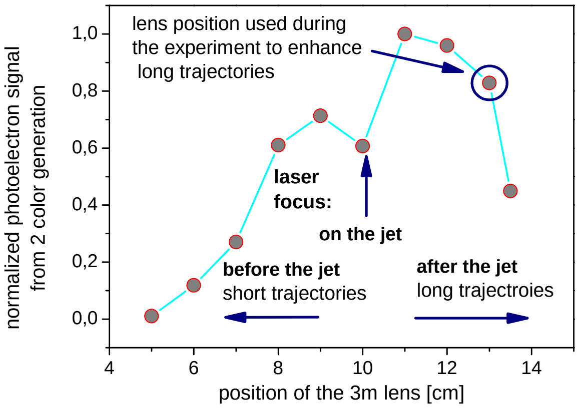

Figure 29: In order to enhance the contributions of long trajectories, we set the laser focus after the production jet. The plot shows the 2-color generated HOH energy as a function of the lens position.

and ordinary axis ($n_O(800nm) = 1.66129$, $n_O(400nm) = 1.69329$) of the crystal (thickness $1mm$) on the rotation angle Θ, given by

$$n_E(\Theta, 2\omega) = \sqrt{n_O^2(2\omega)\cos^2(\Theta) + n_E^2(2\omega)\sin(\Theta)} \tag{61}$$

it can be obtained that, around the angle $\theta = 31°$ where phase matching condition are fulfilled, the $\omega - 2\omega$ delay varies as $d\tau/d\Theta \approx 6fs/deg$. The calcite plate CaF_2, $400\mu m$ thick, introduces a positive dispersion variable between $15.12fs$ at $0°$ and $17.37fs$ at $45°$, thus is suitable for fine tuning of the delay τ. The dependance of the harmonic yield on the relative phase between the two colors in the 2-color driving pulse is shown in fig. 28(b). This dependence is associated with the change of the electron quantum path trajectory and serves for the in-situ manipulation of the emitted XUV spectral phase distribution. Despite the different experimental conditions (loose focusing configuration, different ratio between the medium length and the confocal parameter), this observed dependence is in fair agreement with the one observed in [10] and shown in fig. 28(a). The dependence of the harmonic energy on the position of the focus relative to the gas jet (fig. 29) has been recorded in order to obtain the position where the phase matching conditions are optimum for the long trajectory harmonic generation ($z = +b/2$). This position is marked with the blue circle in fig. 29. As described in sec. 3.1, the divergence of the harmonics emitted by long trajectories is larger compared to the short. Similar is the situation in case that a 2-color driving

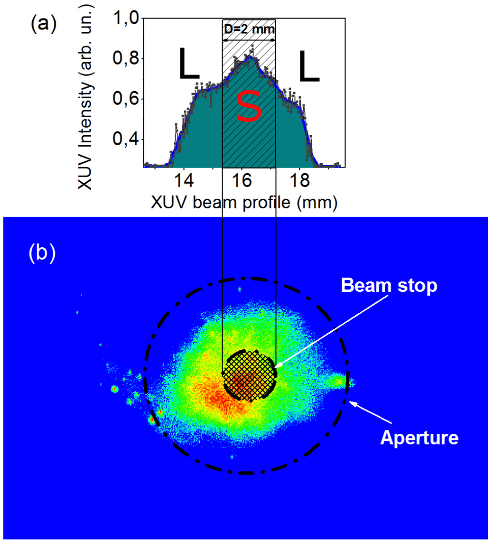

Figure 30: The mask used in the experiment to cut the contribution of short trajectories. In the center of a $5mm\varnothing$ pin hole we put a $2mm\varnothing$ disk.We represent this masks on the XUV beam profile as acquired with the knife edge technique (a) and with a phosphor screen (b).

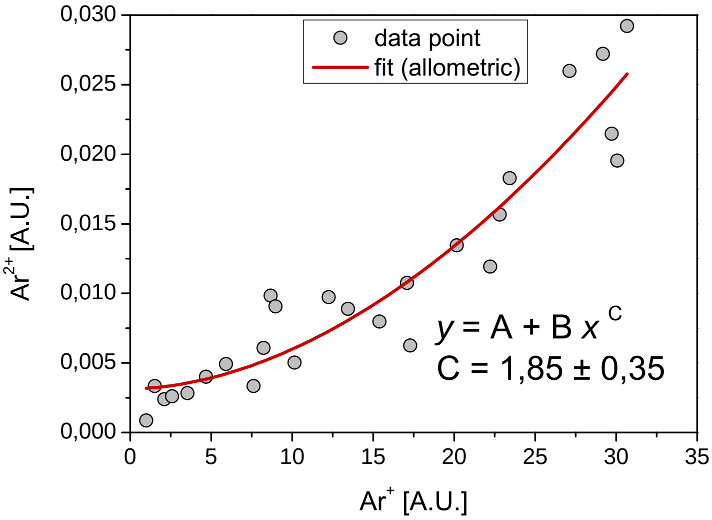

Figure 31: Power dependence for Ar^{2+} vs Ar^{+} with $150nm$ thick Sn filter in 2-color generation scheme. The slope of 1.85 ± 0.35 indicates that Ar^{2+} is produced in a non-linear 2-photon process, in agreement with the excitation scheme of fig. 27. It must be remarked that 17^{th} harmonic is cut by the filter, while the 16^{th} is not. This prevents the use of He^{+} as non-linear medium.

pulse is used for the harmonic generation. This is clearly shown in the XUV beam profile measurement of fig. 30. Thus, In order to select only the long trajectories from the harmonic beam, we set an annular shaper ($2mm$ internal diameter, $5mm$ the external one) in the XUV beam, in order to cut the contribution from short trajectories. Thus, by using the long trajectory HOH $11^{th} - 16^{th}$ (Sn filter has been used) and the TPDDI scheme of Ar, the non-linearity of the process has been clarified (fig. 31) and the 2-IVAC trace has been recorded (fig. 32(a)). In this figure, the beating of the train of pulses is clearly visible: consecutive pulses are produced with a spacing of one fundamental optical cycle, as expected (being the spectral spacing 1ω, the HOHG must take place once per fundamental optical cycle) and as confirmed also by the FFT of fig. 32(b). In the case of one-color generation, such spacing is half a fundamental optical cycle, which in the frequency domain would appear as a frequency of $2/T_{IR}$. The pulse duration varies from small to larger delays; the average value is $\tau_{XUV} = 1.8 \pm 0.3fs$. Another feature of fig. 32 is the modulation of the contrast, which is enhanced where peaks are sharper: this is highlighted in the time domain by the red and blue lines, while it appears in the FFT as the structure of the main peak. It seems that the relative phase between the harmonics generated by the long trajectories changes during the interaction of the medium with two two-color field, but this is a subject under investigation.

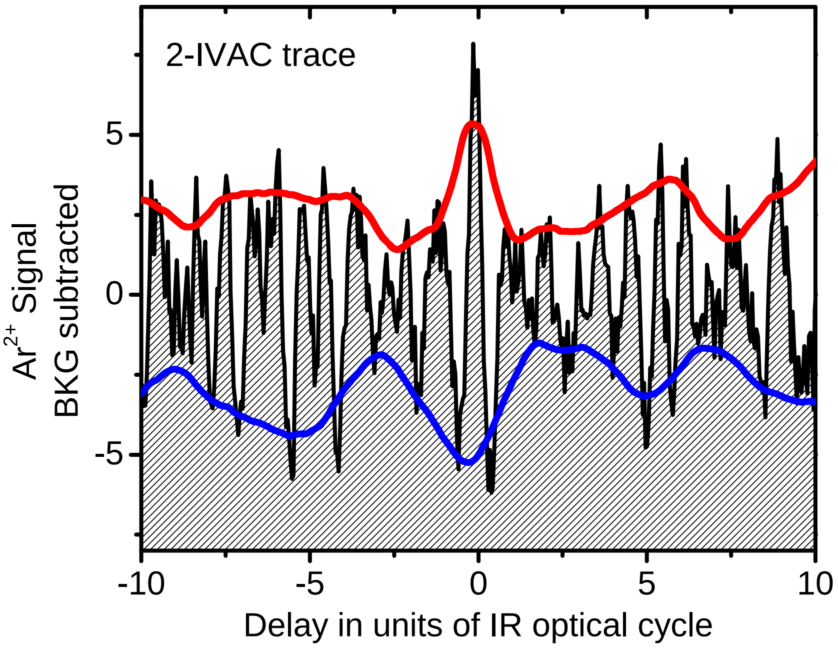

(a)

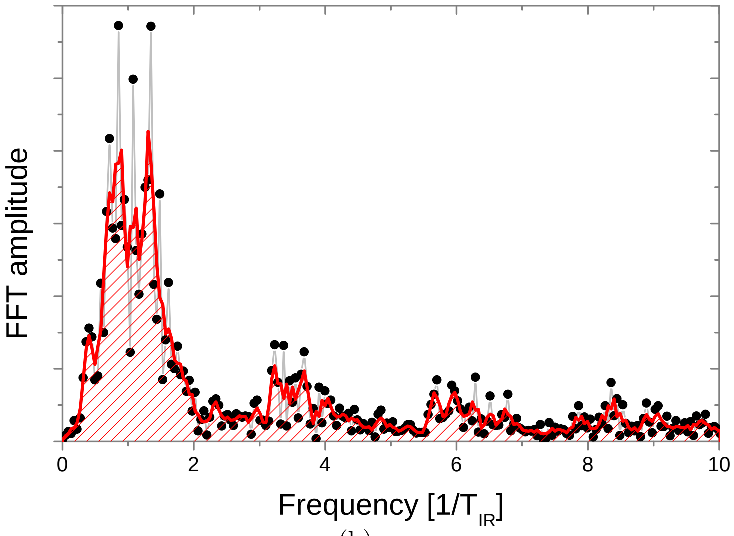

(b)

Figure 32: Temporal structure of long trajectories by 2-color generated HOH and its FFT. 150nm thick Sn filter is used to cut both generating fields (800 and 400nm wavelength) and the 17^{th} harmonic. Due to an annular shaped mask before the metal filter, only contributions from long trajectories appear in this trace. (a): Temporal structure revealed by the 2-IVAC measurement using Ar^{2+} as non-linear medium. Red and blue lines show the modulation of the maximum and of the minimum, respectively. (b): The FFT trace shows that the main frequency is $1/T_{IR}$, which means that pulses are generated once per optical cycle. The large width of this peak, which spans from $\approx 0.5/T_{IR}$ to $\approx 1.5/T_{IR}$, and its structure are related to the modulation in the contrast of the peaks, as shown by the red and blue lines in (a).

4 XUV pump - XUV probe experiment in diatomic molecules, part I: H_2

4.1 Ultrafast dynamics in the molecule of H_2

Through frequency up-conversion of polarization shaped fs laser pulses, non-linearly interacting with Xenon atoms, energetic, broadband, coherent extreme-ultraviolet (XUV) continuum radiation is generated. Exploiting the thus formed short duration XUV pulses, all the optically allowed excited states of H_2 are coherently populated. Nuclear and electronic $1fs$ scale dynamics are subsequently investigated by means of XUV pump - XUV probe measurements, which are compared to the results of *ab initio* calculations. The revealed dynamics reflects the intrinsic molecular behavior as the XUV probe pulse hardly distorts the molecular potential. Coherent light pulses of few to hundreds of femtoseconds (fs) duration have prolifically served the field of ultrafast phenomena. While fs pulses address mainly dynamics of nuclear motion in molecules or lattice in the gas, liquid or condensed matter phase, the advent of attosecond pulses has in recent years provided direct experimental access to ultrafast electron dynamics. However, there are processes involving nuclear motion in molecules and in particular coupled electronic and nuclear motion that occur in the few fs or even sub$-fs$ time scale. Electronic excitations in molecules are commonly in the VUV/XUV spectral region. Until recently most of the XUV sources were lacking either sufficient pulse energy (HOHG sources) or ultrashort pulse duration Free Electron Laser (FEL), thus preventing access to XUV-pump-XUV-probe measurements in the 1 fs or asec temporal scale. Experimental efforts in this time scale have been restricted to XUV-IR pump-probe schemes [34, 37, 41, 44, 73, 94], or in-situ electron-ion collision methods [59]. Systematic developments in high pulse energy HOHG [36, 58, 62, 66, 83] and XUV super-continua [27, 53, 74, 80, 88] paved the way to time delay spectroscopic studies [79] and XUV-pump-XUV-probe experiments [75,87] that have lately demonstrated their first proof of principle application in the measurement of induced, ultrafast evolving atomic coherences in an atomic continuum [75, 79, 90]. Such measurements are free of interventions from unwanted channels, opened through quasi-resonant multi-IR-photon transitions. The present work, motivated by a recent theoretical study [87], demonstrates the first $1fs$ scale XUV-pump-XUV-probe study of ultrafast dynamics in H_2. It further aims at illustrating a fundamental difference between atomic and molecular dynamics. In molecules the nuclear motion modulates the signal of the beating between coherently excited electronic states as the pumped target evolves field-free, because the nuclear-wave-packet associated with each electronic state is moving and spreading, therefore modifying the relative contribution of the electronic states involved. In this work, a broadband extreme-ultraviolet (XUV) pulse is used to coherently excite all the optically allowed excited states of H_2. Nuclear and electronic dynamics are subsequently analyzed. These reflect the intrinsic molecular behavior as the XUV probe pulse hardly distorts the molecular potential.

4.2 Goal of the experiment

The scheme under investigation is shown in fig. 33. The inset shows the spectrum of the continuum radiation used. Absorption of one photon excites coherently all optically allowed electronic states of H_2, in each of which a superposition of those vibrational levels that are within the Franck-Condon region are populated. A fraction of the bandwidth also ionizes the molecule leaving it in the bound part of the H_2^+ ionic ground state. The dynamics of the excited electronic and vibrational wave-packets are probed through absorption of a photon from the second temporally delayed XUV pulse. Absorption of the second photon brings the molecule above its ionization limit at excess energies that allow fragmentation of the ion. Upon evolution of the molecular vibration, the molecule stretches to internuclear distances, from which the state is accessible through the absorption of the second photon. Fragmentation through this repulsive state produces protons with non-zero kinetic energies that depend on the internuclear distance at the moment of the absorption of the second photon, as visible in fig. 34. Consequently, the delay is a parameter that can switch this channel on and off and control the kinetic energy of the produced protons. Although there is some probability that two photons are also absorbed either solely from the first or the second pulse, for the pulses used here the state is dominantly populated through one-photon absorption from the first pulse followed by one-photon absorption from the second one, i.e. only through the pump-probe sequence.

4.3 Set-up

The experimental set up used has been described in a previous work [24,33, 74,79,84,88] and in sec. 2. A $10Hz$ repetition rate Ti:Sapphire laser system delivering pulses of energy $E_L < 170mJ/pulse$, $33fs$ duration and a carrier wavelength at $800nm$, is used for the XUV generation. A laser beam of $\approx 2.8cm$ outer diameter and energy of $\approx 100mJ/pulse$ was passing through an IPG device [74,88]. The ellipticity modulated laser field, focused by a $3m$ focal length lens, interacted with the atoms of a Xenon gas jet generating

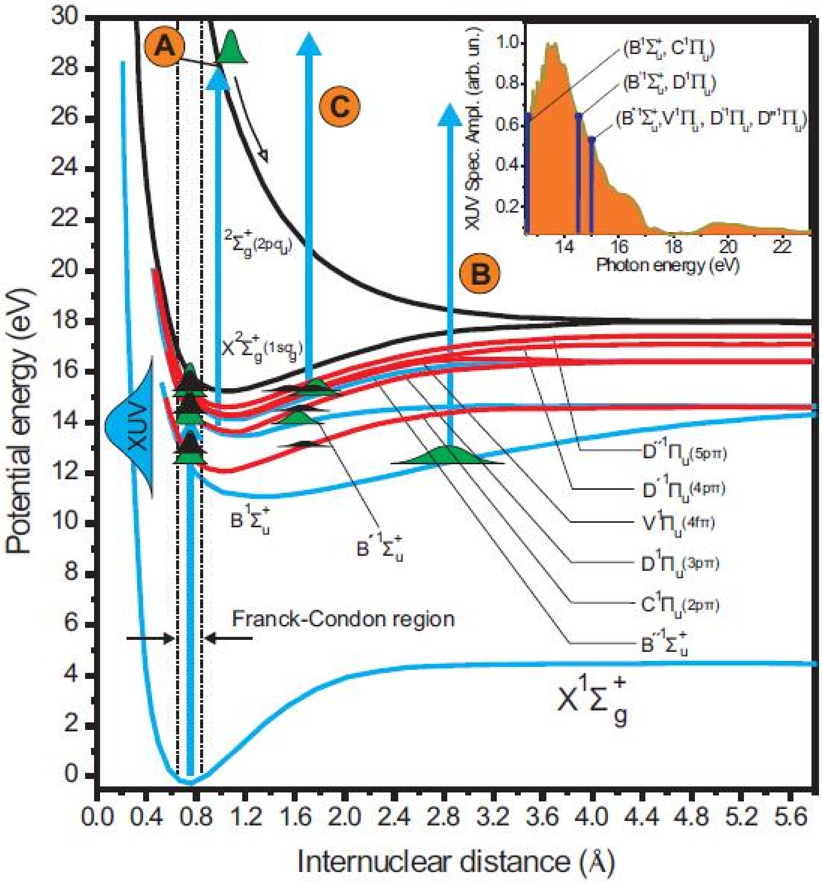

Figure 33: The inset shows the XUV spectrum used in the experiment. This spectrum is selected, using an Indium transmission filter, from the radiation produced through non-linear frequency up conversion applying the IPG to the HOHG process. Single photon absorption excites all dipole allowed electronic and vibrational states of H_2 within the Franck-Condon region. The evolution of the excited electronic and vibrational wavepackets is traced by a delayed replica of the XUV pulse, detecting the yield of H^+ produced through fragmentation of H_2^+. The vertical lines in the spectrum of the inset indicate the states that are resonant with the specific interval of the spectrum. (A) refers to the opening of the ionization/dissociation channel through the $^2\Sigma_g^+$ $(2p\sigma_u)$ repulsive potential. (B) and (C) refer to the vibrational dynamics in the $B^1\Sigma_u^+$ (B) and $C^1\Pi_u/B'^1\Sigma_u^+/D^1\Pi_u$ (C) intermediate electronic states of the neutral molecule. For the assignment see also fig. 39(a).

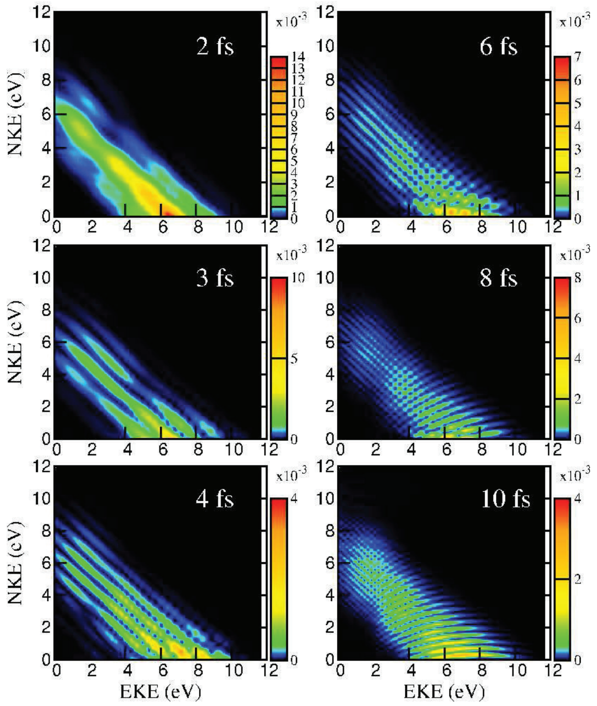

Figure 34: Nuclei Kinetic Energy vs Electron Kinetic Energy for different delays. $1s\sigma_g$ contributions, photon energy $12eV$. Note the different color scale and the high NKE for $\tau = 2fs$.

a coherent XUV continuum. The laser focus was placed before the jet in order to select mainly the short electron trajectory. The XUV is separated from the IR radiation through reflection on a Si plate (fig.14) placed at the Brewster angle for $800nm$. The XUV spectral region used in the experiment was selected by a $150nm$ thick Indium filter that was also filtering out the residual IR radiation. The emitted XUV spectrum, shown in fig. 35, has been recorded by measuring the energy resolved PES of the single photon ionization of Xe. In the interaction/measurement area the XUV pulse impinges at normal incidence a spherical split mirror of $10cm$ radius of curvature. The mirror focuses the XUV beam into a pulsed H_2 jet, synchronized with the arrival of the XUV pulses. The XUV waist diameter is measured to be $2 \pm 1\mu m$ and the estimated XUV intensity at the focus lies between 10^{13} and $10^{14}W/cm^2$. Charged interaction products, i.e. H_2^+ ions and H^+ fragments, are detected through a time-of-flight mass spectrometer as a function of the delay introduced by the split mirror translating the one of its two parts using a piezoelectric linear translator. The temporal resolution of the device

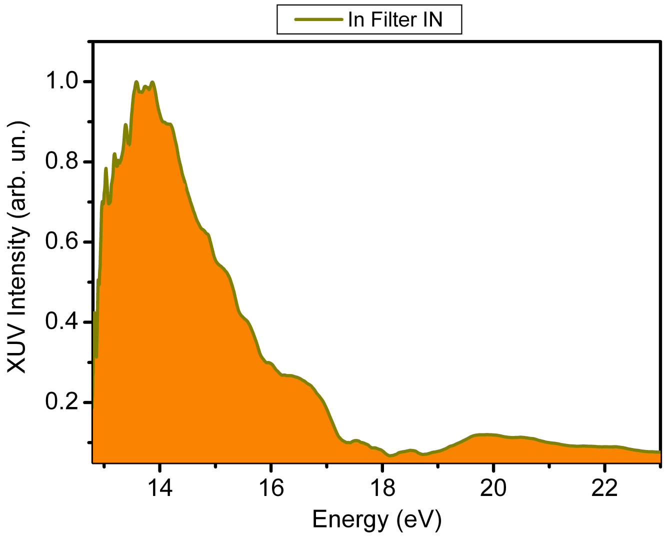

Figure 35: Xe photoelectron spectrum obtained from the XUV continuum used in the pump-probe experiment. $150nm$ In filter is inserted. This spectrum supports a FTL limited pulse of $600as$.

is $150asec$. The overall temporal resolution is determined by the XUV pulse duration ($\tau_{XUV} > 600asec$, FTL value), which is not measured because of the not stabilized CEP of the driving field, which causes an alternating XUV waveform from single-pulse to double-pulse structure [55, 75, 90]. While specific proton kinetic energies cannot be resolved in the mass spectrum, protons with nearly zero kinetic energy can be effectively distinguished from those with non-zero kinetic energy in the mass peak structure. Nearly zero kinetic energy fragments contribute mainly to the center of the ion mass peak; while non-zero kinetic energy fragments are present mainly at the tails of the peak.

4.4 Power dependence

Observable two-XUV-photon absorption is verified through intensity dependence measurements of the ion yields shown in fig. 36. In log-log scale the slope of H_2^+ yield is 1 as expected for a linear process, while the slope of the proton yield is close to 2 (1.7), indicative of a two-photon process. The used XUV bandwidth is rather advantageous, as it is broad enough to efficiently launch a nuclear wave packet that favors sequential two-photon absorption to the ${}^2\Sigma_g^+(2p\sigma_u)$ continuum and decreases the relative importance of one- and two-photon absorption to the $X^2\Sigma_g^+(1s\sigma_g)$ continuum. This plot has been produced using HOHG, not the coherent continuum. This choice is

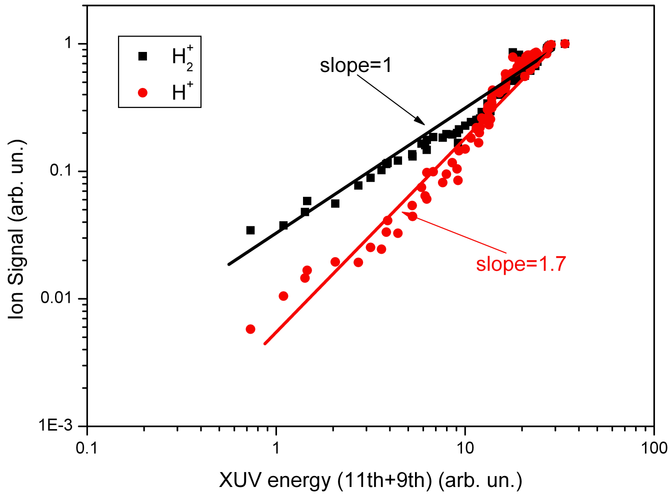

Figure 36: log log plot of H^+ and H_2^+ as a function of the XUV energy with $150nm$ In filter inserted. The graph shows that H_2^+ is produced in a 1 photon process while H^+ in a 2 photon process.

motivated by the need for long term stability and a broad range of XUV energies and ion yield. Also, the theoretical cross section for dissociative and non-dissociative ionization in H_2 as a function of photon energy we referred to (see fig. 37), have been calculated for pulse duration of $10fs$ or more, which is the case for the train of pulses supported by high harmonic spectrum. The plot has been calculated for XUV intensities of $10^{10}W/cm^2$ and $10^{12}W/cm^2$. For the two considered intensities the general behavior is the same: in the spectral region of 1-photon absorption, the non-dissociative ionization is totally dominant over the dissociative one, while in the spectral region associated with the 2-photon process there is an energy window in which the dissociative is much stronger than the non-dissociative one. Such window is in the spectral region of our XUV pulse (fig.35). Thus the theory indicates that the production of H_2^+ is due only to the 1-photon absorption process, while for H^+ only the 2-photon process is involved.

XUV energy is measured with spectral resolution using the TOF in photoelectron energy spectrometer configuration: after the $150nm$ thick In filter the XUV radiation passes unfocused in front of a Xenon gas jet. A small repulsive potential of $-2.09V$ is given in the jet to increase slightly the collection of electrons close to zero kinetic energy. H^+ and H_2^+ yield is measured by focusing, with only one part of the split mirror, the XUV beam in front of the same gas jet filled with H_2. Ions are collected at the TOF in ion mass

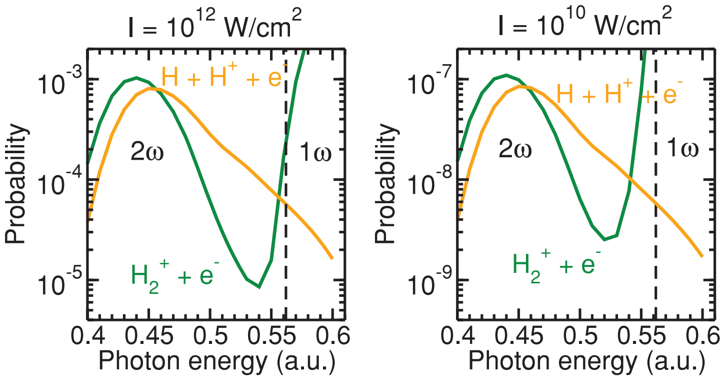

Figure 37: Ionization probabilities versus photon energy for a pulse duration of $T = 10fs$. Left: laser intensity $I = 10^{12} W/cm^2$; right: $I = 10^{10} W/cm^2$. Orange curve: dissociation ionization; green curve: nondissociative ionization. Vertical lines indicates H_2 ionization potential. *[Pérez-Torres et al. J.Phys.B. 2010]*

spectrometer configuration, which requires the application of an extraction potential of $+5kV$.

In order to scan over different energy values for the high harmonics, we change the intensity of the IR beam. We set the IR beam to have annular shape, with fixed internal diameter of $12.5mm$, defined by the dimension of the beamstop mounted in a super-Gaussian beam profiler, and the external diameter of $22mm$, adjustable with an iris. The absolute IR energy is measured with a powermeter at the beginning and at the end of each of the two scans, while for each data point the relative IR energy is measured from a parasitic reflection with the same photodiode that is normally used for triggering the acquisitions. The initial and maximum pulse energy for the IR annular beam is $11.0 \pm 0.3mJ$ while measuring the XUV energy and $11.3 \pm 0.3mJ$ while measuring the ion yield. Both for ions and harmonics, each data point is the average of 140 laser shots. 68 data points have been collected for the harmonic energy and 65 for the ion yield, until the point of zero signal is rseached. With data interpolation $E_{XUV}(IR)$ and $Y_{ion}(IR)$ can be combined to obtain $Y_{ion}(E_{XUV})$ as shown in fig. 36.

4.5 Theoretical methods

The employed method is widely described in [33,65]. Only the relevant stages and the details of the implementation are given in the following. In brief, the time-dependent Schrdinger equation is numerically solved:

$$i\frac{\partial}{\partial t}\Phi(\vec{r},R,t) = \left[H\left(\vec{r},R\right) + V\left(\vec{r},R,t\right)\right]\Phi\left(\vec{r},R,t\right) \qquad (62)$$

where $\vec{r}$ stands for the electronic coordinates, H is the Hamiltonian of the isolated molecule, and V is the laser-molecule interaction. The time-dependent function is written in the basis of the vibronic eigenstates of H. The initial wave function, $\Phi\left(\vec{r}, R, t=0\right)$, is that of the ground state of the neutral $X^1\Sigma_g^+$. The time-dependent potential term V is written in the dipole approximation as the product of the dipole operator and the potential vector, $\vec{\mu}\cdot\vec{A}(t)$. The field is defined with two identical pulses with a given delay, τ. The vector potential can be then written as:

$$\vec{A}(t) = A_0\left[F(t) + F(t-\tau)\right]\vec{e_z} \tag{63}$$

where the direction of the field $\vec{e_z}$, is chosen parallel to the molecular axis, which implies only transitions ${}^1\Sigma_g^+ \rightarrow^1 \Sigma_u^+ \rightarrow^1 \Sigma_g^+$ are included in the calculation. The pulse is defined with sin-squared shape:

$$F(t') = \begin{cases} \sin^2\left(\frac{\pi t'}{T}\right)\cos(\omega t' + \phi) & \text{if } t' \in [0, T], \\ 0 & \text{elsewhere.} \end{cases} \tag{64}$$

The pulses are defined with a length $T = 2fs$, which approximately corresponds to an experimental FWHM duration of $800as$, and a central photon energy $\hbar\omega = 12.2eV$, which is in resonance with the transition from the ground state at the equilibrium distance to the first excited state of H_2, $B^1\Sigma_u^+$. The large energy bandwidth ($\approx 3eV$) of such a short pulse will populate bands of vibrational states associated to several electronic excited states. For simplicity, phase ϕ is equal to zero, which is not relevant for the present analysis with these photon energy and duration (a $2fs$ pulse of $12.2eV$ includes up to ~ 6 cycles).

In fig. 38 is shown the calculated H^+ yield as a function of pump-probe delay and H^+ KER. The theoretical plot of fig. 39(b) is consequently obtained by integrating the data of fig. 38:

$$Y_{H^+}^{E_k \geq 0.4}(\tau) = \int_{E_k = 0.4eV}^{+\inf} Y_{H^+}(\tau, E_k)dE_k \tag{65}$$

The selection rules for allowed one-photon electric dipole-allowed transitions which apply to light homonuclear molecules are:

$$\begin{gathered} \Delta\Lambda = 0, \pm 1, \quad \Delta S = 0, \quad \Delta\Omega = 0, \quad g \leftrightarrow u \\ \Sigma^+ \leftrightarrow \Sigma^+, \Sigma^- \leftrightarrow \Sigma^-, \Pi \leftrightarrow \Sigma^+, \Pi \leftrightarrow \Sigma^- \end{gathered} \tag{66}$$

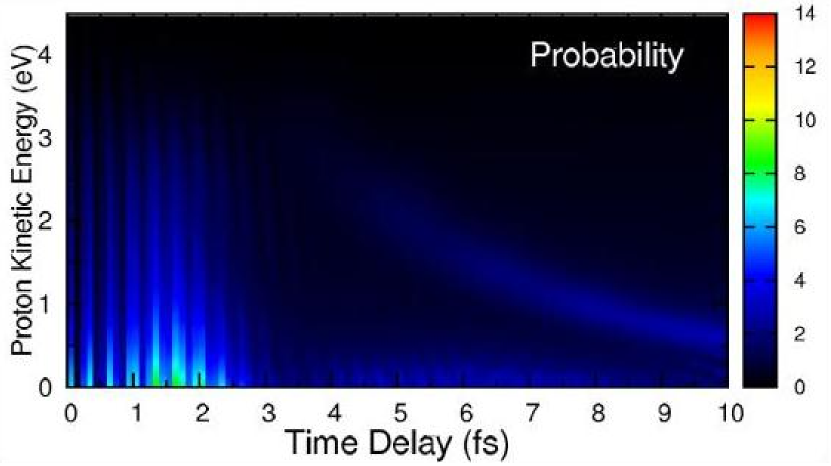

Figure 38: Calculated H^+ production probability as a function of the pump-probe delay and the proton kinetic energy release. The pulse is shaped as $\sin^2$, has length $T = 2fs$, which approximately corresponds to an experimental FWHM duration of $800as$, central photon energy $h\nu = 12.2eV$ and $h\Delta\nu \approx 3eV$.

4.6 Results

Fig. 39(a) depicts the total proton yield as a function of the delay between the two XUV pulses, while fig. 39(b) shows the yield of the protons with non-zero kinetic energy. It should be noted that protons with near zero initial velocity component along the TOF axis (i.e. those contributing to the center of the mass peak, to which we refer as zero kinetic energy protons) are not only those with zero initial kinetic energy (irrespective of the orientation of the molecules), but also most protons ejected perpendicularly with respect to the TOF. Thus protons with non-zero kinetic energy are mainly those ejected from molecules oriented perpendicularly to the polarization direction.

A non-typical but common feature in both figures is the local minimum observed at zero delay, at which the optical interference is expected to lead to a maximum yield in a second order process. This minimum and the subsequent build up of the proton yield during the first fs are attributed to the following dynamics. At zero delay, the dissociation channel through the ${}^2\Sigma_g^+(2p\sigma_u)$ state is practically closed, while after $\approx 1fs$ the excited molecule stretches such that absorption of the second photon from the intermediate state reaches the repulsive state ${}^2\Sigma_g^+(2p\sigma_u)$, leading to an enhancement of the proton yield. At larger delays the yield decreases due to the wave-packet delocalization.

Beyond their common feature around the zero delay, fig. 39(a) and fig. 39(b) preserve a significant difference, which is the signal ratio between near-zero and longer delay times. In the trace of fig. 39(a) the signal around zero delay

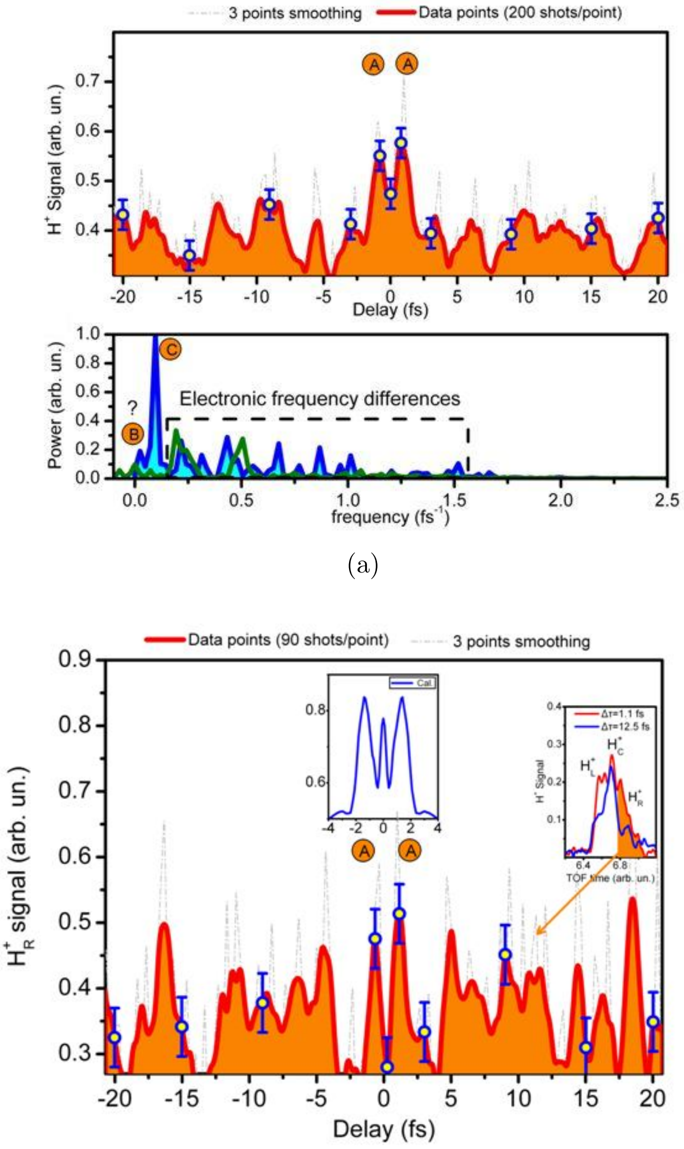

(a)

(b)

Figure 39: Traces for time-delay scan. (a): Measured temporal trace of the total proton yield and its FFT (blue), together with the FFT of the trace in fig. (b) (green). The observed minimum at zero delay and the succeeding build up of the proton yield during the first $1fs$ of delay is attibuted to the dynamics of the opening of the dissociation channel through the ${}^2\Sigma_g^+(2p\sigma_u)$ repulsive potential. A, B, C as in fig. 33. (b): Measured temporal trace of the yield of non-zero kinetic energy protons. The blue curve on top is from theoretical calculations, in which only intermediate states of Σ simmetries have been considered. The inset of the right depicts two ion mass peaks measured at 1.1 and $12.5fs$ delays. To the H_R^+ edge contribute non-zero kinetic energy protons released towards the entrance of the TOF spectrometer. To the H_L^+ edge contribute non-zero kinetic energy proton released towards the repeller of the TOF spectrometer. To the central H_C^+ part of the peak contribute protons produced with zero velocity component parallel to the TOF axis.

is significantly stronger compared to that at longer delay times, a feature that is missing in the trace of fig. 39(b). The signal in fig. 39(a) results from the convolution of the pump-probe channel and the direct 2-photon absorption channel. Thus, the increased yield in fig. 39(a) results from the convolution of the 2-IVAC maximum [84] with the dynamic effect of the dissociation channel opening. The non-zero kinetic energy protons of fig. 39(b) start being produced at non zero delays, for which only the tails of the two pulses are overlapping, and thus the direct 2-photon absorption is significantly reduced. The blue curve of fig. 39(b) has been obtained from the theoretical calculations. In these calculations, the contribution from protons with $KER < 0.4eV$ has been removed. The narrow spike at zero delay is the 2^{nd} order autocorrelation (AC) of the pulse used in the calculations. For a $720asec$ long pulse its FWHM is $1.02fs$. As its width is smaller than the separation of the two side maximum, it is observable between them. The theoretical data in the spike region have been corrected for the reduced peak to background ratio of the 2-IVAC, contributing to the measured trace, as compared to that of a conventional 2^{nd} order AC produced by the calculation. This spike is not observable in the measured trace for the following reasons. Since the laser system has a not stabilized CEP, the emitted XUV spectra fluctuate shot-to-shot between continuum and quasi-discrete spectra with variable harmonic peak positions [90]. Equivalently the emitted XUV waveforms fluctuate from shot to shot between isolated pulses and double peaked distributions with fluctuating relative peak heights. The corresponding shot-to-shot energy shift of the spectral distributions amounts up to $\pm 1.5eV$. Moreover the harmonic generation process produces non Fourier transform limited pulses (FTL). For these reasons the measured 2^{nd} order AC peak is broader than the distance between the two side maximum and thus appears as enhanced background. The traces of fig. 39(a) and fig. 39(b) at longer delays depict similar features of multi-frequency beating. Unlike in many existing studies, this beating is the result of combined electronic and vibrational wave-packet dynamics. The concurrent coherent excitation of electronic and vibrational states in principle allows the simultaneous investigation of electronic and nuclear motion. The vibrational frequencies and energy differences of different states are shown in the theoretical curves of fig. 40. The Fourier transform (FT) of the traces on fig. 39(a) and fig. 39(b) is shown in the lower panel (blue and green curve respectively) of fig. 39(a). In the FT of fig. 39(a), the pronounced peak at $0.09fs^{-1}$ corresponds to half the vibrational period of the $C^1\Pi_u$, $B'^1\Sigma_u^+$, $D^1\Pi_u$ (unresolved) states at the excitation energy interval of the experiment [93], the $C^1\Pi_u$ being the main contributor. This is the only frequency peak that can be safely assigned in the present work. The small peak at $0.04fs^{-1}$ is compatible with half

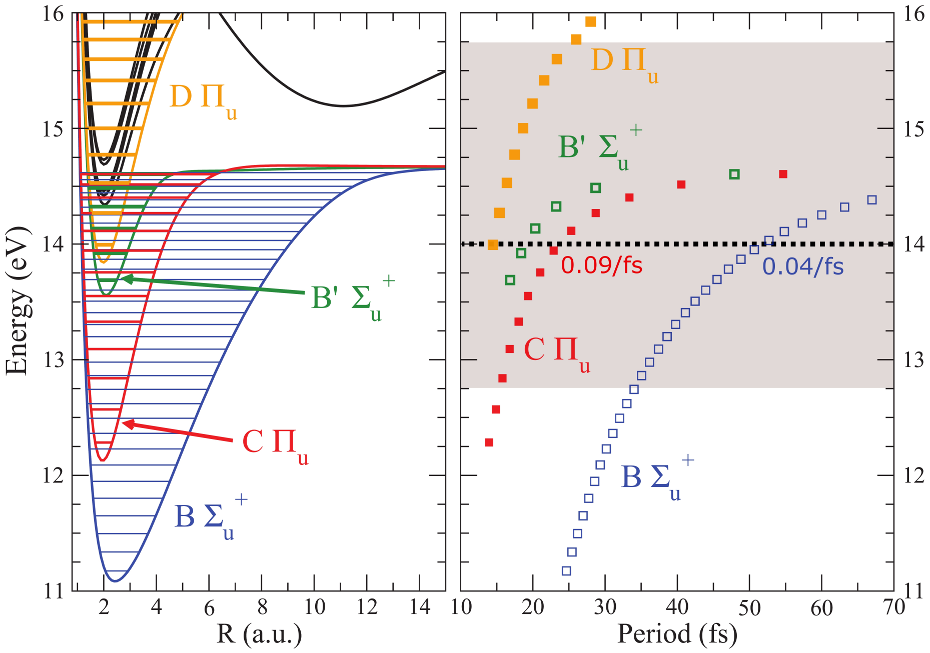

Figure 40: Calculated H_2^+ vibrational energy levels and related oscillation periods. XUV bandwidth is represented as shaded area on the right.

the vibrational period of the $B^1\Sigma_u^+$ state, but due to the maximum delay of the measured trace ($\pm 22fs$) such a measurement is marginal. In the FT of fig. 39(b) (green curve) the pronounced peak C disappears. This is compatible with the fact that states of Π_u symmetry (in particular the $C^1\Pi_u$ state) do not contribute to the non-zero KE proton yield (the $\Sigma_g \rightarrow \Pi_u$ transition is forbidden for molecules parallel to the polarization direction). The rest of the peak structure in the FT spectra could be attributed to beating frequencies between electronic states. The signal level and spectral resolution of the experiment does not allow though an unambiguous assignment of these peaks.

4.7 Conclusions

In a nut shell, utilizing an intense coherent XUV super-continuum radiation, simultaneously electronic and nuclear dynamics in molecular hydrogen, evolving at the $1fs$ temporal scale, have been addressed by means of an XUV pump - XUV probe experiment. The present work paves the way to studies of dynamics beyond the Born-Oppenheimer approximation, addressing the dependence of the electronic dynamics on the variation of the internuclear distance during the vibrational motion. This will be achieved at increased temporal resolution, through reduced pulse duration, while recording of long temporal traces will substantially improve resolution in the frequency domain.

5 XUV pump - XUV probe experiment in diatomic molecules, part II: O_2

5.1 Dynamics in the photo-dissociation of O_2

5.1.1 Theory and purpose

The UV absorption by O_2 in the UV region in the energy range $7.0eV - 9.8eV$, which is called the Schumann-Runge continuum, is of basic interest for environmental issues, as O_2 and O_3 are responsible for most of the UV absorption within the Earth atmosphere.

Photons from the 5^{th} harmonic, $\hbar\omega = 7.75eV$, are in such energy range: their absorption mainly excites O_2 from the ground state to the $B^3\Sigma_u^-$ bound state, while the excitation of other continuum states has much smaller probabilities. When the excitation energy is larger than the dissociation energy $(7.08eV)$ of the $B^3\Sigma_u^-$ state, the direct dissociation into $O\,(^3P)$ and $O\,(^1D)$ is the dominant process. This process was studied in previous works by *Farmanara, 1999* [23] and by *Conde, 2009* [64], but, because of the inconsistencies between their results, the topic of investigation is still open.

In fig. 41 the energy levels of the O_2 molecule are shown, together with the possible excitation schemes. Excitation by 5^{th} harmonic has been mentioned before. The absorption of a photon from the 7^{th} harmonic, $\hbar\omega = 10.85eV$ may excite the $^+\Delta_u$ neutral state, which has a very shallow energy minimum and leads to the dissociation into neutral atoms. Other dissociative levels may be excited, and they can lead to neutral dissociation as well.

The absorption from the ground state of a photon from 9^{th} harmonic, $\hbar\omega = 13.95eV$, leads to the non-dissociative ionization of the molecule in the $X^2\Pi_u$ state. From the neutral excited states, the system can evolve in different ways. We consider the following scenarios:

1. the excited molecule evolves, without absorbing any other further photon, and dissociates as $O_2 + h\nu_5 \rightarrow O_2\,(B^3\Sigma_u) \rightarrow O\,(^3P) + O\,(^1D)$. The effect for 7^{th} harmonic is similar but involves different levels.

2. the successive absorption of a second photon from the 5^{th} harmonic may, depending upon the delay, lead to the photo-ionization of the molecule. In this case $O_2 + h\nu_5 \rightarrow O_2\,(B^3\Sigma_u)$, then $O_2\,(B^3\Sigma_u) + h\nu_5 \rightarrow O_2^+$

3. the successive absorption of a second photon from 9^{th} harmonics may, depending upon the initial state and the delay, lead to the excitation of ionized bound or dissociative states. In this case $O_2 + h\nu_5 \rightarrow O_2\,(B^3\Sigma_u)$,

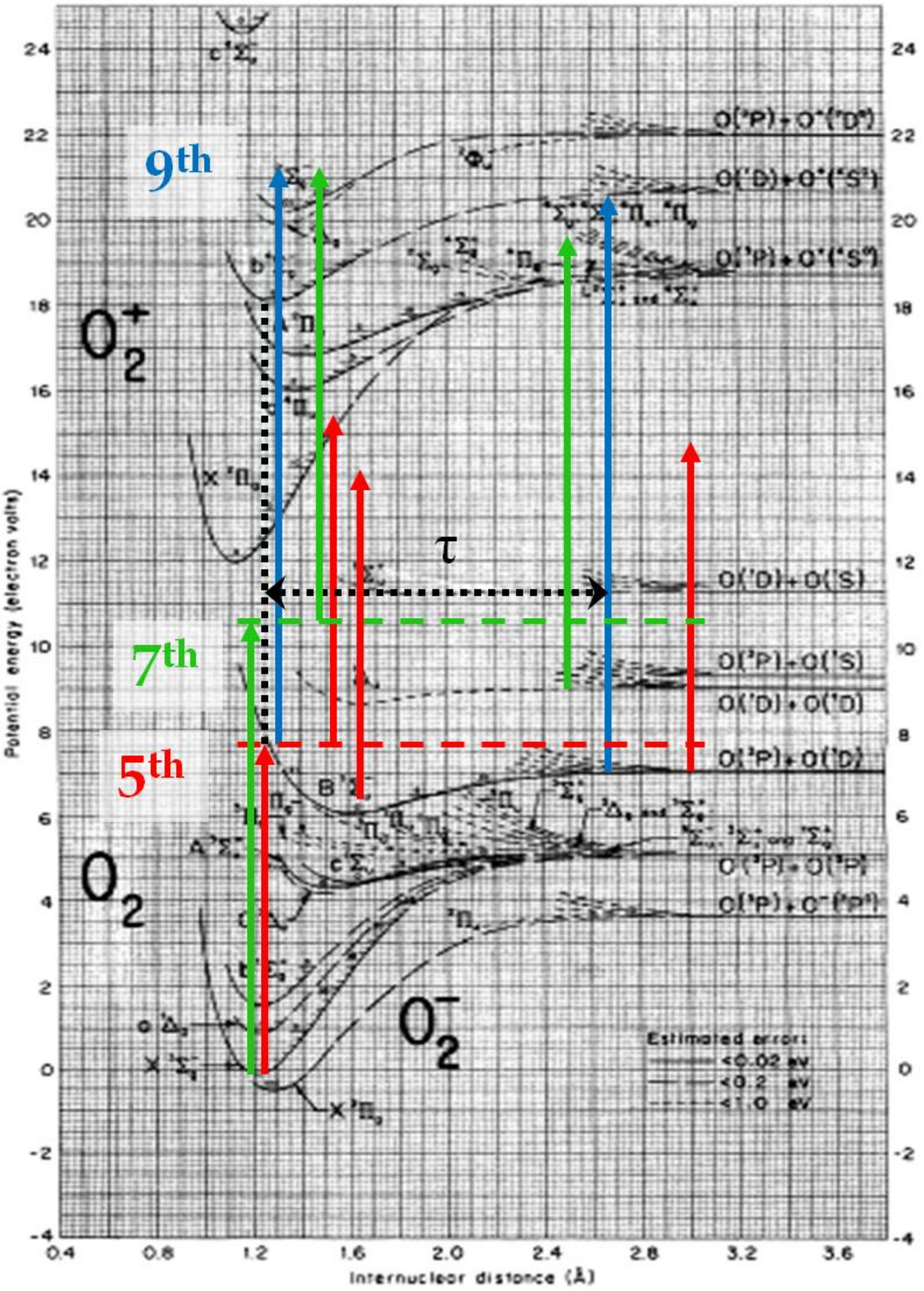

Figure 41: Energy levels and excitation scheme for O_2 molecule.

then $O_2\,(B^3\Sigma_u) + h\nu_9 \rightarrow O_2^\star \rightarrow O + O^+$. The same effect can be produced with $7^{th} + 7^{th}$ absorption. In this case $O_2 + h\nu_7 \rightarrow O_2\,(^+\Delta_u)$, then $O_2\,(^+\Delta_u) + h\nu_7 \rightarrow O_2^\star \rightarrow O + O^+$.

These excitation schemes can be experimentally implemented in pump probe experiments with the following configurations:

- a symmetric one, with 5^{th} harmonic pump and 5^{th} harmonic probe, using a gas mixture of Kr and O_2 and monitoring the delay dependent yield of O_2^+ and Kr^+. A MgF_2 glass works as a low pass filter, cutting the photon energies above the 7^{th} harmonic, thus preventing one photon ionization. It also provides large temporal dispersion between the 3^{rd},the 5^{th} and the 7^{th} harmonic, so that at the mirror zero delay only one color two photon absorption has to be considered. Kr is necessary to measure the duration of the XUV pulse through AC trace.We expect to find a broader trace for O_2^+, as, apart the two photon direct ionization, also the sequential process through neutral excited states is allowed. The resulting trace should show the convolution between the AC trace and the time interval until which the sequential process will close, depending on the internuclear distance and the decay of the intermediate state.

- a similar configuration is used for 7^{th} harmonic pump and 7^{th} harmonic probe. In this case also O^+ shall be monitored, as $7^{th} + 7^{th}$ absorption can provide enough energy to lead, depending on the pump-probe delay, to the dissociative ionization of O_2. This experiment should allow us to measure the time of the opening of the ionized dissociative channels.

- an asymmetric one, with 5^{th} harmonic pump and 9^{th} harmonic probe, using O_2 and monitoring the delay dependent yield of O^+. An asymmetric filter configuration is needed, with $200nm\ In$ on one side to selectively pass energies in the $11-17eV$ range and the MgF_2 glass on the other. Although the total photon energy for $7^{th} + 7^{th}$ and for $5^{th} + 9^{th}$ is the same, in the second case the photon energy of the pump is in the Schumann-Runge continuum and the behavior of O_2 after the interaction with the pump pulse is quite well known from literature. In this case traces are expected to show as well the opening of the dissociative channels, plus the zero-delay should appear as a step in the O^+ yield, due to the arrival of the probe pulse before the pump.

As described in sec. 2.1, after the harmonic generation a silicon plate at Brewster angle for IR is used to reflect most of the harmonics and to cut most of the IR. The original plan for this experiment consisted in changing this "single silicon plate" configuration to one with three reflections: the first and the third on two silicon plates, the second one at the edge of two different elements, one silicon to reflect all the harmonics and one dielectric mirror to reflect mainly the 5^{th} at an angle of 75°. The residual harmonic intensity after three reflections is not high enough to perform pump probe experiments, so we needed to switch to the above described configuration with transmission filters.

5.1.2 Results

Within the $5^{th} + 5^{th}$ scheme, we performed several time-delay scans in order to measure the FWHM difference between O_2^+ and Kr^+. Even though several AC traces shows that such a difference can be in the range of $5fs$ to $15fs$ for different pulse durations, this does not allow us to define a value for such broadening for the following reasons:

- the fit error on each trace is in the range of $2fs$ to $6fs$, depending upon the quality of the trace. This would put the time difference very close to the experimental error. Also, the difference is small as compared to the overall duration.

- the issue mentioned above could be anyway fixed if consistent statistics were available. In fact, in further traces such difference is too close to zero, or AC traces for Kr^+ appear sometimes even longer than O_2^+.

- the estimation of FWHM time duration of the AC traces looks to depend on the signal to noise ratio: as Kr^+ has usually weaker signal, part of its AC trace is within the background noise level, so that it may appear shorter for this reason.

An O_2^+ trace is shown in fig. 42, which is obtained by averaging 5 independent scans. Each of them includes two consecutive traces, from a mirror displacement of $35.0\mu m$, a step of $0.1\mu m$, each step being the average of 14 data points, so that each point represent an average of 140 laser shots. In time this corresponds to an interval $230fs$ long, $\pm 115fs$ from the zero delay, and steps of $0.66fs$.

Within the the $7^{th} + 7^{th}$ scheme, in fig. 43 we compare our data for O^+ with the results published by *S.A. Trushin et al. J. Phys. B. 2011* [82]. The differences between the two plots are related to the different contrasts of the peaks and to a small offset of the x-axis (about $5fs$). Concerning the contrast, in our experiment we expect a lower one, as one XUV photon pump - one XUV photon probe process is involved, while in the other case the system

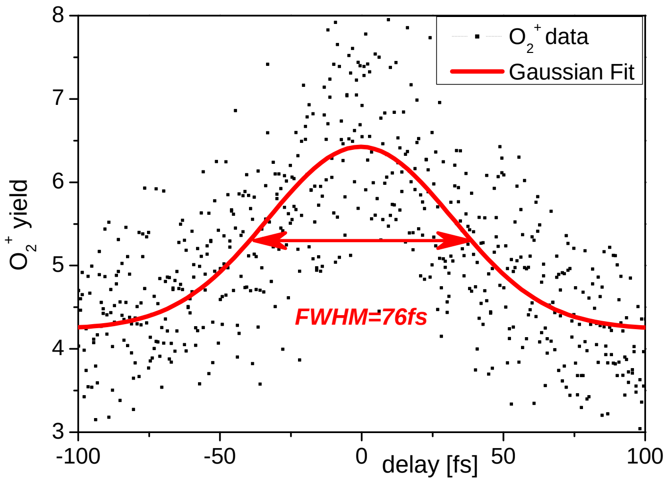

Figure 42: Time delay scan for O_2^+ with MgF_2 glass inserted. The FWHM of the Gaussian fit is $76fs$.

is probed by multi IR photon absorption. For the offset in the delay scales there are two explanations. Firstly, due to the different excitation schemes, it is reasonable that the peaks may appear in slightly different time windows. Secondly, the zero delay is defined differently in the cross-correlation trace and in the auto-correlation. Furthermore, in this particular experiment, because of the MgF_2 filter, whose faces are not exactly parallel, the zero delay depends upon the wavelength. In this case the difference of $5fs$ can be within the uncertainty of the two methods (note that for cross-correlation, the zero delay is defined by the maximum of Ar^+ signal during the record, and that the IR pulse has a duration of $10fs$. In our case it is defined as the center of symmetry of the trace of fig. 42.

Concerning the third proposed configuration, the asymmetric one for 5^{th} harmonic pump - 9^{th} harmonic probe, we proceed in two steps:

1. the preliminary step, in which a MgF_2 glass is inserted in one half of the beam, and the second one is free of any filter, so that all the harmonics are available;

2. the definitive step, in which the In filter is inserted in the second half of the beam in order to selectively transmit mainly the 9^{th} harmonic

Unfortunately our set-up is optimized just for AC traces or similar, while it is not very suitable for asymmetric pump-probe scheme. This is mainly

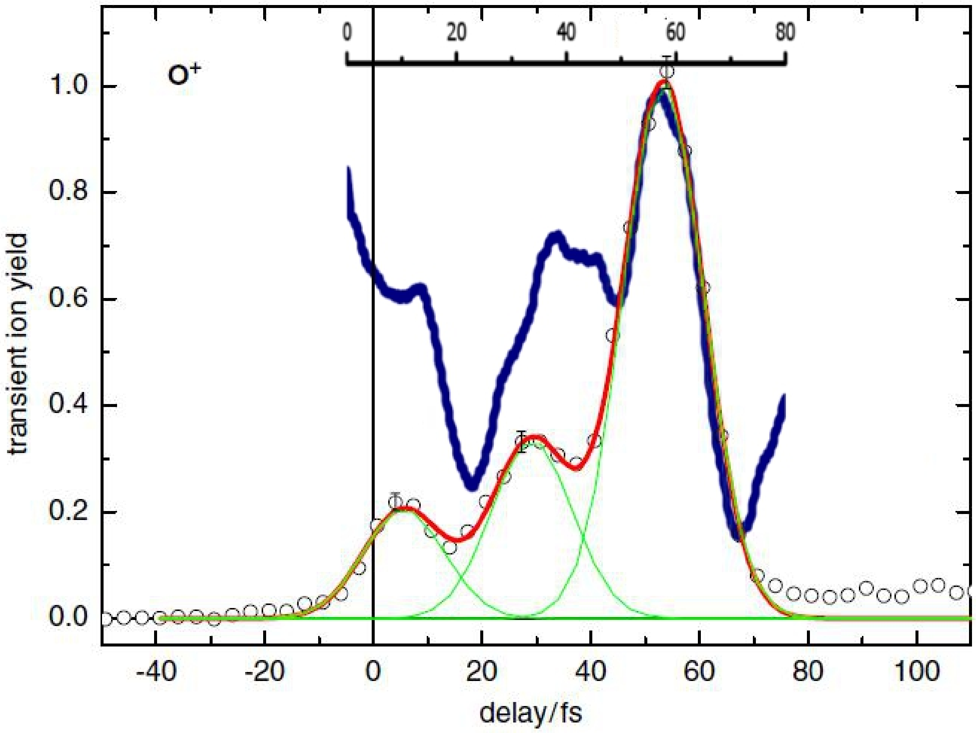

Figure 43: Comparison among our data (blue line) and the work of *S.A. Trushin et al. J. Phys. B. 2011* [82]. In order to show the comparison, our data are plot as a function of the absolute delay. In the cited work, oxygen is excited by $10fs$ pulses in the SchumannRunge continuum at $162nm$, which is by $0.57eV$ above the dissociation limit. It is probed by high-intensity ionization at $810nm$ with $10^{14}W/cm^2$, measuring the ion yields. In our case, O^+ is the product of 7^{th} harmonic pump - 7^{th} harmonic probe.

related to combined use of the split mirror and different filter configuration on each side: this produces different delay times and also different deviations for the two beams, so that spatial and temporal overlapping becomes more difficult. Another issue, typical of cross-correlations, is the definition of the proper amount of radiation for each wavelength, while in auto-correlation traces the same pulse is divided into two identical replica. When different wavelengths in the XUV are used, producing similar amount of ion signal can be a meaningful criteria, as long as equivalent processes take place, i.e. whether both wavelengths produce ions by a one photon process or both of them produce ions by a two photon process. In our case, the 5^{th} harmonic produces O_2^+ through a two photon process while the 9^{th} through one photon absorption. It also problematic to exclude with certainty the role of IR as at least one of the two beams cannot have thin metal filters: we can try to avoid its effects by reducing the laser intensity and the pressure in the production jet, though at the price of reducing the total yield of HOH. Also, in the evaluation of the acquired traces, symmetry cannot be used as the significant discriminating criteria to accept or reject the data.

None of the afore mentioned issues can alone prevent the success of the experiment; but their combination, together with the intrinsic difficulty in taking XUV-pump XUV-probe scan, constitutes a major experimental issue. Also, even in meaningful traces, it is impossible to exclude the presence of parasitic effects.

6 Appendix

6.1 Training in *Politecnico di Milano*: pump-probe experiments on diatomic molecules

6.1.1 CEP stabilized laser system

The "High Energy Attosecond Pulse Laboratory" in Politecnico di Milano is equipped with the CEP stabilized Ti:Sapphire laser system *Femtopower Pro V CEP*, provided by Femtolaser, which delivers $25fs$, $6mJ$ IR pulses at a repetition rate of $1Khz$. In the next section will be presented how the pulses are treated before being used for the generation of XUV radiation. In this section we present the main techniques which allow monitoring and controlling the CEP instabilities.

The first CEP control stage (XPS) provides the stabilization in the oscillator: the phase drift is measured with the frequency difference technique [29, 30, 57, 96] and the reaction takes place through an acousto-optical modulator acting on the pump of the oscillator. The idea of this technique is to overlap the spectrum of the oscillator with its frequency difference generated one: as the former carries information on CEP while the second does not, the variation of CEP, named Carrier Envelope Offset (CEO), can be retrieved.
A laser pulse, in the frequency domain, consists in a comb of optical frequencies:

$$f_m = mf_{rep} + f_0 \tag{67}$$

where m is a large integer, in the order of the millions, that indexes the comb line, f_{rep} is the repetition rate at less than $1GHz$ in general, and f_0 is the comb offset due to the CEO. The Difference Frequency (DF) spectrum is obtained by mixing the high and low frequency components of the original: so, from eq. 67 we obtain:

$$f_{DF} = (n_h f_{rep} + f_0) - (n_l f_{rep} + f_0) = (n_h - n_l)\, f_{rep} \tag{68}$$

Under the condition that the two spectra partially overlap, then the interference beat signal can by obtained at f_0 by 0-to-f comparison.

The second CEP control stage (APS, amplified phase stabilizer) provides the stabilization at the amplifiers: the phase drift is measured after

the amplifiers with the $f-2f$ technique [4, 39] and is compensated by adjusting the insertion of one of the two prisms located in the stretcher.
In this case the spectrum is firstly broadened (for instance by focusing in a photonic crystal fiber) to an octave spanning, then it is focused in a BBO crystal for frequency doubling. The broadened spectrum and its frequency doubled one are then recombined in a spectrometer.
From eq. 67, a low frequency in the broadened spectrum can be written as:

$$f_n = n f_{rep} + f_0 \tag{69}$$

As we requested the spectrum to be wider than one octave, there is an high frequency which can be written as:

$$f_{2n} = 2n f_{rep} + f_0 \tag{70}$$

There is though a region of overlapping between the high frequencies and the doubled low ones. f_0 appears in the beat between f_{2n} and $2f_n$:

$$2f_n - f_{2n} = 2\left(n f_{rep} + f_0\right) - \left(2n f_{rep} + f_0\right) = f_0 \tag{71}$$

6.1.2 Hollow-core optical fiber and chirp mirrors

In this laboratory, few-optical-cycle pulses are obtained by using the hollow fiber compression technique in the pressure gradient scheme.

As reported in [12], "the hollow fiber compression technique [61] is based on the propagation of laser pulses in dielectric capillaries filled with noble gases. Owing to nonlinear effects occurring during propagation, the pulses undergo spectral broadening: optical compression is then achieved by a dispersion delay line." The pressure gradient scheme [78], in combination with the use of positively chirped input pulses, is one of the techniques introduced in order to increase the energy of the compressed pulses. As well from [12], "the gas pressure inside the fiber increases from zero at the entrance to the maximum at the output of the fiber in order to minimize plasma-induced distortions of the laser pulse at the entrance of the capillary."

The hollow fiber is $1m$ long with internal diameter $\varnothing 340\mu m$; it is filled with He, whose pressure scales from $10mbar$ to $1bar$. Typical laser parameters at the input of the fiber are $\tau_L \approx 25fs$, $P = 6.0W$, which, with a laser repetition rate of $1kHz$, means $E_{pulse} = 5.5mJ$. At the output of the fiber, the laser power drops to $3.1W$ in case the fiber is in vacuum, and drops slightly more (to $P = 2.5W$) when the gas pressure gradient is applied. The dispersion delay line in this case is constituted by a set of negatively chirped ultra-broadband mirrors [13], which are dielectric optics with variable layer thickness, so that they can provide negative dispersion. After the compression, the pulse duration gets down to $\tau_L = 4fs$.It must be remarked though that chirp mirrors, at each reflection, provide a discrete negative dispersion compensation to the laser pulse. In order to finely tune the pulse duration, a discrete negative chirp is introduced and then it is finely compensated by the insertion of glass wedges, which provide positive chirp.

While adjusting the laser parameters before the fiber and comparing with the parameters after the compression, we noticed that an higher input energy does not correspond automatically to an higher output energy. Conversely, we realized that it is energetically more convenient to optimize the laser temporal profile by acting on the dazzler, rather than the energy at the input of the fiber: in this case less gas pressure is needed, and so also the energy loss is smaller.

The laser-fiber coupling is one of the critical aspects of this technique: in particular, the laser alignment before the lens used for the coupling has to be kept so stable that an analog feedback system is required. This fast system uses a parasitic reflection of the laser at the window of the vacuum chamber where the fiber is located. This control has the purpose to prevent a drift of the laser focus from destroying the head of the optical fiber.

6.1.3 XUV line and IR delay line

After the compression of the pulse, the IR pulse is spatially split into two parts with a drilled mirror: the inner part is used for the generation of the XUV, thus for the pump, while the outer part is used for the IR probe. This is a temporary solution: as long as the energy ratio will be defined, a beam splitter will be used. Before focusing the IR into the gas cell, a collinear PG, with multi-order $\lambda/4$ waveplate, is also available in case XUV IAPs are required.

In a first vacuum chamber the gas cell for HOHG is mounted on alignment stages, powered by step motors. After the gas cell, a $150nm$ Al filter is used to separate the IR, used for generation, from the XUV radiation. In this chamber, within the line of the probe pulse, a piezoelectric controlled delay stage controls the pump-probe delay.

In a second chamber the IR for the probe and the XUV for the pump, previously separated by a drilled mirror, are recombined to the same optical line thanks to another drilled mirror. It must be remarked that the rough and

the fine delay between the XUV pump and the IR probe cannot be adjusted after this mirror. For the rough delay adjustment, the gas cell is turned off, the Al filter removed, and an IR mirror is inserted in the line after this drilled mirror in order to image the IR for the pump and the IR for the probe onto an external CCD camera, which allows the user to monitor the appearance of interference fringes. The fine delay is instead checked, when the pump-probe experiment is almost ready, by launching a quick delay scan and monitoring the signal at the Velocity Map Imaging (VMI).
In a third chamber there is the toroidal grazing mirror to focus both the IR and the XUV in front of the gas jet, which is integrated in the repeller of the VMI in the detection area, in a dedicated vacuum chamber.
After the interaction, the XUV beam is acquired in a spectrometer, which keeps the spectrum monitored for the whole duration of the experiments.

6.1.4 VMI

"In contrast to the conventional TOF method, where kinetic energy release information is contained in the temporal structure in the arrival period of ions of a specific mass or electrons, the ion imaging technique extracts all the information from the spatial appearance of a 2D image" [22].

Theory: the basic principle of the Velocity Map Imaging is that particles emitted with the same velocity vector are incident of the same point of the detector, even if they are emitted in different regions of the interaction volume. This can be achieved by accelerating the charged particles with a system of electrostatic lenses, which in time have evolved from grid configuration to open electrodes [22]. The detector usually consists in a MCP double stack coupled with a phosphor screen. In order to select a particular ion species, it is possible to gate the MCP so that it is synchronized with the arrival time of such particles.
Still, despite the increasing accuracy of these apparatus, a 3D distribution of particles is mapped onto a 2D detector, so that it is necessary to perform an inverse transform in order to retrieve the 3D distribution from the 2D image. "If the 3D momentum distribution contains an axis of symmetry in the plane of the detector, the measurement is an Abel projection, and the 3D momentum distribution can be retrieved from the 2D projection by means of an inverse-Abel transform" [92]. Several computational techniques have been proposed to perform such inversion. In this laboratory it is used a technique recently proposed and developed by *M. Vrakking*. The improvements with respect to previous techniques rely on the fact that in this case

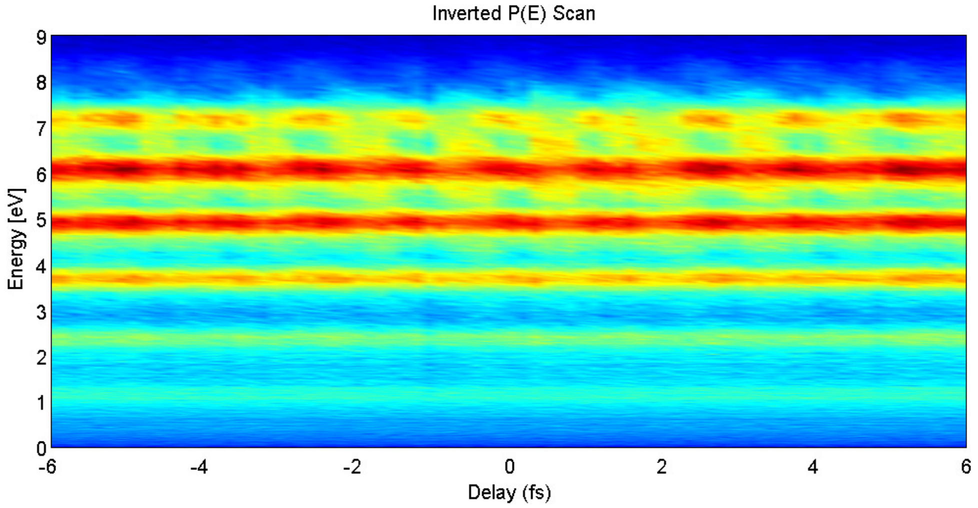

Figure 44: Rabbit trace with VMI. The modulation of the side bands is more clear within the interval $-4fs \leq \tau_D \leq +4fs$. *Courtesy of the High-energy attosecond pulse laboratory, Polimi.*

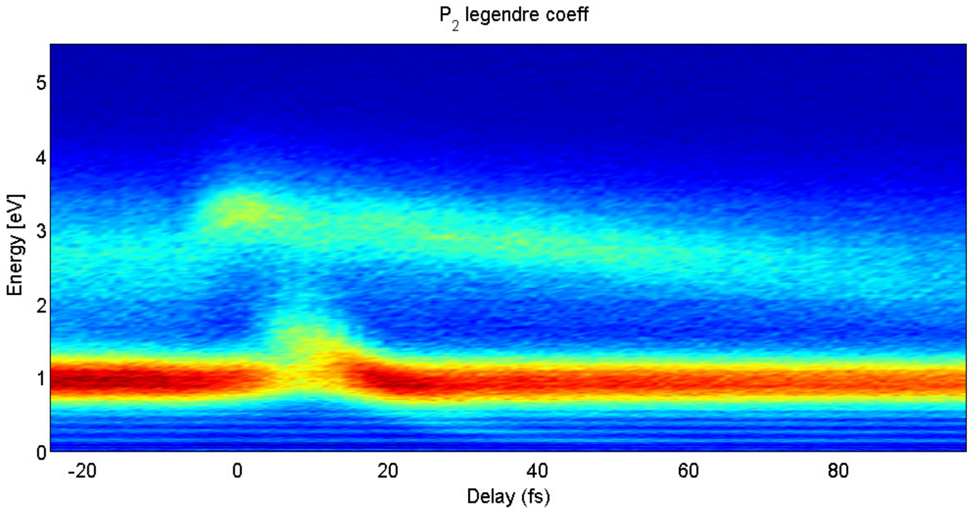

Figure 45: Yield of N^+ in XUV pump - IR probe scan. Two dynamics appear clearly: a slow one on the $100fs$ time scale at $3.5eV$, and the depletion of the F band at $\approx 1eV$ on the $10fs$ time scale, which corresponds to the dissociation of the molecule through the $2\Sigma_g$ state. *Courtesy of the High-energy attosecond pulse laboratory, Polimi.*

the constraints on the angular distributions, given by the nature of photon-matter interactions, are firstly taken into account. "Following the work of Lambropoulos [21] and coworkers, it is known that the angular distribution that can be obtained in a multi-photon ionization consists of a superposition of Legendre polynomials, where the highest order polynomial involved is determined by the order of the multi-photon ionization process.[...] This approach allows us to cast the inversion problem in terms of a simple matrix multiplication that is both extremely fast and immediately connects to the underlying physical process." [67] Thus it is shown that, being $\vec{b}$ the vector representing the 2D projection, it can be obtained by $\vec{a}$, which represents the 3D momentum, by a matrix multiplication:

$$\vec{b} = \mathbf{M}\vec{a} \tag{72}$$

Using the inverse matrix $\mathbf{M^{-1}}$, the 3D distribution can be retrieved by the 2D image according to:

$$\vec{a} = \mathbf{M^{-1}}\vec{b} \tag{73}$$

One remarkable point is that, in eq. 72 and 73, "while the vectors $\vec{a}$ and $\vec{b}$ depend on the specifics of the map imaging experiment, the matrices $\mathbf{M}$ and $\mathbf{M^{-1}}$ do not. Hence, once these matrices have been determined, they can be used repeatedly to perform inversions".

Data: we acquired data for two types of measurement, Rabitt and XUV pump - IR probe on molecules.
Rabitt [63], [5,20,50,51] measurements provide information on the temporal structure of both the XUV and the IR pulse. It is also a good indicator of the interferometric stability of the XUV - IR delay line. The intensity of the IR beam has to be set so that only 1 IR photon + 1 XUV photon effects take place. This can be achieved by finely tuning the amount of IR by regulating an iris while checking in real time the quality of the Rabbitt signal on the VMI. An example of Rabbitt scan is shown in fig. 44.
In order to set properly the IR intensity in XUV pump - IR probe measurements consists, the XUV beam has to blocked and the signal due only to the IR radiation should be just at the minimum threshold of visibility. In fig. 45 is reported an example of pump - probe scan. In this case N_2 is the investigated molecule, and the experimental observable variable is the momentum distribution of the released N^+ ions. The trace has been inverted, according to the procedure described in the previous paragraph.

6.2 SIMION

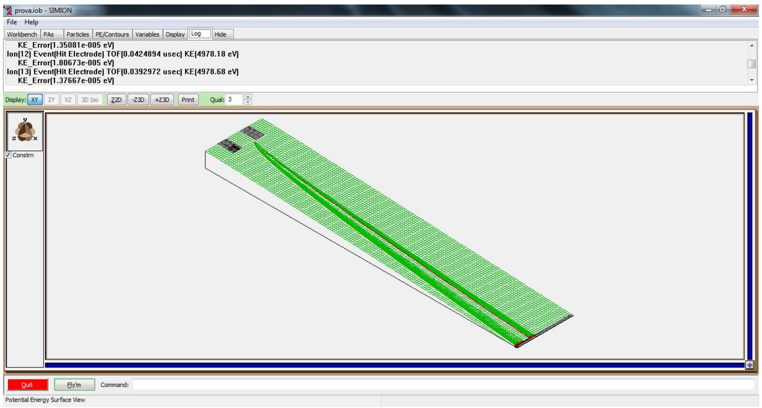

```
    KE_Error(1.35081e-005 eV)
Ion(12) Event(Hit Electrode) TOF(0.0424894 usec) KE(4978.18 eV)
    KE_Error(1.80673e-005 eV)
Ion(13) Event(Hit Electrode) TOF(0.0392972 usec) KE(4978.68 eV)
    KE_Error(1.37667e-005 eV)
```

Figure 46: A screen shot from the SIMION interface during the simulation, showing a $2D$ section of the interaction area, the electric potential, the trajectories of the ions. On top are reported the requested parameters: in this case, TOF and the estimated computation error on the kinetic energy.

The TOF spectrometer can be set in only one of these configuration per time: energy spectrometer for electrons or mass spectrometer for ions. In this case the gas jet is floated at +5KV and works also as a repeller, while the entrance of the TOF is grounded. The charged particles ionized by the interaction with the XUV beam are accelerated by the electric field and are detected by the MCP in the end of the TOF.

In such a configuration the TOF spectrometer is not supposed to give any information about the initial energy of the charged particles, which anyway is almost zero for atoms. The case of molecules is different: charged particles can be emitted with an initial kinetic energy.

In our scan over delay traces, we observed clearly a broadening of the H^+ peak in the order of few nanoseconds. Let us consider two particles which are emitted with the same energy (for example 1eV) but in opposite directions along the axis from the jet to the TOF. If we consider the applied voltage of 5000V and the geometric configuration with a distance of about 1cm between the electrodes, it can be shown that the difference in the time of flight of such particles would be about only half a nanosecond. This assuming that the accelerating electric field is uniform in time (true) and in space: this last assumption has to be verified.

In fact, the jet is a metallic straw with a small hole (1mm). The assumption of constant electric field would be valid in case that the charged particles are produced at a distance large compared to the diameter of the hole. This is not the case, as during the alignment of the whole system we try to focus the

XUV beam as close as possible to the jet in order to maximize the signal.
We used then the program SIMION to check how much can be the time difference between the particles described above in case of non-uniform electric field. When preparing the simulation it is important to define a resolution fine enough to resolve the variations in the electric field in the region close to the tip of the gas jet, which is also the repeller.
We simulated the flight of 8 particles (fly'em, using the terminology of the program), combining the two opposite directions, two values of initial energy (0.5eV and 1.5eV) and the position with respect to the hole of the jet (close to the center or to the edge). We repeated this for different distances from the jet ($100\mu m$, $14\mu m$ and $5\mu m$) and found out that, the smaller the distance, the bigger the time gap in the couple of particles with anti-parallel velocity. A lower limit to the distance between the produced charged particles is given by the size of the XUV beam focus, $2\mu m$.
The typical times given by the simulation are of the order of a few nanoseconds, like the broadening in the scan over delay traces.
These simulations do not have the purpose to provide a calibration of the TOF, so that it can be used to measure particle momentum. They are just intended to verify that the broadening that we observe is a function of the delay and it can be ascribed to the initial energy of the particles that we are studying. Also, the values found in the simulation do not represent the FWHM of the peak: in the experiment the laser radiation is polarized along the horizontal axis, that is the jet-TOF axis, but the H_2 molecules are not aligned, so that we must assume that the emitted Hydrogen ions have some unknown angular distribution. Furthermore, the distance between the XUV beam focus and the jet is not known: as mentioned before, it is minimized during the alignment, but it is not measured.
With this simulation, we can be confident that in the ion mass spectra, in the H^+ peak the tails contain the protons with higher initial kinetic energy, while protons with initial zero kinetic energy have to be in the center of the peak. Note that also protons emitted with non-zero kinetic energy, but perpendicularly to the axis from the jet to the TOF, appear in the center of the peak as well.

6.3 Technical solutions: piezo-driver for integrated jet-repeller at 20KV

The ion microscope has been originally designed to work with radiation from IR lasers, which can easily provide very high intensities: in this case it is enough to diffuse some gas in the whole chamber at very low pressure ($P \approx$

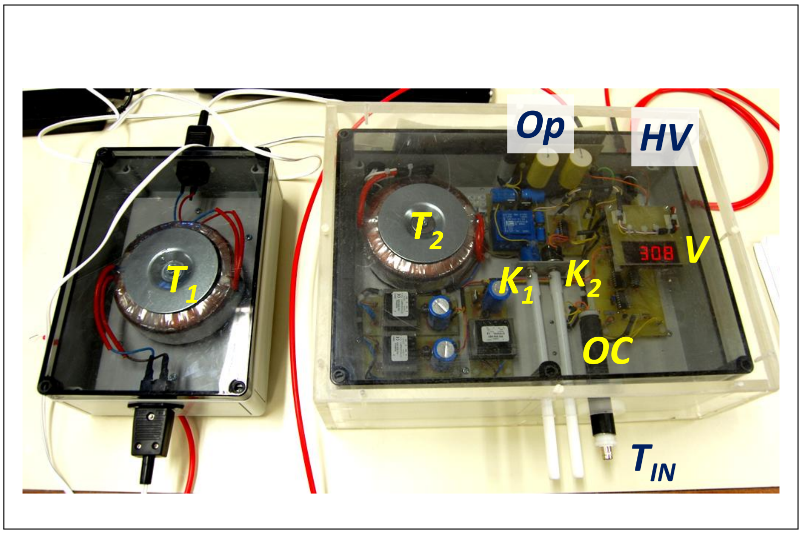

Figure 47: Driver for piezoelectric gas jet floated at $20kV$.
T_1, T_2: transformers for the power supply, providing $10kV$ insulation each. K_1, K_2: controllers for negative square pulse duration and voltage. V: voltage indicator for the square pulse. OC: optical coupler. Allows to transmit the trigger to the driver while being floated at $20kV$. See also fig. 48.T_{IN}: trigger in, TTL signal from delay box. O_p: output square pulse, to drive the floated jet. HV: high voltage, from the HV supply of the ion microscope: it floats the repeller, the jet and the whole driver.

$10^{-6}mbar$). In order to be able to produce any signal just with the HOH, it is necessary to have much higher pressure in the region of interaction between the harmonics and the gas. As it is the very same problem as in the detection area 1, the solution must be the same: a high voltage floated $10Hz$ pulsed gas jet. In the case of the ion microscope the jet would be required to act also as a repeller with a floating voltage of $20kV$, while our available driving electronics allow a floating of at most $5kV$. Also, we have verified both theoretically and experimentally that it is not possible to operate the piezoelectric crystal of the jet with a floating voltage of $5kV$ and to have the front part of the jet, even if separated by ceramic materials, at $20kV$. For any distance between two electrodes with a given high difference of potential, the continuous variation of the gas pressure from atmospheric values to high vacuum ones (because the gas jet is pulsed) makes the system to pass through the minimum of the Paschen curve, which relates for a given medium the discharge voltage as a function of the product of distance and pressure: sparks are inevitable. Although we realized that it is possible to set the ion microscope to operate properly also with a repeller voltage of just $5kV$, we developed a new electronic driver supporting higher floating potential.

The problem can be summarized as follows: a driver for the jet takes in input the power from the electric outlet, the settings of height and width of the pulse with two knobs, and the trigger to synchronize the jet to the laser. All these inputs are grounded and, as shown in the picture of fig. 47, they have to be decoupled from the driver when it has to be floated. The driver has to be kept in an insulating box to avoid discharges. Concerning the knobs, they can be controlled with plastic or ceramic sticks, mounted in such a way to guarantee a minimum distance of $20cm$ between the user and the driver. For even better security, radio controls can be considered. For the power provided with standard AC current, it is just a matter of placing in series two transformers with insulation of $10kV$ each.

The decoupling of the trigger signal was the main issue: it is not possible to use a transformer like in the case of the normal $5kV$ floated driver. In order to have the required insulation and, at the same time, to preserve the quality of the trigger pulse, we developed a long distance (up to $20cm$) photo-coupler. The key element of this device is the IR photo-transistor OPL550, which acts as a photo-controlled switch. It is quite intuitive that the trigger can be sent to an IR led whose light controls the photo-transistor with no issues concerning the difference of potential as long as the two elements are far enough. If, by adding two lenses, we set an optical scheme as in fig. 48, the receiver can operate at whatever distance from the emitter, with no risks of discharges.

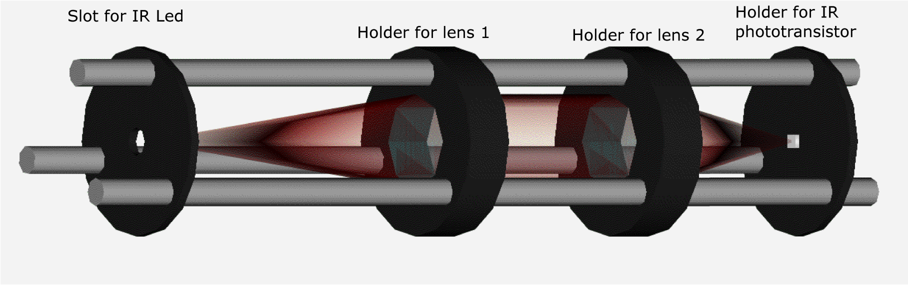

Figure 48: Project scheme of the photo-coupler. The IR led (the emitter) is mounted on the left support, the photo-transistor OPL550 (receiver) on the right. The two lenses in the middle allow the photo-transistor to have enough light from the IR led for any distance between the two.

6.4 Magnetic Bottle: theory and construction

The collection efficiency of photoelectrons can be improved, without particular loss of resolution, by arranging a magnetic bottle configuration in the detection area.

Theory: the TOF in ion mass spectrometer configuration uses an extraction potential of $5kV$, so most of the produced ions are accelerated towards the detector and are collected. In the photoelectron energy spectrometer configuration, no extraction potential - or very little, in the order of $5V$ -is applied in order to preserve the energy resolution. As a consequence, only the photoelectrons which are emitted in the very direction of the detector are collected. One way to increase the efficiency of collection is to set a magnetic bottle TOF, as presented in [45].
The idea of the normal TOF is that a small hole between the gas jet and the MCP selects only the electrons which have been emitted in the same direction, so that their TOF represents their kinetic energy: should electrons emitted with different directions be allowed to get to the MCP, electrons with the same energy but different directions would have different TOF. The relation between TOF and kinetic energy would not be bijective anymore.
A uniform magnetic field in the gas jet - detector direction would allow electrons emitted at different angles to reach the detector; in this case the TOF would represent only the projection of the total speed along the direction of the magnetic field, thus destroying the energy resolution. A non uniform magnetic field instead allows to obtain high collection efficiency without loosing the energy resolution. Under the conditions that :

- the magnetic field B_I (initial) in the region of emission of the photoelectrons is much stronger than B_F close to the detector
- the magnetic field B_F (final) is uniform along most of the distance between the emission region and the detector (this is similar to the condition for the ion mass spectrometer that the region of the electric field is much shorter than the total distance to the detector)
- the gradient is not too large (which means that the change in the field acting on an electron during one orbit is negligible with respect to the total field) so that the motion of the electron can be solved in the adiabatic limit

The TOF for electron emitted with the same energy but variable angle θ_I is expressed by:

$$T_{drift} \approx \frac{l_{drift}}{v}\left(1+\frac{B_F \sin^2\theta_I}{2B_I}\right) \tag{74}$$

so that the dependence on θ_I is very weak for $B_F/B_I \ll 1$.

Realization and characterization: we need two magnetic fields: B_I, which should be very intense in a small region, and B_F, which should be

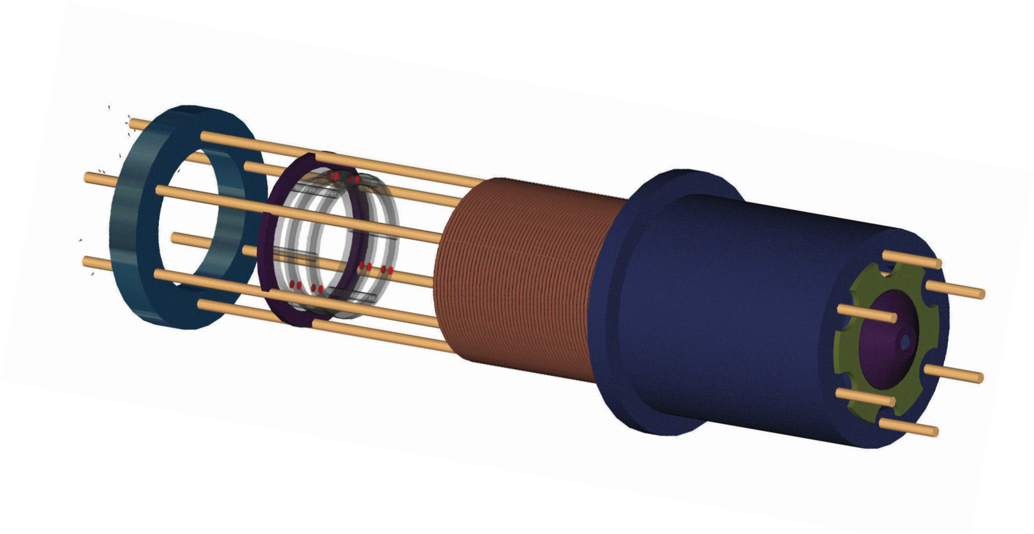

Figure 49: Coil and its frame for magnetic bottle TOF spectrometer. The coil is represented only in one part of the drawing, while in reality it covers the whole distance from the detection area (on the right) to the MCP (on the left). Inside the coil a double grid is installed: it can be grounded or provided some potential to accelerate the electrons.

weak and constant in a large region. For B_I we use a ring magnet $\varnothing 5/0.5mm$, height $4.6mm$, chrome plated, N52, which can produce $0.5T$ magnetic field at its edges. The magnet has ring shape so that it can be used as the tip of the gas jet. For B_F we built a coil, so that the field is tunable by adjusting the current. It has been measured with a Gaussmeter that inside the coil $dB/dI \approx 11G/A$. In fig. 25 of sec. 3.3 are compared two PES acquired with and without the magnetic bottle.

distance [mm]	3	6	8	11	13	15	19	26	35	70
magnetic field [G]	1000	500	200	100	70	50	25	10	5	2

Table 2: Permanent magnetic field of the magnet measured at different distances on axis.

6.5 Electronic driver for magnetic jet

Commercially available drivers for pulsed valves are flexible but relatively expensive devices. Once the working conditions are defined, it is easy to build more specific but much cheaper drivers.

The electronic support of Forth can normally provide drivers for piezoelectric controlled pulsed gas jets. The piezoelectric crystal requires an high voltage $(300 - 500V)$ and small current. As mentioned in sec. 2.1, we tested also

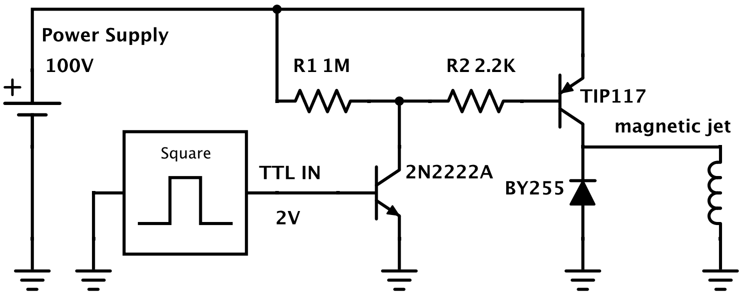

Figure 50: A simple driver for magnetic jet. It amplifies the input flat-top TTL pulse from the delay box to a flat-top pulse with the same duration and the amplitude defined by the power supply.

some magnetic pulsed jet. As they have the typical load of a coil, they do not require too high voltages, but after a transient time they behave like a closed circuit, so a high current may pass, thus burning the power transistors of our usual drivers. Also, when they are not powered anymore, they release the energy stored in the magnetic field as induced current: again, this may burn our usual drivers. As in the laboratory both power supplies and delay boxes are largely available, a driver can be built just by applying the definition of transistor (*semiconductor device for amplifying and switching electronic signals or electric power*) to an amplifying circuit like the small one in fig. 50. This circuit is powered by an external power supply and takes as input from the delay box a square TTL flat-top pulse ($2V$) with variable duration. This pulse is amplified to another flat-top square pulse, whose voltage is set by the power supply ($\approx 80 - 100V$) while the pulse duration is the same as for the input. The *TIP117* is the power transistor. Its base must be almost at the same voltage of the power supply, so that another transistor *2N2222A* is necessary to drive it. In this way it is possible to keep the flat-top logic both in input and output. The diode is necessary to avoid the discharge current of the coil to enter the circuit.

6.6 Notes on the alignment feedback system: settings and development

The pointing instability we intend to stabilize affects the energy distribution of the beam profile. It is monitored by the laser intensity of four points in the periphery of the beam profile by a mask, a lens and a 4-radiants photo-diode. It is controlled by acting on a mirror in the laser amplifier.

6.6.1 Settings

A Proportional Integral Derivative (PID) controller is a negative feedback system for the stabilization of a parameter. Its total action u can be expressed as:

$$u = u_p + u_i + u_d \tag{75}$$

where

$$\begin{aligned} u_p &= K_p \cdot e \\ u_i &= K_i \cdot \int e(t)\mathrm{d}t \\ u_d &= K_d \cdot \frac{de}{dt} \end{aligned} \tag{76}$$

are the proportional, integral, and derivative actions of the controller. Clearly, the integral action has memory on the previous values of the error e, while the derivative action controls and compensate for fast variations. An efficient performance of the controller requires a proper setting of the constants K.
In our case attention must be paid in order to avoid the system to try to correct shoot to shoot random and large variations, while its purpose is to correct, with the least movements, a slow, small, constant and one-directional drift. It is important then to compare the random fluctuations with the systematic ones. Obviously, in such conditions, *the integral action is the only suitable one.*
For instance, in an out-of loop test, without the mask, setting the oscilloscope to 128 averages and the program to 4 internal averages (which means a total of 128 X 4 = 512), the random fluctuations are of the order of 2-3%; with 8 internal averages they are reduced to 1%. The systematic laser drift is measured in 15% variation in 30 minutes.
Repeating the same test with the mask inserted, we find out that random variations are similar or slightly larger, while sensitivity to laser drift is clearly improved: a variation of 15% is measured in only 5 minutes.
It must be also noted that the laser shoot to shoot variation is known to be in the order of 10%. The acquisition over 100 shots should already bring the relative error to 1%, while in this case this happens only after about 800 acquisitions: but the whole electronic apparatus, that is the photodiode, its analog amplifiers, the oscilloscope and its communication with the program, introduces more uncertainty. Also 10% variation refers to the total energy of the pulse, while in this case only the energy from a small fraction of the whole area is monitored: in this case it is reasonable to assume that larger variations may take place.

Any misalignment in the laser amplifier may cause severe damage to the system. So, for safety reasons, before allowing the feedback system to control the alignment inside the $10Hz$ amplifier, we arranged a small set-up to verify the closed-loop operations out of the laser alignment. First, a thick ($2.5cm$) plate of plexiglass is put in front of the detector. By tilting it, it is possible to simulate the drift of the laser profile that we want to control. Then we place another identical plate of plexiglass, but installed on a typical mirror mount which is controlled by the feedback system through piezomotors. In this case, when we move the first plate, the system slowly tilts the second one in order to compensate the drift, until the two plates are tilted with the same, but opposite, angle. It is important to check that the reaction of the system is negative, so that it compensates for the misalignment, and not positive, otherwise it would increase it even more.

6.6.2 Development

With the dismantling of the current laser system in September 2013, the feedback system is not in use anymore, but it may be re-adapted for the new laboratory. The technical issues, which determined our choices for its realization, and the project details may provide useful guidelines for this conversion.

Choice of the type of system: digital vs analog.

The choice between analog or digital systems concerns almost any applications that can be thought of. In order to choose, it is important to know which advantages are offered by each of them.

Analog systems, made of passive (capacitors, resistors, diodes) and active (transistors, operational amplifiers, logic operators, photo-electronics) components, are usually cheap and have very fast response (that is, they can be much faster than the 1kHz repetition rate of the secondary laser beam), even though they require some specific knowledge for the project. Analog system must be inevitably chosen for the simplest applications, like: power switches for piezo-electric or magnetic jet, logical operators for frequency dividers, manipulation (amplification, derivation, integration, summation, differential amplification) of electronic signals from basic devices (photodiodes, pressure indicators).

Even the basic knowledge of circuits, diodes, transistors, operational amplifier, logical operations and similar concept, allows to handle or to build standard devices for most applications. Proper software (NI:Multisim for instance) can be useful in the simulation of real circuits.

Even the most complex problem can be controlled by an analog circuit, but in this case its engineering may be far beyond personal competences: for example a PID controller to stabilize the pressure of jet in the detection area by monitoring the pressure and changing the voltage of the driving jet accordingly. This can be the field of the digital solutions, if the temporal requirements are not too strict (which means, if very high response speed is not required). Digital solutions have the great advantage that all the operations are controlled by a software, which can simulate almost any existing instrument. This also means that, in case of malfunctioning, there is no need to search for short circuits, oxidized components, burned elements or similar: all the attention can be focused on the program itself. There is not any limit in monitoring all the inputs and outputs at the same time. Also, most users are more familiar with software programming rather than with circuit engineering. The main drawback is the response speed, which may be not very fast. Computers and I/O digitizer are required, but they are usually already available in laboratories. The most common software for the communication between computers and scientific instruments is NI: Labview. Despite the interface, unusual for standard programmers, the dataflow visual programming language and environment is quite intuitive, while the basic logic of programming is independent of the environment.

Choice of the components.

A general computer-programmed digital system is composed of a detector, an amplification circuit, a digitizer, the computer and the program, an actuator (a motor, a voltage or current controller) with its related computer interface. Some digitizer include I/O communication, like the NI: USB-6009. In our case the detector, that is the 4-radiants photodiode, was ready and with an integrated circuit for output comparison and amplification. There are four output signals, two per direction in a 2D scheme, and each of them provides a sharp peak, with a duration $\approx 1\mu s$ and max $\approx 1V$. The properties of the signal define the requirements of the digitizer. The output voltage is high enough; should it be too high for a certain device, can be simply reduced with a resistor partition. The pulse duration is not too short, but it is for a device like the NI: USB-6009, which is supposed to be a digitizer for acoustic system with a limited bandwidth of 24kHz. One possible option is to use an Operational Amplifier (OP-AMP) to prepare an integrating circuit with also a certain amplification. Or to order a suitable device, with larger bandwidth. Or, at least in the preliminary phase, to use an available one even if over dimensioned for our need, like an oscilloscope with USB interface. Our output has to be a control over optics alignment, so it clearly has to be a step or piezoelectric motor. We have available piezoelectric motors, with their own driver interfaced with the computer through serial port.

Hw and Sw configuration.

Most commercially available electronic instruments are offered with included drivers (usually available at the website of the manufacturer) for PCI or PXI interfaces. It is then just a matter of installing the drivers and choose which program we want to use. Despite a user may feel more confident with Mathematica or C++, NI:Labview is highly recommended both for the large variety of included functions for the analysis of electronic signals, both for the good amount of samples usually provided by the manufacturer together with the drivers. So, in this case we can find quite many ready programs both for the data acquisition from the oscilloscope both for the motion control of the step motors. Such programs are thought to be working for most applications by all the possible users, so they are large, complex and full of details which are not needed for each particular situation. Also, given that coding down such a program from scratch is not an easy task even for experienced programmers, the most appropriate way to proceed is to collect some blocks of a large existing program and put them together in a smaller and simpler one. This shall not have all the functions and options offered in the sample program, but it shall have all and only the ones we need for our specific application. NI:Labview has the useful feature that each program can be saved as a "closed box", called sub-routines or SubVis (stands for sub virtual instruments), just with input and output, performing its assigned task, and it can be used as a standard function in a bigger program (it is analogous to the *functions* of C, for example). For instance, concerning the I/O communications, we need to initialize the oscilloscope (SubVi1), the motors (SubVi2), read the oscilloscope (SubVi3), read the motor position (SubVi4), move the motors (SubVi5), close the communication with the motors (SubVi6), close the communication with the oscilloscope (SubVi7). All this SubVis can be placed in the main program, which will launch them assigning the proper arguments and reading the output communications, which are used to determine the next steps.

Simulations.

If we want to develop such a system, we need to keep it tested in every stage. This should include the availability of all the resources which have to be included in the final project. Of course it is not very reasonable to use most of the resources of the laboratory when it is possible to simulate some components. As an example, once the signal of the detector has been characterized, the laser is not required anymore as long as the detector can be substituted just by an electronic wave function generator while developing or testing the program. Also, nobody wants to have the alignment of the multi-pass amplifier to be controlled by a software before this has been extensively tested. Series of test setups have to be arranged for simulations, going from the more basics ones to those closer to the final system. So, we start by checking that the amplitude variation in a square waveform from a waveform generator has the effect of starting the motion of a piezo-electric motor, that this motion is controlled and in agreement with expectations. We finish by checking that the laser drift detected by the four radiant photodiode makes the motors to re-align the laser beam to its assigned direction. While increasing the level of the simulation towards the real system, new effects have always to be kept into account: as an example, when working with the real detector rather than with a waveform generator, there are shoot to shoot variations which have to be considered.

The program.
The program, once the I/O communications have been initialized, has the task of reading the signal of a detector and to decide the movement of the picomotors accordingly. Thus, it performs the following operations in a cycle:

- to read 4 channels (up down left right) from the 4 radiant photodiode through the oscilloscope (variable: $currentvalue1..4$)
- to memorize the latest n acquisitions of $currentvalue1..4$ in a vector $CH1..4averaging$
- at a command of the user, to take for each channel the average of the last n acquisition saved in $CH1..4averaging$ as a reference (variable: $reference1..4$)
- for each acquisition, to evaluate the variation of each channel from the reference (es: $var_{left} = current_{left} - ref_{left}$) and then to evaluate the laser drift (es: $drift_{horizontal} = var_{left} - var_{right}$)
- to memorize the current drift in a vector $memory1..2$. Note that the channels are four, but the variation of the difference of each couple gives the two laser drifts, the horizontal and vertical one. Also note that the drift is defined by the variation in time of the difference between two channels, and not by the difference itself: this latter case would imply the desirable but not obvious condition that the initial difference between each couple of channels (up-down, left-right) should be zero.

- when the laser drift exceeds a given minimum threshold, to move the relative motor accordingly and to reset all the averaging vectors. Note that this operation does not change the $reference1..4$, which are taken at a command of the user just in the beginning of the operations, while the $memory1..2$ vectors, containing the n latest values of $laserdrift1..2$ is reset to zero. This is important to avoid an average-dependent overshooting. Conversely, the average of the laser drift remains underestimated as long as all the zero-values in the $memory1..2$ vectors are not substituted by the real values: this behavior is appropriate in the actual circumstance that the laser drift is slow (minutes) compared to the averaging (less than 1 minute), while the adjustment is quick (less than 1 second).

Glossary

2-IVAC 2^{nd} order Intensity (or Interferometric) Volume Auto Correlation.

AC Auto Correlation.

AIS Auto Ionizing States.

APT Attosecond Pulse Trains.

BBO Barium Borate.

CEO Carrier Envelope Offset.

CEP Carrier-Envelope Phase.

CPA Chirped Pulse Amplification.

CPG Collinear Polarization Gating.

DF Difference Frequency.

DMI Double Michelson Interferometer.

DMZ Double Mach-Zehnder Interferometer.

FEL Free Electron Laser.

HOH High Order Harmonics.

HOHG High Order Harmonic Generation.

IAP Isolated Attosecond Pulse.

IPG Interferometric Polarization Gating.

IR Infra-Red.

MCP Multi Channel Plate.

OP-AMP Operational Amplifier.

PES Photoelectron Energy Spectrum.

PG Polarization Gating.

PID Proportional Integral Derivative.

PM Phase Matching.

SAE Single Active Electron.

SHG Second Harmonic Generation.

TOF Time of Flight.

TPDDI Two Photon Double Direct Ionization.

TPDSI Two Photon Double Sequential Ionization.

VMI Velocity Map Imaging.

References

[1] W. Ackermann, G. Asova, V. Ayvazyan, et al. Operation of a free-electron laser from the extreme ultraviolet to the water window. *Nature Photonics*, 1:336–342, 2007.

[2] P. Antoine, A. L'Huillier, and M. Lewenstein. Attosecond pulse trains using high˘order harmonics. *Phys. Rev. Lett.*, 77:1234–1237, Aug 1996.

[3] P. Antoine, A. L'Huillier, M. Lewenstein, P. Salières, and B. Carré. Theory of high-order harmonic generation by an elliptically polarized laser field. *Phys. Rev. A*, 53:1725–1745, Mar 1996.

[4] A. Apolonski, A. Poppe, G. Tempea, et al. Controlling the phase evolution of few-cycle light pulses. *Phys. Rev. Lett.*, 85:740–743, Jul 2000.

[5] S. A. Aseyev, Y. Ni, L. J. Frasinski, H. G. Muller, and M. J. J. Vrakking. Attosecond angle-resolved photoelectron spectroscopy. *Phys. Rev. Lett.*, 91:223902, Nov 2003.

[6] P. Balcou, P. Sali'eres, A. L'Huillier, and M. Lewenstein. Generalized phase-matching conditions for high harmonics: The role of field-gradient forces. *Phys. Rev. A*, 55:3204–3210, Apr 1997.

[7] A. Baltuka, T. Udem, M. Uiberacker, et al. Attosecond control of electronic processes by intense light fields. *Nature*, 421(6923):611–615, 2003.

[8] E. P. Benis, D. Charalambidis, T. N. Kitsopoulos, G. D. Tsakiris, and P. Tzallas. Two-photon double ionization of rare gases by a superposition of harmonics. *Phys. Rev. A*, 74:051402, Nov 2006.

[9] L. Brugnera, F. Frank, D. J. Hoffmann, et al. Enhancement of high harmonics generated by field steering of electrons in a two-color orthogonally polarized laser field. *Opt. Lett.*, 35(23):3994–3996, Dec 2010.

[10] L. Brugnera, D. J. Hoffmann, T. Siegel, et al. Trajectory selection in high harmonic generation by controlling the phase between orthogonal two-color fields. *Phys. Rev. Lett.*, 107:153902, Oct 2011.

[11] K. S. Budil, P. Salières, A. L'Huillier, T. Ditmire, and M. D. Perry. Influence of ellipticity on harmonic generation. *Phys. Rev. A*, 48:R3437–R3440, Nov 1993.

[12] F. Calegari, M. Lucchini, M. Negro, et al. Temporal gating methods for the generation of isolated attosecond pulses. *Journal of Physics B: Atomic, Molecular and Optical Physics*, 45(7):074002, 2012.

[13] J.-P. Caumes, G. Sansone, E. Benedetti, et al. Imaging of recombination events in high-order harmonic generation by phase-stabilized few-optical-cycle pulses. *Journal of Modern Optics*, 53(1-2):67–74, 2006.

[14] D. Charalambidis, P. Tzallas, E. P. Benis, et al. Exploring intense attosecond pulses. *New Journal of Physics*, 10(2):025018, 2008.

[15] S. Chen, M. Chini, H. Wang, et al. Carrier-envelope phase stabilization and control of 1 khz, 6 mj, 30 fs laser pulses from a ti:sapphire regenerative amplifier. *Appl. Opt.*, 48(30):5692–5695, Oct 2009.

[16] E. Constant, D. Garzella, P. Breger, et al. Optimizing high harmonic generation in absorbing gases: Model and experiment. *Phys. Rev. Lett.*, 82:1668–1671, Feb 1999.

[17] E. Constant, D. Garzella, P. Breger, et al. Optimizing high harmonic generation in absorbing gases: Model and experiment. *Phys. Rev. Lett.*, 82:1668–1671, Feb 1999.

[18] P. B. Corkum. Plasma perspective on strong field multiphoton ionization. *Phys. Rev. Lett.*, 71:1994–1997, Sep 1993.

[19] E. Cormier and M. Lewenstein. Optimizing the efficiency in high order harmonic generation optimization by two-color fields. *The European Physical Journal D - Atomic, Molecular, Optical and Plasma Physics*, 12(2):227–233, 2000.

[20] L. C. Dinu, H. G. Muller, S. Kazamias, et al. Measurement of the subcycle timing of attosecond xuv bursts in high-harmonic generation. *Phys. Rev. Lett.*, 91:063901, Aug 2003.

[21] S. N. Dixit and P. Lambropoulos. Theory of photoelectron angular distributions in resonant multiphoton ionization. *Phys. Rev. A*, 27:861–874, Feb 1983.

[22] P. D. H. Eppink, A. T. J. B. Velocity map imaging of ions and electrons using electrostatic lenses: application in photoelectron and photofragment ion imaging of molecular oxygen, 1997.

[23] P. Farmanara, O. Steinkellner, M. T. Wick, et al. Ultrafast internal conversion and photodissociation of molecules excited by femtosecond 155 nm laser pulses. *The Journal of Chemical Physics*, 111(14), 1999.

[24] O. Faucher, P. Tzallas, E. Benis, et al. Four-dimensional investigation of the 2nd order volume autocorrelation technique. *Applied Physics B*, 97(2):505–510, 2009.

[25] X. Feng, S. Gilbertson, H. Mashiko, et al. Generation of isolated attosecond pulses with 20 to 28 femtosecond lasers. *Phys. Rev. Lett.*, 103:183901, Oct 2009.

[26] F. Ferrari, F. Calegari, M. Lucchini, et al. High-energy isolated attosecond pulses generated by above-saturation few-cycle fields. *Nature Photonics*, 4(12):875–879, 2010.

[27] F. Ferrari, F. Calegari, M. Lucchini, et al. High-energy isolated attosecond pulses generated by above-saturation few-cycle fields. *Nature Photonics*, 4(12):875–879, 2010.

[28] M. Ferray, A. L'Huillier, X. F. Li, et al. Multiple-harmonic conversion of 1064 nm radiation in rare gases. *Journal of Physics B: Atomic, Molecular and Optical Physics*, 21(3):L31, 1988.

[29] T. Fuji, A. Apolonski∗, and F. Krausz. Self-stabilization of carrier-envelope offset phase by use of difference-frequencygeneration. *Opt. Lett.*, 29(6):632–634, Mar 2004.

[30] T. Fuji, J. Rauschenberger, A. Apolonski, et al. Monolithic carrier-envelope phase-stabilization scheme. *Opt. Lett.*, 30(3):332–334, Feb 2005.

[31] M. B. Gaarde and K. J. Schafer. Space-time considerations in the phase locking of high harmonics. *Phys. Rev. Lett.*, 89:213901, Oct 2002.

[32] F. Gilmore. Potential energy curves for N2, NO, O2 and corresponding ions. *Journal of Quantitative Spectroscopy and Radiative Transfer*, 5:369–389, Apr. 1965.

[33] A. González-Castrillo, A. Palacios, H. Bachau, and F. Martín. Clocking ultrafast wave packet dynamics in molecules through uv-induced symmetry breaking. *Phys. Rev. Lett.*, 108:063009, Feb 2012.

[34] E. Goulielmakis, Z.-H. Loh, A. Wirth, et al. Real-time observation of valence electron motion. *Nature*, 466(7307):739–743, 0.

[35] E. Goulielmakis, M. Schultze, M. Hofstetter, et al. Single-cycle nonlinear optics. *Science*, 320(5883):1614–1617, 2008.

[36] J.-F. Hergott, M. Kovacev, H. Merdji, et al. Extreme-ultraviolet high-order harmonic pulses in the microjoule range. *Phys. Rev. A*, 66:021801, Aug 2002.

[37] M. Holler, F. Schapper, L. Gallmann, and U. Keller. Attosecond electron wave-packet interference observed by transient absorption. *Phys. Rev. Lett.*, 106:123601, Mar 2011.

[38] R. Hörlein, Y. Nomura, P. Tzallas, et al. Temporal characterization of attosecond pulses emitted from solid-density plasmas. *New Journal of Physics*, 12(4):043020, 2010.

[39] D. J. Jones, S. A. Diddams, J. K. Ranka, et al. Carrier-envelope phase control of femtosecond mode-locked lasers and direct optical frequency synthesis. *Science*, 288(5466):635–639, 2000.

[40] I. J. Kim, C. M. Kim, H. T. Kim, et al. Highly efficient high-harmonic generation in an orthogonally polarized two-color laser field. *Phys. Rev. Lett.*, 94:243901, Jun 2005.

[41] K. Klünder, J. M. Dahlström, M. Gisselbrecht, et al. Probing single-photon ionization on the attosecond time scale. *Phys. Rev. Lett.*, 106:143002, Apr 2011.

[42] G. Kolliopoulos, P. A. Carpeggiani, D. Rompotis, D. Charalambidis, and P. Tzallas. A compact collinear polarization gating scheme for many cycle laser pulses. *Review of Scientific Instruments*, 83(6):–, 2012.

[43] M. Kornberg and P. Lambropoulos. Photoelectron energy spectrum in 'direct' two-photon double ionization of helium. *Journal of Physics B: Atomic, Molecular and Optical Physics*, 32(20):L603–L613, 1999-12-01T00:00:00.

[44] F. Krausz and M. Ivanov. Attosecond physics. *Rev. Mod. Phys.*, 81:163–234, Feb 2009.

[45] P. Kruit and F. H. Read. Magnetic field paralleliser for 2 electron-spectrometer and electron-image magnifier. *Journal of Physics E: Scientific Instruments*, 16(4):313, 1983.

[46] J. E. Kruse, P. Tzallas, E. Skantzakis, et al. Inconsistencies between two attosecond pulse metrology methods: A comparative study. *Phys. Rev. A*, 82:021402, Aug 2010.

[47] K. Kulander, K. Schafer, and J. Krause. Dynamics of short-pulse excitation, ionization and harmonic conversion. In B. Piraux, A. LHuillier, and K. Rzewski, editors, *Super-Intense Laser-Atom Physics*, volume 316 of *NATO ASI Series*, pages 95–110. Springer US, 1993.

[48] P. Lambropoulos, L. A. A. Nikolopoulos, and M. G. Makris. Signatures of direct double ionization under xuv radiation. *Phys. Rev. A*, 72:013410, Jul 2005.

[49] M. Lewenstein, P. Balcou, M. Y. Ivanov, A. L'Huillier, and P. B. Corkum. Theory of high-harmonic generation by low-frequency laser fields. *Phys. Rev. A*, 49:2117–2132, Mar 1994.

[50] Y. Mairesse, A. de Bohan, L. J. Frasinski, et al. Attosecond synchronization of high-harmonic soft x-rays. *Science*, 302(5650):1540–1543, 2003.

[51] Y. Mairesse and F. Quéré. Frequency-resolved optical gating for complete reconstruction of attosecond bursts. *Phys. Rev. A*, 71:011401, Jan 2005.

[52] H. Mashiko, S. Gilbertson, M. Chini, et al. Extreme ultraviolet supercontinua supporting pulse durations of less than one atomic unit of time. *Opt. Lett.*, 34(21):3337–3339, Nov 2009.

[53] H. Mashiko, S. Gilbertson, C. Li, et al. Double optical gating of high-order harmonic generation with carrier-envelope phase stabilized lasers. *Phys. Rev. Lett.*, 100:103906, Mar 2008.

[54] H. Mashiko, A. Suda, and K. Midorikawa. All-reflective interferometric autocorrelator for the measurement of ultra-short optical pulses. *Applied Physics B*, 76(5):525–530, 2003.

[55] H. Mashiko, A. Suda, and K. Midorikawa. Second-order autocorrelation functions for all-reflective interferometric autocorrelator. *Applied Physics B*, 87(2):221–226, 2007.

[56] D. B. Milošević and W. Becker. Role of long quantum orbits in high-order harmonic generation. *Phys. Rev. A*, 66:063417, Dec 2002.

[57] O. D. Mücke, O. Kuzucu, F. N. C. Wong, et al. Experimental implementation of optical clockwork without carrier-envelopephase control. *Opt. Lett.*, 29(23):2806–2808, Dec 2004.

[58] Y. Nabekawa, T. Shimizu, T. Okino, et al. Conclusive evidence of an attosecond pulse train observed with the mode-resolved autocorrelation technique. *Phys. Rev. Lett.*, 96:083901, Feb 2006.

[59] H. Niikura, F. Lgar, R. Hasbani, et al. Sub-laser-cycle electron pulses for probing molecular dynamics. *Nature*, 417(6892):917–922, 2002.

[60] L. A. A. Nikolopoulos, E. P. Benis, P. Tzallas, et al. Second order autocorrelation of an xuv attosecond pulse train. *Phys. Rev. Lett.*, 94:113905, Mar 2005.

[61] M. Nisoli, S. De Silvestri, and O. Svelto. Generation of high energy 10 fs pulses by a new pulse compression technique. *Applied Physics Letters*, 68(20), 1996.

[62] Y. Nomura, R. Hrlein, P. Tzallas, et al. Attosecond phase locking of harmonics emitted from laser-produced plasmas. *Nature Physics*, 5(2):124–128, 2008.

[63] P. M. Paul, E. S. Toma, P. Breger, et al. Observation of a train of attosecond pulses from high harmonic generation. *Science*, 292(5522):1689–1692, 2001.

[64] A. Peralta Conde, J. Kruse, O. Faucher, et al. Realization of time-resolved two-vacuum-ultraviolet-photon ionization. *Phys. Rev. A*, 79:061405, Jun 2009.

[65] J. F. Pérez-Torres, J. L. Sanz-Vicario, H. Bachau, and F. Martín. The role of autoionizing states in two-photon dissociative ionization of h_2 by xuv ultrashort laser pulses. *Journal of Physics B: Atomic, Molecular and Optical Physics*, 43(1):015204, 2010.

[66] T. Popmintchev, M.-C. Chen, D. Popmintchev, et al. Bright coherent ultrahigh harmonics in the kev x-ray regime from mid-infrared femtosecond lasers. *Science*, 336(6086):1287–1291, 2012.

[67] A. Rouze, F. Kelkensberg, W. K. Siu, et al. Photoelectron kinetic and angular distributions for the ionization of aligned molecules using a hhg source. *Journal of Physics B: Atomic, Molecular and Optical Physics*, 45(7):074016, 2012.

[68] P. Saliéres and M. Lewenstein. Generation of ultrashort coherent xuv pulses by harmonic conversion of intense laser pulses in gases: towards attosecond pulses. *Measurement Science and Technology*, 12(11):1818, 2001.

[69] P. Salières, A. L'Huillier, and M. Lewenstein. Coherence control of high-order harmonics. *Phys. Rev. Lett.*, 74:3776–3779, May 1995.

[70] P. Salires and M. Lewenstein. Generation of ultrashort coherent xuv pulses by harmonic conversion of intense laser pulses in gases: towards attosecond pulses. *Measurement Science and Technology*, 12(11):1818, 2001.

[71] G. Sansone. Quantum path analysis of isolated attosecond pulse generation by polarization gating. *Phys. Rev. A*, 79:053410, May 2009.

[72] G. Sansone, E. Benedetti, F. Calegari, et al. Isolated single-cycle attosecond pulses. *Science*, 314(5798):443–446, 2006.

[73] G. Sansone, F. Kelkensberg, J. F. Prez-Torres, et al. Electron localization following attosecond molecular photoionization. *Nature*, 465(7299):763–766, 0.

[74] E. Skantzakis, P. Tzallas, J. Kruse, C. Kalpouzos, and D. Charalambidis. Coherent continuum extreme ultraviolet radiation in the sub-100-nj range generated by a high-power many-cycle laser field. *Opt. Lett.*, 34(11):1732–1734, Jun 2009.

[75] E. Skantzakis, P. Tzallas, J. E. Kruse, et al. Tracking Autoionizing-Wave-Packet Dynamics at the 1-fs Temporal Scale. *Physical Review Letters*, 105(4):043902, July 2010.

[76] A. V. Sokolov, D. D. Yavuz, and S. E. Harris. Subfemtosecond pulse generation by rotational molecular modulation. *Opt. Lett.*, 24(8):557–559, Apr 1999.

[77] I. J. Sola, E. Mvel, L. Elouga, et al. Controlling attosecond electron dynamics by phase-stabilized polarization gating. *Nature Physics*, 2(5):319–322, 2006.

[78] A. Suda, M. Hatayama, K. Nagasaka, and K. Midorikawa. Generation of sub-10-fs, 5-mj-optical pulses using a hollow fiber with a pressure gradient. *Applied Physics Letters*, 86(11):–, 2005.

[79] E. J. Takahashi, P. Lan, O. D. Mcke, Y. Nabekawa, and K. Midorikawa. Attosecond nonlinear optics using gigawatt-scale isolated attosecond pulses. *Nature Communications*, 4:–, 0.

[80] E. J. Takahashi, P. Lan, O. D. Mücke, Y. Nabekawa, and K. Midorikawa. Infrared two-color multicycle laser field synthesis for generating an intense attosecond pulse. *Phys. Rev. Lett.*, 104:233901, Jun 2010.

[81] H. Telle, G. Steinmeyer, A. Dunlop, et al. Carrier-envelope offset phase control: A novel concept for absolute optical frequency measurement and ultrashort pulse generation. *Applied Physics B*, 69(4):327–332, 1999.

[82] S. A. Trushin, W. E. Schmid, and W. Fu. Time-resolved photodissociation of oxygen at 162 nm. *Journal of Physics B: Atomic, Molecular and Optical Physics*, 44(16):165602, 2011.

[83] P. Tzallas, D. Charalambidis, N. A. Papadogiannis, K. Witte, and G. D. Tsakiris. Direct observation of attosecond light bunching. *Nature*, 426(6964):267–271, 2003.

[84] P. Tzallas, D. Charalambidis, N. A. Papadogiannis, K. Witte, and G. D. Tsakiris. Second-order autocorrelation measurements of attosecond xuv pulse trains. *Journal of Modern Optics*, 52(2-3):321–338, 2005.

[85] P. Tzallas, E. Skantzakis, E. P. Benis, et al. Full temporal reconstruction of a lower order harmonic superposition. *New Journal of Physics*, 9(7):232, 2007.

[86] P. Tzallas, E. Skantzakis, and D. Charalambidis. Measuring the absolute carrier-envelope phase of many-cycle laser fields. *Phys. Rev. A*, 82:061401, Dec 2010.

[87] P. Tzallas, E. Skantzakis, and D. Charalambidis. Direct two-xuv-photon double ionization in xenon. *Journal of Physics B: Atomic, Molecular and Optical Physics*, 45(7):074007, 2012.

[88] P. Tzallas, E. Skantzakis, C. Kalpouzos, et al. Generation of intense continuum extreme-ultraviolet radiation by many-cycle laser fields. *Nature Physics*, (12):846850, 2007.

[89] P. Tzallas, E. Skantzakis, J. Kruse, and D. Charalambidis. On the generation of intense isolated attosecond pulses by many-cycle laser fields. In K. Yamanouchi, D. Charalambidis, and D. Normand, editors, *Progress in Ultrafast Intense Laser Science VII*, volume 100 of *Springer Series in Chemical Physics*, pages 163–190. Springer Berlin Heidelberg, 2011.

[90] P. Tzallas, E. Skantzakis, L. A. A. Nikolopoulos, D. G. D. Tsakiris, and Charalambidis.

[91] P. Tzallas, E. Skantzakis, L. A. A. Nikolopoulos, G. D. Tsakiris, and D. Charalambidis. Extreme-ultraviolet pump-probe studies of one-femtosecond-scale electron dynamics. *Nature Physics*, 7(10):781–784, 2011.

[92] M. J. J. Vrakking. An iterative procedure for the inversion of two-dimensional ion/photoelectron imaging experiments. *Review of Scientific Instruments*, 72(11):4084–4089, 2001.

[93] M. J. J. Vrakking, D. M. Villeneuve, and A. Stolow. Observation of fractional revivals of a molecular wave packet. *Phys. Rev. A*, 54:R37–R40, Jul 1996.

[94] H. Wang, M. Chini, S. Chen, et al. Attosecond time-resolved autoionization of argon. *Phys. Rev. Lett.*, 105:143002, Oct 2010.

[95] Y. Zheng, Z. Zeng, P. Zou, et al. Dynamic chirp control and pulse compression for attosecond high-order harmonic emission. *Phys. Rev. Lett.*, 103:043904, Jul 2009.

[96] M. Zimmermann, C. Gohle, R. Holzwarth, T. Udem, and T. W. Hnsch. Optical clockwork with an offset-free difference-frequency comb: accuracy of sum- and difference-frequency generation. *Opt. Lett.*, 29(3):310–312, Feb 2004.